Collective behavior of molecular motors

DISSERTATION

zur Erlangung des akademischen Grades
Doctor rerum naturalium
(Dr. rer. nat.)

vorgelegt
der Fakultät Mathematik und Naturwissenschaften
der Technischen Universität Dresden

von

Manuel Neetz

geboren am 27. Oktober 1982 in Braunschweig, Deutschland

Erste Gutachterin: Prof. Dr. Petra Schwille
Zweiter Gutachter: Prof. Dr. Arne Gennerich

Eingereicht am: 13. Januar 2012
Verteidigt am:

Table of contents

List of Figures

Abbreviations

AAA	ATPase associated with diverse cellular activities
AMPPNP	adenylyl-imidodiphosphate
ATP	adenosine-5'-triphosphate
CV	column volume
DDS	dimethyldicholorosilane
DNA	deoxyribonucleic acid
DTT	dithiothreitol
EGTA	ethylene glycol tetraacetic acid
FITC	fluorescein isothiocyanate
GFP	green fluorescent protein
GMPCPP	guanylyl-(alpha, beta)-methylene-diphosphonate
GST	glutathion-S-transferase
GTP	guanosine-5'-triphosphate
h	Planck constant ($6.63 \cdot 10^{-34}$ J s)
HEPES	4-(2-hydroxyethyl)-1-piperazineethanesulfonic acid
IPTG	isopropyl β-D-1-thiogalactopyranoside
k_B	Boltzmann constant ($1.38 \cdot 10^{-23}$ J / K)
LB	lysogeny broth
m_e	electron mass ($9.11 \cdot 10^{-31}$ kg)
MOPS	3-(N-morpholino)propanesulfonic acid
mRNA	messenger ribonucleic acid
NA	numerical aperture
OD	optical density
PBS	phosphate buffered saline
PIPES	piperazine-N,N′-bis(2-ethanesulfonic acid)
RNAi	ribonucleic acid interference
SEM	standard error of the mean
TAMRA	carboxytetramethylrhodamine
TEV	tobacco etch virus
TIRF	total internal reflection
Tris	tris(hydroxymethyl)aminomethane
TRITC	tetramethyl rhodamine isothiocyanate

Summary

Microtubule associated molecular motors are involved in a multitude of fundamental cellular processes such as intracellular transport and spindle positioning. During these movements multiple motor proteins often work together and are, therefore, able to exert high forces. Thus force generation and sensing are common mechanisms for controlling motor driven movement. These mechanisms play a pivotal role when motor proteins antagonize each other, e.g. to facilitate oscillations of the spindle or the nucleus.

Single motor proteins have been characterized in depth over the last two decades, our understanding of the collective behavior of molecular motors remains, however, poor. Since motor proteins often cooperate while they walk along microtubules, it is necessary to describe their collective reaction to a load quantitatively in order to understand the mechanism of many motor-driven processes.

I studied the antagonistic action of many molecular motors (of one kind) in a gliding geometry. For this purpose I crosslinked two microtubules in an antiparallel fashion, so that they formed "doublets". Then I observed the gliding motility of these antiparallel doublets and analyzed the gliding velocity with respect to the relative number of motors pulling or pushing against each other. I observed that the antiparallel doublets gliding on conventional kinesin-1 (from *Drosophila melanogaster*) as well as cytoplasmic dynein (from *Saccharomyces cerevisae*) exhibited two distinct modes of movement, slow and fast, which were well separated. Furthermore I found a bistability, meaning, that both kinds of movement, slow and fast, occurred at the same ratio of antagonizing motors. Antiparallel doublets gliding on the non-processive motor protein Ncd (the kinesin-14 from *D. melanogaster*) showed, however, no bistability. The collective dynamics of all three motor proteins were described with a quantitative theory based on single-motor properties.

Furthermore the response of multiple dynein motors towards an external, well-defined load was measured in a gliding geometry by magnetic tweezing. Examples of multi-motor force-velocity relationships are presented and discussed. I established, furthermore, a method for counting single surface immobilized motors to guide the evaluation of the tweezing experiments.

1 Introduction to the functions of molecular motors

In chapter 1.1 I present the most important milestones in our understanding of biological motility due to force generation by molecular motors. I neglect, however, many aspects of actin based motility in order to focus on the particular microtubule associated molecular motors I worked with. I ignore nearly all aspects of motor regulation and concentrate rather on the mechanics of motor activity, which is essential for understanding multi-motor behavior. In chapter 1.2 I review briefly our knowledge about microtubules in as far it is of importance for understanding the activity of molecular motors. In chapter 1.3 I summarize recent efforts to elucidate the directionality of microtubule associated molecular motors. In chapter 1.4 I present selected examples of complex intracellular movements, which are regulated by microtubule associated molecular motors.

1.1 How molecular motors move

1.1.1 Of muscles and molecules

The question how nature facilitates movement of living matter puzzles scientists since the early days of biological and medical research. This question is not only deeply rooted in the history of science, but the struggle to find answers to it, is also a prime example of the relationship between scientific thinking and technological development. Conceptual progress in science often relies on tools, which allow, sometimes literally, seeing things from a different angle.

Luigi Galvani employed the newest techniques from electrical engineering and discovered at the end of the 18th century, that electrical currents were sufficient for exciting muscles [Galvani, 1792]. Galvani believed, however, in an “animal electric fluid”, which is supposedly bound to an individual animal. He did not realize – different than his companion Alessandro Volta – that general physical laws are the fundamental explanation for his experimental results [Volta, 1792]. Nevertheless Galvani’s observations paved the way to a modern understanding of neuronal and muscle activity.

Another tool, the optical microscope, was invented by Robert Hooke in the 17th century. His *Micrographia* encompasses detailed drawings of microscopic objects and even coined the term cell (Latin *cella*: store room) [Hooke, 1665]. About two centuries after Hooke's invention and one century after Galvani's seminal experiments, Walther Flemming relied on new dyes for staining cells. The chemist William Perkin has developed these synthetic dyes in the middle of the 19th century. The new staining method and tedious observation of fixed cells culminated in the first detailed description of mitosis and meiosis, including some of their intracellular dynamics. Flemming also gave chromatin its name (Greek χρώμα: color) and witnessed already the snapshots of a highly coordinated dance of genetic material before cell division [Flemming, 1878; Flemming, 1880].

It should take a long time until the molecular players involved in generating forces - and thereby separating genetic material - during mitosis and meiosis were finally discovered. For most of the 20th century, when molecular biology entered the stage, the motility field was identical with the muscle field. Actually the term myosin was already coined in 1864 (Greek μυός, genitive of μυς: muscle) when Kühne purified the protein from muscle tissue [Kühne, 1864]. In the 1940s the activation of actin-myosin systems by MgATP was discovered [Needham et al, 1942; Szent-Györgyi & Banga, 1941–1942; Szent-Györgyi & Banga, 1942]. With this work the principle of converting chemical into mechanical energy via ATP hydrolysis was laid out. The question, how the force generation via ATP hydrolysis is achieved structurally, was addressed by HE Huxley and Hanson [Huxley & Hanson, 1954] as well as AF Huxley and Niedergerke [Huxley & Niedergerke, 1954] in the 1950s and led to proposing the sliding filament model. This model suggests that ATP hydrolysis induces a "working stroke" of the crossbridges connecting the two sliding filaments. Later it was confirmed that these crossbridges are formed by myosin motors. Advances in electron microscopy provided new structural data in the end of the decade, which elucidated how the myosin motors are attached to the thick filament. This observation led AF Huxley and Simmons to suggesting the strikingly successful crossbridge model for the collective activity of myosin motors in muscles [Huxley & Simmons, 1971]. In this model the elasticity of the motor protein and its subsequent stretching due to its power stroke is already incorporated.

Apart from muscles another tractable model object for studying motility were cilia and flagella. Consequently the first microtubule associated ATPase was purified from *Tetrahymena pyriformis* in 1965. The authors christened it dynein (Greek *δύναμις*: force). They also realized, that "dynein is one of a class of proteins of widespread occurrence in relation to cell motility, but distinct from the contractile proteins related to actomyosin" [Gibbons & Rowe, 1965]. Cytoplasmic dynein, one of the essential proteins for intracellular transport was, however, only discovered in 1987 [Lye et al, 1987; Paschal et al, 1987]. Two years before the "novel force-generating protein, kinesin" (Greek *κίνηση*: movement), later on termed kinesin-1, was already described [Brady, 1985; Vale et al, 1985]. With these findings the new field of microtubule associated molecular motors (from now on referred to as (molecular) motors or motor proteins) was established and started to flourish. In the following years many more kinesins were discovered, a new nomenclature was introduced [Lawrence et al, 2004], and the individual components and adaptors of the huge motor complex forming dynein were scrutinized one by one (see e.g. [Kardon & Vale, 2009] and references therein).

Thanks to the new technology of video-enhanced differential interference contrast microscopy it became possible at the beginning of the 1980s to observe directly the dynamic properties of cell division and cargo transport, which are based on the activity of molecular motors [Allen et al, 1981]. Differential interference contrast microscopy exploits the different travel times of light through media of different refractive indices and allowed together with video technology for the first time to spot the movement of particles < 1 µm in axonal transport *in vivo* and *in vitro* [Allen et al, 1982; Brady et al, 1982].

The next step was achieved soon: At the end of the 20th century it was time for looking at the properties of single motors *in vitro* to eventually dissect their mechanochemical cycle and therewith the basis of all motor-driven processes.

1.1.2 Kinesin-1, the working horse of single-molecule research

In the new field kinesin-1 turned out to be the molecule of choice to study generic motor properties. It is of utmost importance for intracellular transport and present in nearly all eukaryotic cells. It is also much smaller than dynein (with just ~ 120 kD instead of ~ 500 kD per heavy chain) and can be easily purified with a bacterial expression system. It consists essentially of two light and two heavy chains, the latter comprised of a "head" and a "tail" domain. The head is connected via a flexible linker called "neck" to the "stalk" domain, which consists of a long coiled-coil, see Figure 1. A homodimer of the two heavy chains forms a fully functional motor and is usually used for *in vitro* experiments. Kinesin-1 is also referred to as a N-terminal motor, because its head is at the N-terminal of the heavy chain. The C-terminus of the heavy chain defines the tail; the two light chains are located at this tail region. The heads interact with the microtubule lattice and also hosts the catalytic domain, while the light chains at the tail are responsible for binding to cargo [Vale, 2003].

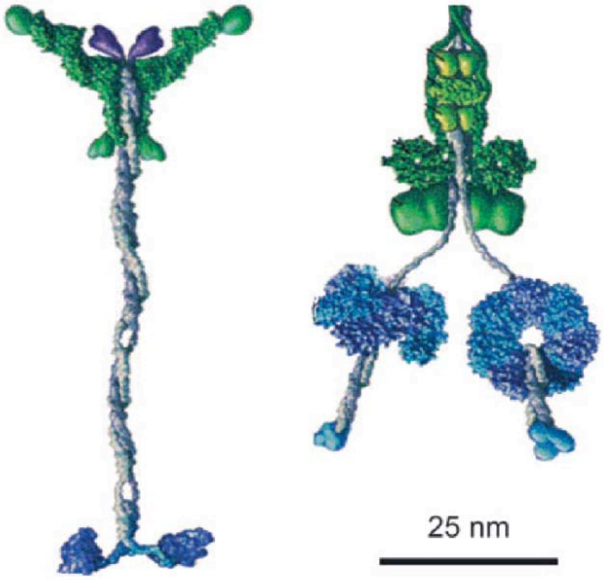

Figure 1. Structure of kinesin-1 and cytoplasmic dynein. On the left the structure of kinesin-1 with the two heads (blue), the long coiled-coil forming the stalk (grey) and the light chains (blue) are shown. On the right dynein with the microtubule binding domains and the AAA rings (both in blue) as well as additional subunits such as light and intermediated chains (green) are shown. Figure taken from [Kolomeisky & Fisher, 2007], modified from [Vale, 2003].

Kron and Spudich introduced the gliding assay (for myosin), where the motor is immobilized via its tail on a coverslip, so that the heads are free to propel filaments [Kron & Spudich, 1986]. Howard et al. employed the gliding assay to demonstrate, that kinesin-1 is a processive motor, meaning that it travels for a distance much beyond its own length scale along the filament before it detaches from it. It was also shown that kinesin-1 moves with an ATP dependent velocity, and that the gliding velocity does not depend on the motor density at high ATP concentrations [Howard et al, 1989].

Block and coworkers confirmed the idea of processivity with the means of optical trapping (also referred to as optical tweezing) [Block et al, 1990]. Soon optical trapping was pushed to the next level and the 8 nm steps of kinesin-1 could be measured by exposing the trapped bead and therefore the attached motor to well-controlled forces [Svoboda et al, 1993]. The first data relating the velocity of single kinesin-1 molecules to a load force were obtained via an optical trap, an elastic glass fiber or the viscous drag of gliding microtubules. The resulting force-velocity relationship was found to be linear (in the regime of positive velocities), and the stall force was measured to be around 4 – 6 pN [Hunt et al, 1994; Meyhofer & Howard, 1995; Svoboda & Block, 1994].

Vale and coworkers introduced the stepping assay of fluorescently tagged motors in combination with total internal reflection (TIRF) microscopy [Vale et al, 1996]. This technique reduces the fluorescent background significantly by decreasing the penetration depth of the illuminating light and allows therefore observing single molecules at a high signal-to-noise ratio. Therewith all main tools for studying the kinetics of single motor proteins were established in the middle of the 1990s.

It only took a few more years until the hypothesis was confirmed, that kinesin-1 hydrolyses one molecule of ATP per step [Coy et al, 1999; Schnitzer & Block, 1997]. The question how such hydrolysis events are exactly coupled to the single conformational changes within the kinesin-1 molecules is still under debate [Block, 2007]. An important aspect of the single-molecule mechanochemistry is surely its load-dependent detachment from the microtubule - and therefore load-dependent processivity [Schnitzer et al, 2000]. Without load-dependent detachment many collective effects of motor driven motility would not work [Howard, 2009].

Two different techniques were employed independently of each other to observe the hand-over-hand stepping mechanism of kinesin-1, the optical trapping assay [Asbury et al, 2004] and the tracking of fluorophores [Yildiz et al, 2004]. Carter and Cross showed in 2005 via an optical trap how the velocity of kinesin-1 depends on an opposing force and that it is able to walks backwards at very high loads (in an ATP dependent manner). It was suggested that once a motor head is bound to the microtubule lattice, the other head searches via diffusion for a new binding site, and that the outcome of this search can be biased by an external load [Carter & Cross, 2005]. Quantum dot tracking of mutants with differently long neck linkers indicates that it is more precisely intramolecular strain, which sets the directionality of the kinesin-1 motor. The work highlights the importance of the flexibility of the neck linker domain for the coordination of the stepping behavior [Yildiz et al, 2008]. This aspect is currently also studied in the context of multi-motor transport. Quantum dots were also employed to track the rotation of microtubules gliding on kinesin-1 motors [Nitzsche et al, 2008]. This study confirms the finding that kinesin-1 motors follow always one protofilament within the microtubule lattice [Ray et al, 1993].

1.1.3 Kinesin-14, an unusual kinesin with a new twist

While microscopic movements, such as transport mechanisms, motivated the search for dynein and kinesin-1, other proteins were found due to lack-of-function mutations. The microscopic effect of the claret-non-disjunctional (ca^{nd}) mutation, which leads to unfocused mitotic spindles, was described in 1983 [Kimble & Church, 1983]. Soon upon purification and description of the protein encoded in the respective locus, it was named Ncd, according to the mutation. This motor protein is nowadays categorized as kinesin-14, and it is in many respects structurally similar to kinesin-1. It is, however, a C-terminal motor, with its motor head (and catalytic domain) at the C-terminus [Endow et al, 1990].

Surprisingly Ncd turned out to be a (-) directed motor, meaning that it walks into the opposite direction than kinesin-1. Furthermore it generates a strong torque in gliding assays via its power stroke [Walker et al, 1990]. Gliding assays revealed that multiple Ncd motors propel microtubules with an ATP dependent velocity. The gliding velocity does not depend on the length of the filament or on the motor density. Different than for the processive kinesin-1 between three and seven Ncd motors are necessary to provide stable gliding at saturating ATP concentration [deCastro et al, 1999]. The size of Ncd's power-stroke was determined via optical tweezing experiments to be 9 nm [deCastro et al, 2000]. Taken together with the structural information from electron microscopy [Endres et al, 2006] Ncd seems to behave more like muscle myosin than like a kinesin-1. It is, however, interesting to notice, that Ncd, different than muscle myosin, carries out its power stroke at the end of the attachment cycle to the filament [deCastro et al, 2000; Endres et al, 2006]. Thus the original crossbridge model cannot be applied straightforward to Ncd driven multi-motor translocation. It was furthermore shown, that kinesin-14 is able to bundle microtubules and slide them relative to each other in a directed manner [Braun et al, 2009; Fink et al, 2009].

1.1.4 Cytoplasmic dynein, the molecule with many qualities

Cytoplasmic dynein (henceforth denoted dynein) is a 1.2 MD multi-protein motor complex, which is the major (-) directed motor protein for intracellular transport. It is also involved in spindle positioning in many different model organisms (e.g. in *Caenorhabditis elegans* and budding yeast), and the effect of different subunits, at least for its *in vivo* function, has been studied extensively. Here I refer, however, mainly to work analyzing the properties of the "naked" dynein without any additional subunits such as dynactin.

Structurally and evolutionary dynein is very different from the family of kinesins. Dynein evolved from the hexameric AAA proteins (ATPase associated with diverse cellular activities) and each of its two heavy chains contains a ring with four AAA functional domains, see Figure 1. It was, however, shown, that only ATP hydrolysis by AAA1 and ATP binding by AAA3 is essential for proper motility [Reck-Peterson & Vale, 2004]. The microtubule binding domain, whose structure was resolved recently by crystallography, is spatially separated from the site of hydrolysis [Carter et al, 2008].

The stall force, velocity and ATP dependence of kinesin-1 and dynein (from pig's brain) are very similar despite the structural differences of the two proteins. The single-exponential dwell-time distribution indicates together with the 8 nm steps a hand-over-hand stepping mechanism also for dynein [Toba et al, 2006]. This stepping mechanism was confirmed via quantum-dot tracking for a truncated homodimer of dynein from budding yeast [Reck-Peterson et al, 2006]. Further experiments with this truncated construct indicate, however, that the hand-over-hand mechanism is not coordinated. Thus, it seems as if each head is able to step independently of the other head [DeWitt et al, 2011; Qiu et al, 2012]. Yet, dynein seems to be a very persistent motor, since it was shown to move processively backward at high opposing loads, even in the absence of ATP [Gennerich et al, 2007]. These findings question in as far dynein undergoes force-induced detachment, but one should notice, that these experiments were carried through at low salt conditions (30 mM HEPES instead of 30 mM HEPES + 50 mM KAcetate as used by [Reck-Peterson et al, 2006]), which lead to an increased processivity (Prof. Dr. Reck-Peterson, Harvard Medical School, talk at the Annual Meeting of the American Biophysical Society 2010 in San Francisco).

A controversy developed around work, which showed that dynein (from bovine brain) stalls at much lower forces than measured by other groups. Some authors claim furthermore that dynein can exhibit different step sizes in dependence on the load it is subjected to [Mallik et al, 2004]. Furthermore work with endosomes from *Dictyostelium* also indicates a lower stall force of dynein [Soppina et al, 2009]. It can only be speculated whether a miscalibration of the trap or other cofactors (only present *in vivo*) lead to these surprising results.

1.2 Structure and function of microtubules

Light microscopy in combination with a new staining method led Walther Flemming to the discovery of the mitotic spindle [Flemming, 1878; Flemming, 1880]. It was another improvement in light microscopy, polarized light microscopy, which led to new insights into the role of mitotic spindle fibers in cell division. Inoue et al. described the dynamic properties of these fibers, which were later on identified as microtubules, already in 1967 [Inoue & Sato, 1967]. Eventually the interaction between (chromo-)kinesins and dynamic microtubules, which facilitates proper chromosome segregation, has become a prime example for studying the collective behavior of molecular motors, see e.g. [Campas & Sens, 2006].

Microtubules are present in nearly all eukoryotic cells and one of their main functions is to provide tracks for kinesins and dyneins. The purification of functional tubulin (from brain tissue) was achieved in 1972 and turned out to be a necessary prerequisite for all other *in vitro* motor studies [Borisy & Olmsted, 1972; Weisenberg, 1972].

Microtubules form hollow cylinders with an outer diameter of 25 nm, consisting of typically 12 - 14 protofilaments when they are grown *in vitro*. Each protofilament consists of a chain of alternating α and β tubulin subunits, which form heterodimers. Each of the subunits is 4 nm long, so that a protofilament exhibits an intrinsic periodicity of 8 nm, which corresponds to the step size of many molecular motors. Furthermore the internal structure of α and β tubulin gives rise to a so-called (+) and (-) polarity of microtubules, with α tubulin at the (-) end and β tubulin and (+) end. Microtubules polymerize preferentially at the (+) end, and *in vivo* the (-) end is often capped by a nucleation center. The role of microtubule (+) end dynamics is nicely reviewed in [Howard & Hyman, 2003].

Microtubules shrink and grow by (de-)polymerization in a dynamic equilibrium [Mitchison & Kirschner, 1984], which allows them to exert pulling and pushing forces and eventually to counteract the activity of molecular motors [Dogterom et al, 2005]. Interestingly, similar to molecular motors, microtubules also exhibit a force-velocity relationship [Dogterom & Yurke, 1997]. Vice versa certain kinesins are able to moderate the growth and shrinkage of microtubule and might, therefore, influence the ability of microtubules to generate force, see e.g. [Helenius et al, 2006; Tischer et al, 2009]. Thus the understanding of microtubule dynamics and motor activity is often tightly connected.

But even non-dynamic microtubules, as the ones forming the axoneme, can play an extremely important role in motor activity beyond just providing tracks. The high stiffness of microtubules leads, together with crosslinkers between the microtubules in the axoneme, to a strong resisting force when the axoneme is bend, e.g. by the activity of axonemal dynein. Such a resisting force is an important part of the force-feedback necessary for the oscillations of cilia and therefore the motility of many cell types [Howard, 2009].

Nowadays many different isoforms of tubulin are known and post-translational modifications might play a role in regulating motor activity [Janke & Kneussel, 2010]. E.g. kinesin-14 from the fission yeast *Schizosaccharomyces pombe* propels microtubules from mammalian brain faster than “native” ones from yeast [Braun et al, 2009].

1.3 The directionality of molecular motors

Although the structure of microtubules has been studied extensively, it is not completely clear how molecular motors are actually able to determine the direction of their travel along the microtubule lattice. This question is of particular importance with respect to the collective behavior observed *in vivo*. Cargos, to which motors of opposite directionality attach at the same time, change their direction, sometimes in a coordinated fashion, sometimes seemingly randomly [Welte, 2004]. Some studies report, that motors, which are expected to antagonize each other, might even support each other during vesicle transport [Kural et al, 2005]. And the absence of a (+) end directed motor can lead to a breakdown of transport into (-) end direction [Ally et al, 2009]. Thus the question remains: what sets the directionality of a motor protein? And might the answer to this question be a handle for scientists - and cells - to control it?

One suspect was the catalytic domain, but at least for kinesins it contributes rather to the processivity than to the orientation of the motor [Case et al, 1997; Henningsen & Schliwa, 1997]. A chimera based on the (+) directed motor kinesin-1 with a catalytic domain form the (-) end directed motor Ncd moves towards the (+) of the microtubule, but does so in a less processive manner than the wild type kinesin-1 [Case et al, 1997]. Chimeras with the stalk and neck of Ncd and large parts of the kinesin-1 motor domain move to the (-) end, while a mutation in the neck makes the chimera walk towards the (+) end [Endow & Waligora, 1998]. A mutation in the motor-core from kinesin-14 that touches the neck leads, however, to a bidirectional mutant [Sablin et al, 1998]. Even a single point mutation in the neck of Ncd (in a region, which is highly conserved among C-terminal motor proteins,) causes bidirectional movement [Endow & Higuchi, 2000]. More interestingly, microtubules gliding on the neck-mutant move with wild type velocities and change their direction abruptly, which is a fingerprint of collective behavior. It can be concluded, that the directionality of kinesin motor proteins is mainly encoded in the neck region.

The kinesin-5 Cin8 from budding yeast is a tetrameric motor, capable of cross-linking microtubules, and known to be (+) end directed [Kapitein et al, 2005]. Recently it was, however, demonstrated, that it moves as a single motor processively to the (-) end of microtubules, whereas it acts as a (+) end directed motor, when it propels microtubules in a gliding assay. It could even be shown, that an increasing concentration of motors shifts the motor directionality in the gliding assay from the (-) towards the (+) end [Roostalu et al, 2011]. This study is another example for the importance of coordination and collaboration between multiple motors, even for setting such fundamental parameters as the directionality.

1.4 Force regulation in cell biology via molecular motors

1.4.1 Bidirectional cargo transport

The transport of cargo by motors allows cells to control the concentration of molecules and molecular ensembles at certain points in space and time precisely. Microtubule based transport processes occur in nearly all eukaryotic cells, and the cargo ranges from viral particles over lipid droplets, endosomes, mitochondria and mRNA to motor proteins themselves. The advantage of directed transport over the simplest mechanism for translocation, diffusion, becomes obvious when looking at the typical length scales of cells. The diffusion law is given by

$$< x^2 > = q \ D \ t \qquad \textit{Eq. 1}$$

where $< x^2 >$ is the mean-square-displacement and t the diffusion time. It holds q = 2, 4, 6 for diffusion in 1, 2, 3 dimensions [Einstein, 1905]. The diffusion constant D for a spherical particle with radius r is given by the Einstein-Stoke relationship

$$D = (k_B \, T)/(6 \ \pi \ \eta \ r) \qquad \textit{Eq. 2}$$

with the Boltzmann constant k_B, the temperature T and the viscosity η [Einstein, 1905]. Eq. 1 yields, that it takes a protein with a typical value of D = 5 μm^2 / s [Elowitz et al, 1999] 33 ms to diffuse through a cell of 1 µm but already more than ~ 3 s for diffusing through a cell of 10 µm size (both examples in three dimensions) and more than a day for diffusing (in one dimension) through a cell, e.g. an axon, of 1 mm length. Directional motors with a speed of 1 µm/s can travel the same distance in less than 17 minutes or 100 x faster.

The precise spatial and temporal control of molecular components within the cells requires often bidirectional cargo transport. Therefore bidirectional transport is nearly as abundant as cargo transport in general [Welte, 2004]. Since the phenomenon of bidirectionality is known, scientists wonder whether cells regulate the activity of one particular set of motors, e.g. of the (+) end directed kinesin-1. In some cases particular molecules suppress or enhance the activity of one motor type and therewith guide the cargo into the right direction, see e.g [Dixit et al, 2008; Welte et al, 1998]. But in many cases the cargo (and therewith the motor ensemble) changes its direction seemingly randomly and so fast, that a chemical trigger can be ruled out as an explanation. A very well known example is the biased diffusion of mitochondria.

A combination of *in vivo* and *in vitro* experiments demonstrated that the nature of at least some bidirectional transport processes is a tug-of-war between different teams of motor proteins, e.g. kinesin-1 and dynein [Hendricks et al, 2010; Soppina et al, 2009]. In such a tug-of-war motors of opposite polarity are bound simultaneously to one cargo (and the transport filament) and therefore antagonize each other. Eventually the “stronger” team of motors wins, where “strength” has different aspects, which are illustrated in chapter 2. A reversal of travel direction can be achieved by fluctuations of the number of motors binding to the filament. A theoretical description of such a tug-of-war leads to the prediction, that essentially three kinds of movement exist: fast (+) end and fast (-) end movement as well as no movement due to a force balance between the antagonizing motors pulling at the cargo, see Figure 2 and [Muller et al, 2008].

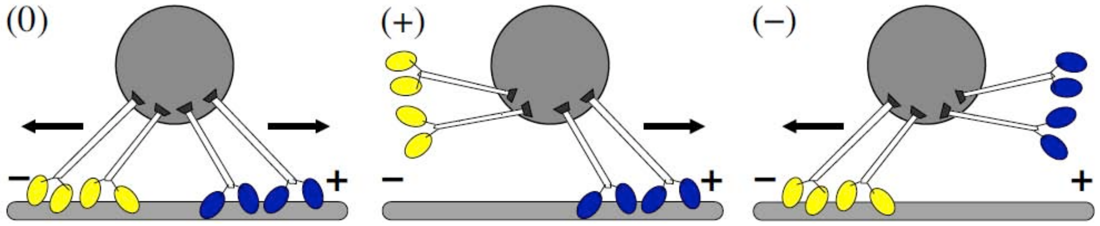

Figure 2. Tug-of-war in bidirectional transport. Schematic of the three predicted states for bidirectional cargo transport by antagonizing motors (yellow: (-) end directed motor, e.g. dynein; blue: (+) end directed motor, e.g. kinesin-1). In state (0) the motors are in a tug-of-war and the cargo stalls; in state (+) and (-) the cargo moves fast to the (+) end of the microtubule or to its (-) end, respectively. Figure taken from [Muller et al, 2008].

The experimental results agree well with the theoretical predictions, which are based on well-known properties of single motors. The simple physical basis of the tug-of-war implies, that force regulates (at least partially) many bidirectional motor driven processes. Whether some regulators of motor activity turn out to tune the capability of motor to generate force, as speculated recently [Shubeita et al, 2008], is, however, not known yet.

Other bidirectional transport mechanisms are implemented by binding of the second (antagonizing) kind of motor protein at the end of the initial directed travel. Thus the tug-of-war starts in this particular case only after the transport towards the (+) end by kinesin-1 is finished. Then the newly bound motor, dynein, wins right away and reverses the direction of transport [Schuster et al, 2011]. This study demonstrates how the combination of physical single motor properties and the regulation of motor number can account for coordinated bidirectional cargo transport within cells.

In vitro experiments show, that the run length and the maximal stall force of cargo can be easily tuned via the number of active motors (see chapter 2). Thus controlling the number of active (or available) motors is a feasible mechanism for regulating multi-motor transport. It can be concluded, that multi-motor transport is more accessible to regulatory mechanisms than single-motor transport, see also the discussion in [Beeg et al, 2008].

1.4.2 Dynein drives intracellular oscillations

The ability of cells to recombine and segregate genetic material in a highly coordinated manner is one of the most fundamental and intriguing processes in the realm of living matter. Large-scale movements of cellular structures, such as the nucleus or chromosomes often accompany reproduction [Parvinen & Soderstrom, 1976]. These movements play a role in chromosome pairing and recombination [Scherthan et al, 2007]. The nuclear oscillations during the meiotic prophase of *S. pombe* are a well-studied example of nuclear movements.

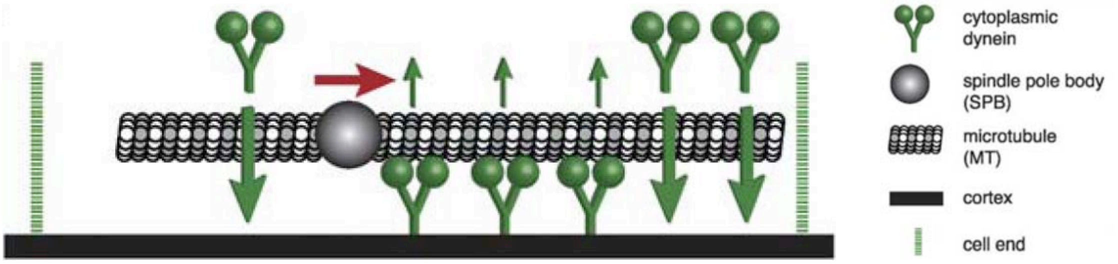

Figure 3. Dynein drives oscillations in *S. pombe*. Schematic of the microtubule-motor arrangement driving the nuclear oscillations in the meiotic prophase of *S. pombe*. The green arrows indicate the (un-)binding of cytoplasmic dynein from/to the microtubule and the cortex. The red arrow indicates the direction of movement of the nucleus, which is bound to the spindle pole body (the centrosome equivalent in yeast). The figure is adapted from [Vogel et al, 2009].

Dynamic microtubules, which are connected to the nucleus via the spindle pole body (the centrosome equivalent in yeast), and the collective activity of dynein motors drive the nuclear oscillations. More precisely, laser ablation of microtubules led to the conclusion, that cortex bound motors pull along the whole length of microtubules and not only at the microtubule tip (see Figure 3). Furthermore, a dynein - 3 x GFP fusion protein and its (re-)distribution during the oscillations could be visualized and confirmed the results obtained by laser ablation [Vogel et al, 2009].

The collective activity of molecular motors was also identified as one of the essential factors for spindle oscillations during the first cell division of *C. elegans*. Although it was so far not possible to visualize dynein directly in *C. elegans*, experiments with RNAi of dynein light chain indicate, that dynein is responsible for pulling the spindle and eventually driving the oscillations [Pecreaux et al, 2006]. Cutting the spindle poles during the asymmetric first cell division of *C. elegans* and analyzing the velocity of its fragments suggested, that all the force generators exert the same force. Differences for the movement of the fragments toward the anterior and the posterior pole were explained rather in differences of the attachment probability of the force generators than their number [Grill et al, 2003].

The starting point for describing both phenomena (in *S. pombe* and *C. elegans*) is, of course, a force balance, which can be generalized as

$$F = \xi \, v \qquad \textit{Eq. 3}$$

where ξ is the friction coefficient of the system, F the force stemming from the microtubule/motor system and v the velocity (of the nucleus or the spindle, respectively). For understanding the phenomenon it is sufficient to limit the description to one spatial dimension, here denoted as x. In the *C. elegans* embryo it holds

$$F = -\, x\, K + G \qquad \textit{Eq. 4}$$

where $x\,K$ is the restoring force of the microtubules in contact with the cell cortex, while G describes the force exerted by the motors [Grill et al, 2005]. In *S. pombe* no restoring forces by microtubules are present, thus K = 0 [Vogel et al, 2009]. In both models the force dependent detachment rate of the molecular motors plays a vital role, and can be written as

$$\omega\,(f) = \omega_0 \exp\,(f/f_c) \qquad Eq.\ 5$$

with the detachment rate ω_0 in the absence of force, the load force f and the characteristic force f_c. In the *C. elegans* embryo it is important to notice, that the motor detaches only from the microtubule, and that it is rigidly attached to the cortex. This assumption agrees well with the existence of membrane invaginations, which are caused by a cortex-bound force-generator, most likely dynein [Redemann et al, 2010]. In *S. pombe* dynein motors also detach from the cortex in response to load and eventually redistribute inside the cell. This redistribution leads to an increased positive feedback of the system, which can also be described as negative damping. In the *C. elegans* embryo the oscillations do not last as long as in *S. pombe*, and the build-up and die-down of the movement has to be explained additionally. If one wants to include the finding, that a threshold number of motors is necessary to generate oscillations, then a variable detachment rate has to be assumed [Pecreaux et al, 2006]. A decrease of the detachment rate from 1.5/s to 0.3/s during the 150 s of the oscillations is the consequence. How such a change in a rather fundamental motor property can be achieved *in vivo*, in particular during such a short time, is not known yet. There are indications, that dynactin influences the processivity of dynein [Kardon et al, 2009; King & Schroer, 2000], but the question how the (de-)activation of dynein or dynactin should be achieved in such a short time remains open.

1.4.3 Control of spindle length

The assembly of the mitotic spindle is a necessary prerequisite for mitotic cell division and the separation of genetic material into the two daughter cells. Molecular motors fulfill several different functions during the assembly of the mitotic spindle. Here I want to focus on the mechanism, which is responsible for setting the right length of the spindle.

Sharp et al. characterized mitotic spindles in the early embryo of *Drosophila melanogaster* after the loss of kinesin-5 function [Sharp et al, 1999]. These spindles collapse, which indicates, that the tetrameric motor kinesin-5 slides microtubules in the spindle apart. *In vitro* experiments show that kinesin-5 is indeed able to slide microtubules relative to each other in a (+) directed manner [Kapitein et al, 2005].

Null mutations of the kinesin-14 Ncd lead the other way around to abnormally long and unstable spindles [Kimble & Church, 1983]. As a next step the effect of a loss of kinesin-5 function in a Ncd null mutant was tested. Without the activity of any of these two motors, mitotic spindles do not collapse. These observations indicate, that kinesin-5 and Ncd antagonize each other in the mitotic spindle and are, therefore, responsible for setting the right spindle length [Sharp et al, 1999]. This result argues strongly for a force-balance, which has to be established between the (+) end directed motor kinesin-5 and the (-) directed motor Ncd (see Figure 4).

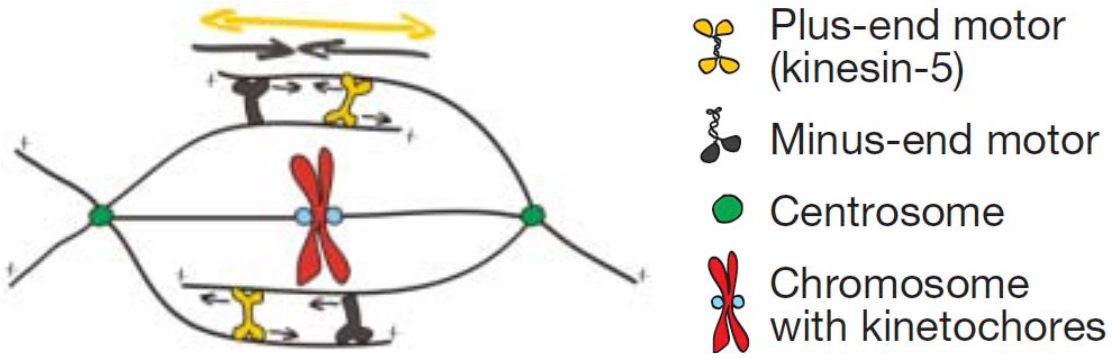

Figure 4. Antagonizing motors set the spindle length. Schematic of the mitotic spindle. (-) end directed motors (kinesin-14, e.g. Ncd), and (+) end directed motors (kinesin-5, eg. Eg5) antagonize each other and set the right spindle length by establishing a force balance. Figure from the group homepage of Prof. Schmidt, University of Göttingen (adapted from [Kapitein et al, 2005]).

In order to understand collective effects involving force regulation it is necessary to understand the molecular mechanisms of force regulation. *In vivo* Ncd is bound to two microtubules, via a motor domain on the C-terminus and a non-motor domain on the N-terminus. While the motor domain facilitates the force-generating power-stroke, the tail domain facilitates diffusion along the microtubule lattice. In a sliding assay Ncd can change its head-tail orientation between the two microtubules, so that it slides apart antiparallel microtubules and statically crosslinks parallel microtubules [Fink et al, 2009]. Similar results were obtained for the kinesin-14 from the fission yeast *S. pombe*, Klp-2 [Braun et al, 2009]. These experiments are good examples for combining single-molecule research with multi-motor assays in order to understand the *in vivo* function of the motor assembly.

It was also demonstrated that a passive crosslinking protein, ASE 1, is able to stabilize overlaps of microtubules, which would otherwise slide apart due to the activity of Ncd [Braun et al, 2011]. Thus force balances can also be influenced by pssive crosslinking molecules, which gradually slow down the activity of Ncd motors.

In the meanwhile more and more components of the spindle overlap zone are purified and combined in complex *in vitro* assays with the final aim to reconstitute spindle assembly [Bieling et al, 2010].

2 Introduction to the collective behavior of molecular motors *in vitro*

In this chapter I review the more recent efforts to understand the collective behavior of molecular motors by *in vitro* assays. In chapter 2.1 I discuss how multiple molecular motors influence each other in gliding assays. In chapter 2.2 I present several approaches to measuring the response of multiple motors to an external force. And in chapter 2.3 I present different experiments, which reconstitute antagonizing activity of multiple molecular motors.

2.1 Cooperativity of molecular motors

Cooperativity (or interference) of a chemical systems means, that the binding of a ligand to a receptor with multiple binding sites influences the affinity of the other binding sites. If one interprets, in a lose analogy, the microtubule as a receptor and the motors as ligands, then the question occurs, whether coupled motors can accelerate or slow down each other. In a more narrow definition cooperativity refers to the coupling of individual ATP-hydrolysis events and thus the synchronization of individual steps.

Already one of the first *in vitro* experiments with purified kinesin-1 revealed a difference between microtubules gliding on a surface with a high and a low motor density, respectively. At low ATP concentration many motors facilitate a slower gliding motility than only a few motors [Howard et al, 1989]. This counterintuitive finding may be explained by an inhibition of individual motors (either through a chemical, e.g. AMPPNP, or denaturation of the proteins). Consequently, a non-functional motor acts as a spring until its bond to the microtubule is broken and facilitates, therefore, a very simple mechanism for negative cooperativity.

New methods for surface preparation allow increasing the density of functional, specifically bound motors in a controlled manner up to > 10^4 μm^{-2}. Gliding experiments with truncated kinesin-1 on these functionalized surfaces yield, first, that the velocity decreases with increasing motor concentration (at saturating ATP). Second, this effect is more pronounced for constructs with a shorter coiled-coil, which are also stiffer, see Figure 5. Third, this effect is enhanced by low salt buffer, which increases the processivity of the motor [Bieling et al, 2008]. These effects can be interpreted as negative interference.

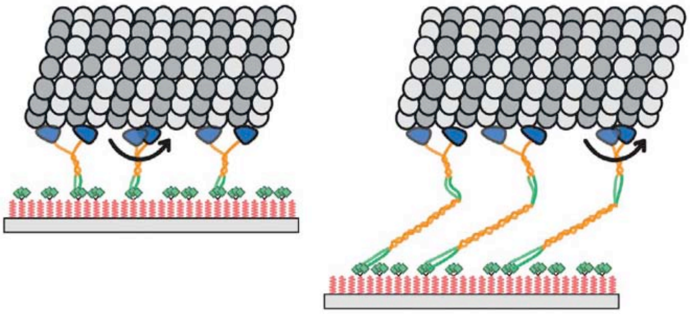

Figure 5. Stiff motors cause negative cooperativity. Schematic of two gliding assays with truncated (left) and wild type kinesin-1 (right). The shorter and stiffer kinesin-1 causes a slow down of gliding motility compared to the wild type kinesin-1. Figure taken from [Bieling et al, 2008].

In other experiments the deletion of a region between the neck and the stalk domain of kinesin-1 (called Hinge 1) leads at increasing motor densities to lower gliding velocities [Crevenna et al, 2008]. These experiments highlight, therefore, the function of kinesin-1's coiled coils in particular for multi-motor transport.

The fact that motors are often coupled mechanically (e.g. via microtubule and cargo/glass surface) leads to the question, in how far they might be able to synchronize individual steps. At least in a gliding assay the coupling via the surface is not sufficient to synchronize the stepping of kinesin-1 at low ATP [Leduc et al, 2007]. It is extremely unlikely that motors interfere positively *in vivo*, because the coupling via a biological, rather soft and often fluid-like cargo is weaker than in the previously mentioned *in vitro* experiment. Stepping experiments with exactly two coupled kinesin-1 motors do not show any difference in velocity compared to single stepping motors [Rogers et al, 2009].

A single, processive motor steps typically for about 1 µm along the microtubule before detachment. Intracellular cargo is often transported for much longer distances. It could be shown, that the run length of the cargo depends on the number of motors transporting the cargo. Beads decorated with high surface densities of kinesin-1 travel for a longer distance along the microtubule than beads decorated with low surface densities of kinesin-1 [Beeg et al, 2008; Coy et al, 1999].

2.2 How multiple motors work against a load

2.2.1 Theoretical concepts

Many experiments and theories are inspired by or even based on the seminal work from Jülicher and Prost describing the concerted action of large groups of molecular motors (with and without an external load) [Julicher & Prost, 1995]. In this model the collective motion of motors with two possible states (strongly and weakly bound) along a periodic potential (given by the nature of the filament) is studied. The transition between these two states can either be due to thermal fluctuations or due to ATP hydrolysis, i.e. stepping. The thermally driven transition depends on the potential difference along the filament. Jülicher and Prost showed that the velocity increases monotonically with the ATP concentration. In the presence of an external force there is, once the stepping rate surpasses a critical value, no stable solution for zero velocity. At this point small perturbations lead to spontaneous symmetry breaking and the systems reaches a stable velocity unequal zero. Similar dynamic transitions are known from statistical physics. Jülicher and Prost mention [Julicher & Prost, 1995]: "With an external force, the problem is formally equivalent to that of a magnetization in the presence of a magnetic field close to a paramagnetic-ferromagnetic critical point."

Other theoretical models focus on cooperative effects of a lower number of motors, which are more relevant for understanding cargo transport. Klumpp and Lipowsky found that the run length increases strongly with the number of motors, which agrees well with previous experiments. Furthermore they predicted force-velocity relationships for up to ten motors, which are monotonic and roughly linear. The relationship for positive velocities is given by [Klumpp & Lipowsky, 2005]:

$$v_n(F) = v\left(1 - \frac{F}{n\,F_s}\right) \qquad \textit{Eq. 6}$$

where $v_n(F)$ is the effective velocity of the motor ensemble (cargo) at force F, v the velocity of a single motor in the absence of force, n the number of bound motors and F_s the stall force of a single motor. The stall forces of N = 1, 2, 3,…10 available motors is predicted not to equal N F_s, since the number of bound motors n is likely to be lower than N. It should be noticed, that the detachment rate, which determines the number of bound motors, is force-dependent. Furthermore it is predicted, that intermediate forces (e.g. 12 pN for N = 5 motors with F_s = 6 pN each) lead to discrete peaks in the velocity distribution [Klumpp & Lipowsky, 2005]. This prediction implies, that a discrete and distinct numbers of bound and active motors n corresponds to a peak in the velocity distribution. Thus the motors are predicted to share the load effectively.

2.2.2 Optical tweezing of multiple motors

Several experimental approaches have been implemented to test the predictions of the theoretical models describing multi-motor dynamics. Experiments with an optical trap indicate, that the stall forces of dynein molecules (from bovine brain) are additive for up to three motors. Although multiple dyneins were found to undergo backward movement less frequently than single dynein motors, they still undergo backward movement more often than single kinesin-1 motors [Mallik et al, 2005]. This finding can be interpreted in different ways: Either the backward movement stems from force-dependent detachment, so that actually the detachment events or the backward stepping of only a single remaining dynein was measured. Or multiple motors are indeed able to step backward collectively. The stall force of a single motor in this particular experiment was, however, measured to be only 1 pN, so that forces less than 5 pN were sufficient to probe the behavior of multiple motors. Furthermore the number of simultaneously active motors was too low to probe the previously predicted collective effects [Mallik et al, 2005].

Normally, dynein and kinesin-1 stall around 7 pN, so that forces up to a hundreds of pN are necessary to probe the collective activity of these motors. The stiffness of optical traps is in general not high enough yet to exert such high forces. New approaches with coated microspheres allow, however, exerting optical trapping forces up to 100 pN and were already employed in multi-motor assays [Bormuth et al, 2008]. Furthermore, the geometry of the bead assay hampers the trustworthiness of optical tweezing experiments with multiple motors. Although stall forces can add up for two kinesin-1 motors, the force-velocity relationship of these two motors in an optical trap assay is not just a factor of two different from the single motor curve, see Figure 6. Essentially it turned out, that the elastic properties of the motors lead to a non-equal load sharing. Consequently a single motor often bears most of the load when a high external force is applied [Jamison et al, 2010].

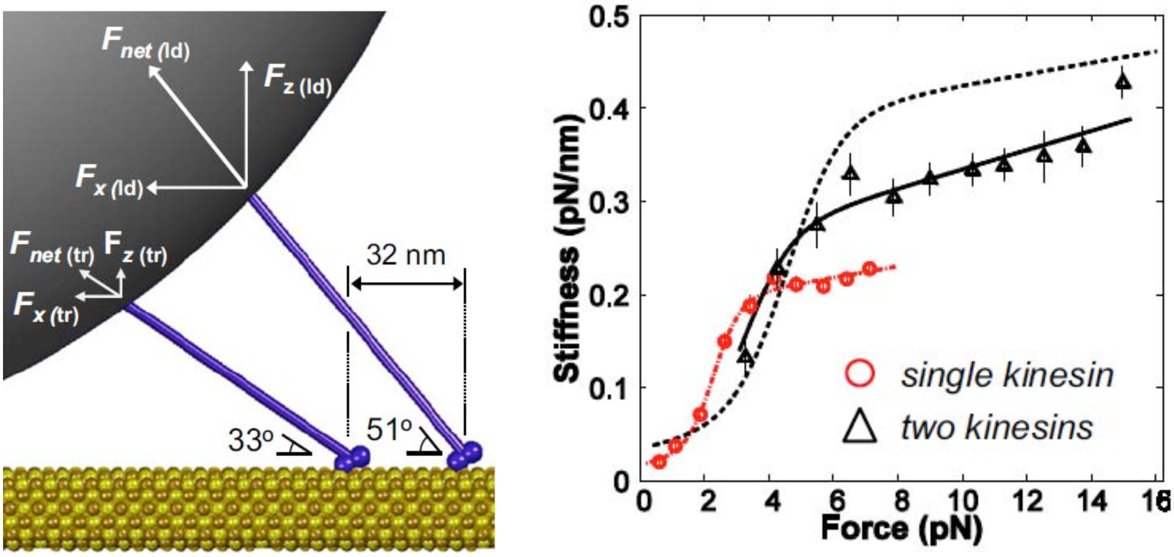

Figure 6. Two motors do not share their load equally. Left: Scheme of the experimental setup with two kinesin-1 motors (purple), the microtubule (yellow) and the trapped bead (black). The motors experience different loads due to the different angles with respect to the bead and the microtubule. Right: The measured effective stiffness of two motors (solid lines) does not correspond to the theoretically predicted stiffness of two motors, which share their load equally (dotted line). The experimental data shows a trend towards the single-motor behavior for the two-motor ensemble. Figure taken from [Jamison et al, 2010].

2.2.3 Alternative experimental approaches

Despite the great results, which were achieved with optical tweezers, there are three main problems with bead assays for probing multi-motor behavior: (1) Due to geometric reasons maximal ten motors are able to bind to the bead and the microtubule simultaneously. (2) The maximal force is limited to 100pN, often less. (3) The load is not distributed equally to the active motors.

In a gliding assays it is possible to probe the behavior of many (tens of) motors and the load is more equally distributed to the active motors. Several approaches based on gliding assays were developed to exert high forces on motors. External electric fields were employed to apply forces to gliding microtubules. The velocity of microtubules gliding on kinesin-1 coated channels was found to depend rather linearly on externally applied opposing forces. For assisting forces microtubules speed up and are able to reach velocities 4 x the velocity in the absence of force [Dujovne et al, 2008].

Another approach is based on applying forces through a superparamagnetic bead, which can easily be attached via the biotin-streptavidin system to gliding microtubules. So far forces up to 31 pN were employed to probe the reaction of several kinesin-1 motors [Fallesen et al, 2011a]. In this regime the number of active motors fluctuates significantly, and therefore the experimental setup corresponds rather to the situation described by Klumpp and Lipowsky [Klumpp & Lipowsky, 2005]. It was found, that the velocity distribution of the gliding microtubule shifts from a Gaussian distribution to a multi-modal distribution with increasing force. It is, however, difficult to identify discrete peaks and compare the velocity distribution quantitatively with the previously developed theories. In the simplest model all attached motors share the load equally. This assumption was tested by analyzing the velocity in dependence of the force per average number of motors $< n >$, which yields a normalized force-velocity relationship. At a constant motor density this number is proportional to the length of the microtubule. Within the errors this normalized force-velocity relationship seems to agree with single motor curves, so that the idea of equal load-sharing in a gliding assay is supported [Fallesen et al, 2011a; Geyer, 2008].

2.2.4 Membrane tube dynamics

Apart from cargo transport, filament sliding or positioning of microtubule structures, motors also work collectively to pull membrane tubes. Reconstitution of membrane tube extraction *in vitro* by kinesin-1 led to the conclusion, that motors accumulate on the tip of the membrane tube. Thus only the motors in the tip region carry a load. In a simple model it was assumed, that all motors in the tip region share the load equally, and that a linear force-velocity relationship is sufficient. As a result the on-rate of the kinesin-1 motor to the microtubule was calculated to be ~ 5/s [Leduc et al, 2004]. It should be, however, considered, that the motors diffuse in the membrane tube, and that attachment rates are likely to be higher in a gliding assay, where the motors are forced to orient towards the microtubule. Similar membrane tube experiments were carried through with the non-processive motor Ncd. It was shown, that multiple non-processive motors are able as well to pull membrane tubes. Since the necessary force for tube extraction is much higher (~ 25 pN) than the expected stall force of a single Ncd motor, this finding shows, that multiple Ncd motors are able to act collectively to generate high forces. The system exhibits not only growth, but also regimes of shrinkage. This bistable behavior is explained by the clustering of Ncd motors all along the membrane tube. If the leading cluster loses motors (due to detachment and subsequent diffusion within the membrane tube), it might not be able to withstand the force exerted by the membrane anymore. As a consequence the tube shrinks until it encounters another, sufficiently large motor cluster [Shaklee et al, 2008].

2.3 Antagonizing molecular motors

2.3.1 Competition between dissimilar motors

Soon after purified motors became available and microscopic methods allowed to carry through quantitative *in vitro* experiments, scientists started to aim at reconstituting bidirectional motor systems. Vale and coworkers were the first to observe gliding motility of microtubules on surfaces coated with different ratios of kinesin-1 and (axonemal or cytoplasmic) dynein [Vale et al, 1992]. They found that the microtubules moved at all investigated motor ratios persistently into one direction before they eventually changed their direction. The absolute microtubule gliding velocity in such an assay was, however, lower than the velocity of a microtubule gliding on only one kind of motor. Thus antagonizing motors interfere with each other by inducing detachment or slowing down the stepping rate. Once the symmetry of the system is broken, movement is stable until fluctuations of the number of attached motors, (+) end as well as (-) end ones, lead to a reversal of direction. The fact, that the distribution of switching follows the Poisson distribution argues strongly for an underlying stochastic process [Vale et al, 1992].

A biologically more relevant assay was established by studying the antagonistic behavior of kinesin-5 and the kinesin-14 Ncd in a gliding assay. It was found that, depending of the relative ratio of the two motor populations, the microtubules move either to the (+) end or the (-) end direction, but different than in the previously mentioned experiments by Vale et al. no switching between these two directions in one assay was observed. The microtubules reverse their direction of movement only at one particular relative motor concentration, where both motors establish a force balance. At this balance points the microtubules glide only for short distances before changing their direction, see Figure 7. For modeling simple linear (additive) force-velocity relationships were used. The attachment and (force-dependent) detachment of the motors was not taken into account. The effect of the antagonizing motor teams was instead described by a global friction coefficient [Tao et al, 2006].

Similar results (without a theoretical description) were obtained by studying the antagonism between kinesin-5 and kinesin-14 from *Xenopus laevis* in a sliding assay [Hentrich & Surrey, 2010].

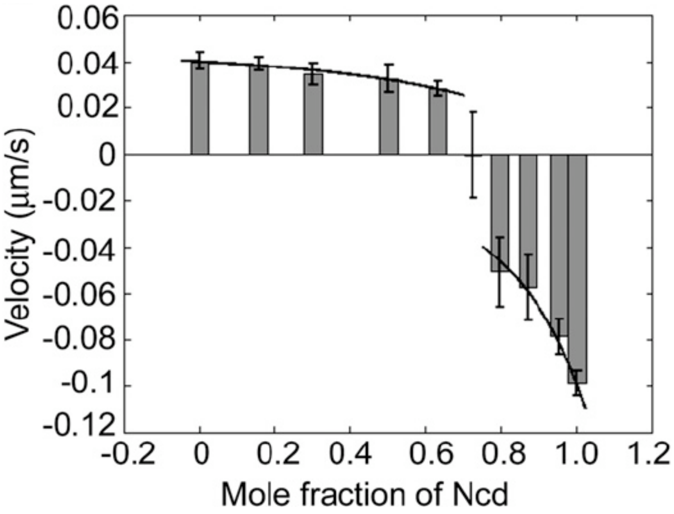

Figure 7. Bidirectional microtubule gliding by dissimilar kinesins. The gliding direction of microtubules changes in dependence of the ratio between the (+) end directed motor kinesin-5 and the (-) end directed motor kinesin-14. At the balance point movement in both directions is observed. The solid line indicates the best fit. Figure taken from [Tao et al, 2006].

2.3.2 Competition between identical motors

A simple way to probe the competition between identical motors is to observe the movement of motor decorated beads at microtubule intersections. With this assay the effect of motor number (via the motor surface density on the bead) was probed for kinesin-1 and the dynein-dynactin complex (from mouse or bovine brain). Multiple kinesin-1 motors tend to make a quick decision at the microtubule intersection and either pass the crossing or switch the filament and walk on, irrespective of the motor concentration. Dynein-dynactin on the other hand shows a more diverse behavior, i.e. dynein-dynactin decorated beads are more likely to reverse their direction of travel or unbind from the filament at the lowest investigated motor densitiy. At higher motor densities these beads are very likely to stall at the intersection [Ross et al, 2008]. Thus the number of motors might regulate the tethering function of dynein in cargo transport, see also the discussion in [Beeg et al, 2008]. Bidirectional movement in the gliding geometry was achieved by a single point mutation in the non-processive motor Ncd [Endow & Higuchi, 2000]. The mutation caused the motor to become non-directional in the sense that it did not prefer any direction of a microtubule but stepped randomly to the (+) end and (-) end. Nevertheless large groups of these non-directional motors facilitated directional gliding of microtubules until stochastic fluctuations induced a reversal of the gliding direction. Directional gliding becomes possible because coupling of the motors (via surface and microtubule) leads to a collective feedback. A theoretical description is based on a two-state model and leads to the conclusion, that the reversal time grows exponentially with the number of motors bound to the filament [Badoual et al, 2002].

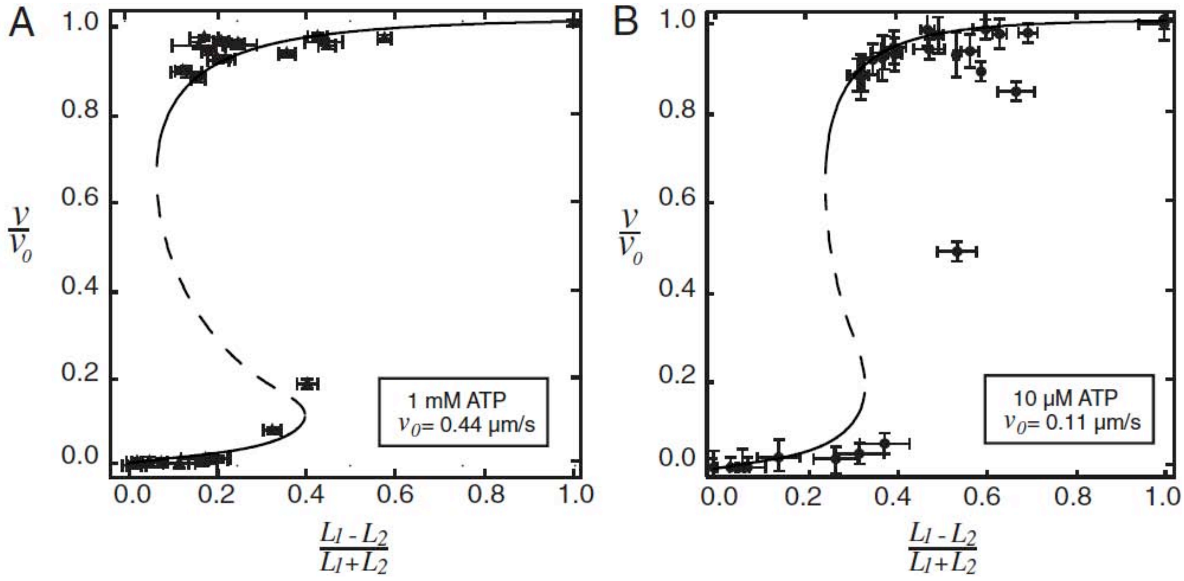

Figure 8. Superprocessive antagonizing kinesin-1 motors exhibit bistability. V indicates the gliding velocity of two antiparallel crosslinked microtubules, and v_0 the velocity of a single freely gliding microtubule. L_1 and L_2 are the lengths of the two antagonizing microtubules. The line indicates theoretical results; the dashed region is not stable. The motors in this assay exhibit a run length of more than 50 µm. Figure taken from [Leduc et al, 2010].

In order to probe the collective antagonistic behavior of the same kind of motor proteins, Leduc et al. invented an assay with exactly two antiparallel crosslinked microtubules (henceforth denoted doublets). The gliding velocity of these doublets was evaluated in dependence of the (normalized) length ratio of the two microtubules forming the doublet. In the doublet experiment the motor density is sufficiently high, so that fluctuations in the number of active motors can be neglected (different than in bead assays). Thus the length ratio of the microtubule corresponds directly to the ratio of antagonizing motors. Leduc et al. found, that superprossesive kinesin-1 motors with a run length > 50 µm are able to facilitate a bistability, meaning that two different velocities can be realized at a given length ratio of the doublet, see Figure 8. The theoretical mean-field approach for the experiments is based on the physical properties of individual motor proteins, such as attachment rate, force-dependent detachment rate, stiffness, stepping rate and the force-velocity relationship [Leduc et al, 2010]. A detailed description of the model is presented in chapter 5.3.

2.4 Aim of the project

In the introduction I laid out, how the research on molecular motors has been motivated by the observation of collective effects, such as muscle movement and chromosome oscillations. In the last two decades new technologies allowed studying single molecular motors and their dynamics in detail. Nowadays much is known about single motor properties, but our understanding of collective motor effects still remains poor. Recent efforts concentrated on putting the pieces together and reconstituting complex multi-motor behavior. The final aim must be to describe such complex behavior quantitatively, based on our knowledge about the single-motor properties. The particular questions I try to answer in my thesis work are the following:

(1) What is the force-velocity relationship of multiple dynein molecules? I tackle this question by combining magnetic tweezing with gliding assays [Geyer, 2008]. This approach allows exerting high forces (above 100 pN) and distributing them equally among the active motors.

(2) What is the dynamics of collectively antagonizing kinesin-1 and dynein motors with run lengths in the range of one up to a few µm?

(3) What is the dynamics of collectively antagonizing non-processive Ncd motors? I approach the latter two questions by employing the doublet assay [Leduc et al, 2010].

For probing the collective dynein properties I rely on a well-characterized minimal construct consisting of two dimerized heavy chains from *Saccharomyces cerevisae* (GST-Dyn1$_{331kD}$) [Gennerich et al, 2007; Reck-Peterson et al, 2006]. For the doublet assay I use additionally full-length kinesin-1 and a truncated Ncd construct with a GST tag at the tail (both from *D. melanogaster*).

Furthermore I aim at understanding the collective effects quantitatively based on single-motor properties. I employ related mathematical models for processive and non-processive motors and compare the experimental results to the theoretical description. Ideally it is possible to find an agreement between experimental observations and the theory with the input parameters of previous single-molecule experiments.

3 Characterization of molecular motors

In this chapter I present the characterization of the molecular motors, which I used for the experimental work described in chapter 4 and 5.

3.1 Results: The run length of processive motors

3.1.1 Run length of kinesin-1 at different ATP concentrations

In order to interpret the results of single- as well as multi-motor assays it is necessary to measure the basic properties of the molecules of interest. In the following experiments, presented in chapter 4 and 5, the run length is a particular important parameter. Thus the run length of kinesin-1 was measured at 1 mM and 7.5 µM ATP and the run length of dynein was measured at 1 mM ATP. The experiments were carried through with TAMRA labeled microtubules immobilized via anti-TAMRA antibodies on hydrophobic coverslips, which were then blocked by the polymer F127. The GFP tagged motors where flushed into the flow cell together with an oxygen scavenger system to diminish photobleaching and their stepping behavior along the microtubules was observed via laser based TIRF microscopy. For evaluation purposes the movies were converted into kymographs, see Figure 9, and the run length and velocity of the individual motors was measured.

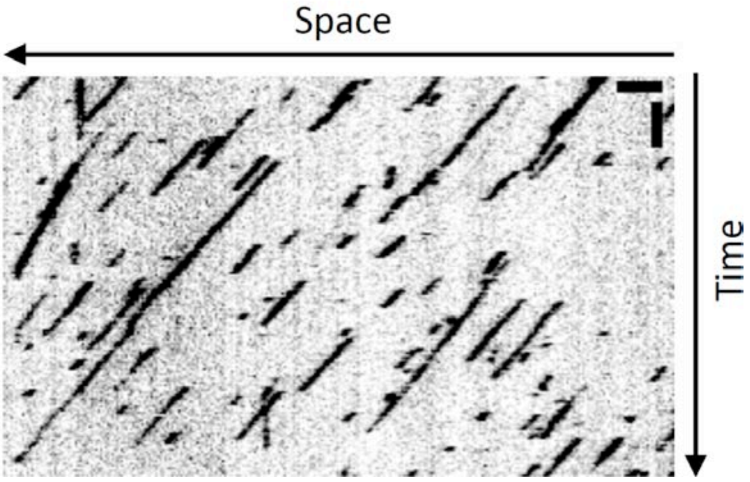

Figure 9. Kymograph of kinesin-1 stepping at 1 mM ATP. The spatial dimension is plotted horizontally (scale bar: 2 µm), the time dimension is plotted vertically (scale bar: 2 s). Nearly all motors (black) are functional and move with a similar velocity along the microtubule. The movie was acquired with a GFP tagged kinesin-1 and TIRF microscopy.

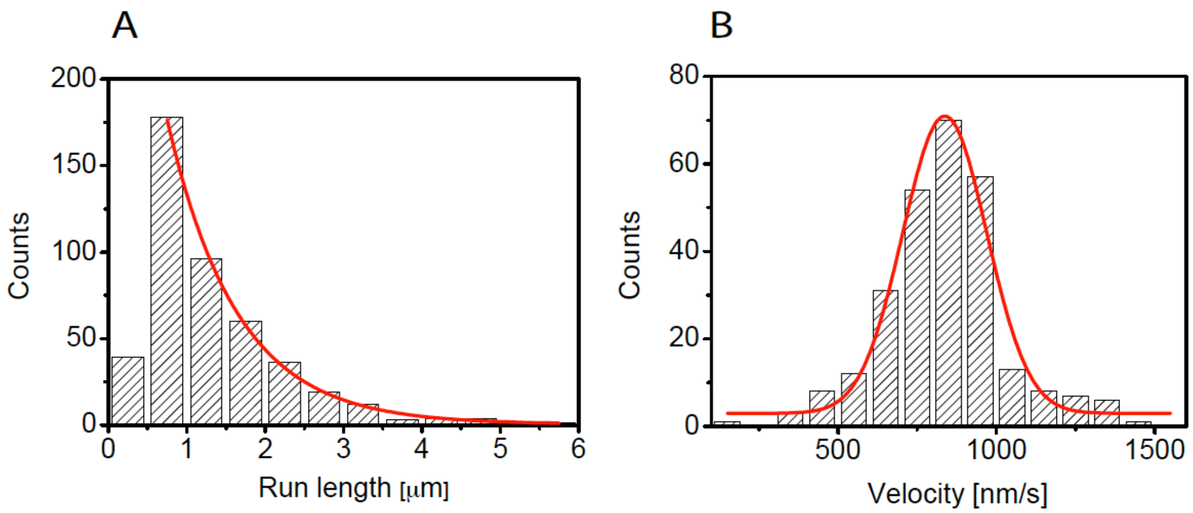

Figure 10. Run length and velocity of kinesin-1 at 1 mM ATP. A Histogram of the run length of kinesin-1 motors. The red line indicates a mono-exponential fit and yields a run length of 0.88 µm. The first bin from 0 - 0.5 µm was not considered in the fitting procedure. **B** Histogram of the velocity of kinesin-1 motors. The red line indicates a Gaussian fit with the central velocity of 837 nm/s. **A and B** The data was acquired with 1 mM ATP and 100% laser intensity.

A

LP [%]	Rl_{exp} $[\mu m]$	Δ Rl_{exp} $[\mu m]$	v $[nm/s]$	Δv $[nm/s]$	$\omega_{exp}[s^{-1}]$	Δ $\omega_{exp}[s^{-1}]$	n
5	1.92	0.19	804	13	0.419	0.048	146
41	1.33	0.21	848	8	0.629	0.107	271
78	1.15	0.04	837	8	0.737	0.032	550
100	0.88	0.03	837	8	0.951	0.042	454

B

LP [%]	Rl_{exp} $[\mu m]$	Δ Rl_{exp} $[\mu m]$	v $[nm/s]$	Δv $[nm/s]$	$\omega_{exp}[s^{-1}]$	Δ $\omega_{exp}[s^{-1}]$	n
5	1.75	0.44	117	4	0.067	0.019	67
41	1.10	0.24	118	1	0.107	0.025	127
78	0.78	0.07	115	3	0.147	0.015	157
100	0.58	0.02	110	2	0.190	0.009	225

Table 1. Result of stepping experiments with kinesin-1. A 1 mM ATP. **B** 7.5 µM ATP. LP refers to the relative laser power, Rl_{exp}, to the measured run length, v to the velocity, ω_{exp} to the measured detachment rate and n to the number of events. The errors Δ are the standard errors of the fitting parameters, while the error for the detachment rate is calculated according to error propagation.

The run length for a population of motors under given conditions was calculated by plotting all individual values in a histogram and fitting a single-exponential decay curve to the distribution, see Figure 10 A. The decay constant corresponds to the run length. The underlying assumption is, that the probability for detachment is constant per time interval. The velocity of the motor population was determined by fitting a Gaussian distribution to the histogram of the individual velocity values. The center of the Gaussian distribution corresponds to the average velocity of the motor population, see Figure 10 B.

In order to account for the effects of photo-bleaching, the run length was measured for different intensities of the illuminating laser light, see Table 1. The laser intensity was controlled by neutral density filters. The intensity of the attenuated laser light I was measured. I was used to determine the relative laser intensity I/I_{max} where I_{max} is the intensity without filter. Under the assumption, that the experimental detachment rate ω_{exp} depends linearly on the relative illumination intensity I/I_{max} it holds [Mashanov et al, 2004]:

$$\omega_{exp} = \omega_0 + I/I_{max}\,\omega_{pb} \qquad \text{Eq. 7}$$

where ω_{pb} is the photobleaching rate at I_{max}. Thus the real detachment rate ω_0 can be obtained easily by fitting a linear curve to the detachment rate$s$ ω_{exp} measured at different laser intensities, see Figure 11. The real run length Rl was calculated via the average velocity of the four velocity values obtained at different laser powers $\bar{v}$: $Rl = \bar{v}/\omega_0$. For kinesin-1 the resulting values are Rl (1 mM ATP) = (2.13 ± 0.30) µm and Rl (7.5 µM ATP) = (2.02 ± 0.28) µm (the error is dominated by the standard error of the fit for ω_0), and indicate that the run length of kinesin-1 is independent from the stepping rate of the motor. In other words, the intrinsic detachment rate (and, therefore, the time the motor is attached to the microtubule) does change with the stepping rate of the motor. Thus the underlying stochastic process, which leads to detachment, seems rather to depend on a particular part of the stepping cycle than on time per se. At decreasing stepping rates, kinesin-1 spends more and more time of its stepping cycle in the ATP waiting state. The experimental results presented here indicate, that the ATP waiting state is a strongly bound state. This finding is supported by previous measurements

[Verbrugge et al, 2009; Yajima et al, 2002], but different results were obtained as well [Schnitzer et al, 2000]. The absolute run length of about 2 µm is slightly higher than the typically measured values of 1 – 1.5 µm. Values up to 3 µm were, however, measured before [Dixit et al, 2008]. It is known that the salt concentration of the buffer influences the electrostatic interaction of the motor domain with the microtubule lattice and is, therefore, able to moderate the run length [Thorn et al, 2000]. Thus the slightly increased run length compared to previous experiments might stem from additional buffer components such as the oxygen-scavenger system, which contains charged components, e.g. glucose-oxidase and catalase.

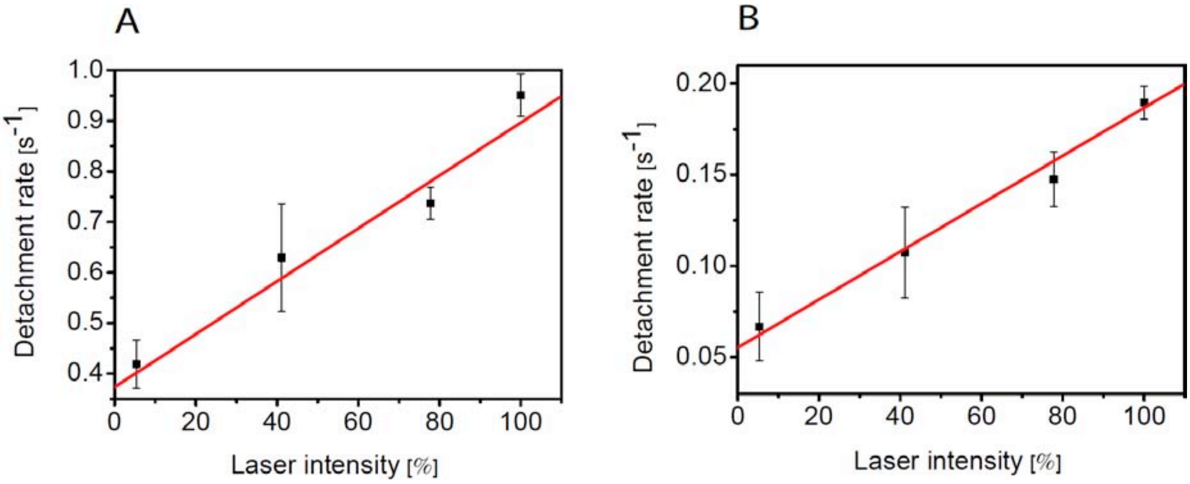

Figure 11. The run length of kinesin-1 is not ATP dependent. Squares: The experimental detachment rate ω_{exp} of stepping kinesin-1 at 1 mM ATP (**A**) and 7.5 µM ATP (**B**) is plotted against different intensities of the illuminating laser light. The experimental detachment rate was determined by $\omega_{exp} = v / Rl_{exp}$ with the velocity v and the experimental run length Rl_{exp} (see Figure 10 and Table 1). The error bars are thus dominated by the standard error of the fit for Rl_{exp}. In both figures the red line indicates a linear fit (weighted with the individual errors), which reveals the real detachment rate ω_0 via $\omega_{exp} = \omega_0 + I\ \omega_{pb}$ where I is the laser intensity and ω_{pb} the photo-bleaching rate. Thus ω_0 is corrected for photo-bleaching effects. The fits yield ω_0 (1 M ATP) = (0.39 ± 0.05) s^{-1} and ω_0 (7.5 µM ATP) = (0.057 ± 0.007) s^{-1} (standard error of the fit), which corresponds to Rl (1 M ATP) = (2.13 ± 0.30) µm and Rl (7.5 µM ATP) = (2.02 ± 0.28) µm.

3.1.2 The run length of cytoplasmic dynein

The run length of dynein was acquired and evaluated in the same manner as the run length of kinesin-1 (see chapter 3.1.1). A typical kymograph for the dynein experiment is shown in Figure 12. A typical histogram for the run length and velocity distribution is presented in Figure 13. It should be mentioned, that the stepping velocity of dynein $v_{st} \approx 140$ nm/s, see Table 2, differs significantly from velocity of microtubules gliding on dynein $v_{gl} \approx 60$ nm/s. The reason for this discrepancy is currently not clear, but since both, the stepping and the gliding assay, lead reproducibly to stable movement with a narrow distribution, there is no reason to assume a dysfunctional protein. Previously reported velocities for this construct (at the same buffer conditions used here with 30 mM HEPES + 50 mM KAcetate) lie between the stepping and gliding velocities measured here [Reck-Peterson et al, 2006]. A stepping velocity of only 45 nm/s was reported for a similar construct despite a slightly higher temperature (of 298 K), most likely due to a lower salt concentration of the buffer (30 mM HEPES without KAcetate) [Gennerich et al, 2007].

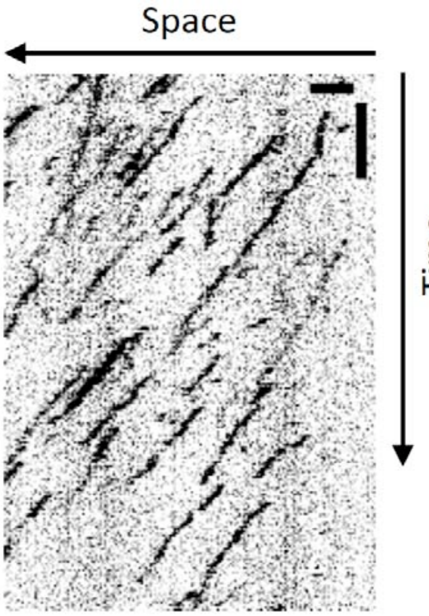

Figure 12. Kymograph of dynein stepping at 1 mM ATP. The spatial dimension is plotted horizontally (scale bar: 2 µm), the time dimension is plotted vertically (scale bar: 20 s). Nearly all motors (black) are functional and move with a similar velocity along the microtubule. The movie was acquired with a GFP tagged dynein construct from budding yeast and TIRF microscopy.

The dynein run length was also measured at different laser illumination intensities, see Table 2. Although the dynein construct has - like the kinesin-1 construct - 1 GFP per heavy chain, the recorded signal was lower, and therefore it was not possible to obtain data at the lowest illumination intensity. The real detachment rate

ω_0 was derived, too, by fitting the experimental detachment rate ω_{exp} against the illumination intensity with a linear curve in order to compensate for photo-bleaching, see Figure 14. The run length of 3.8 µm is clearly longer than the previously measured run length for this construct of about 2.4 µm (GST-Dyn1$_{331kD}$) [Reck-Peterson et al, 2006]. As mentioned in chapter 3.1.1 such a difference might occur due to an increased electrostatic interaction between the microtubule binding domain of the motor and the microtubule lattice, e.g. due to charged buffer components.

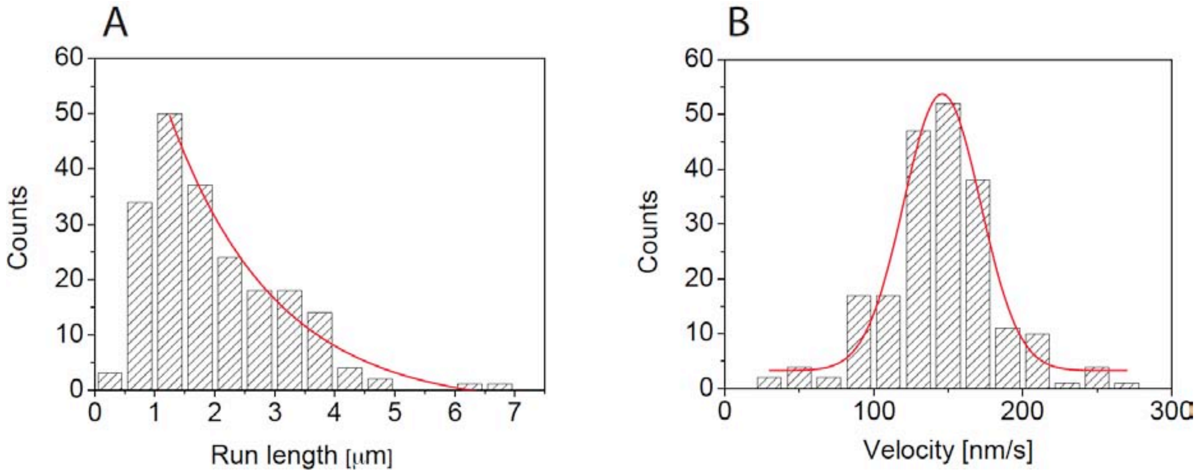

Figure 13. Run length and velocity of dynein at 1 mM ATP. A Histogram of the run length of dynein motors. The red line indicates the mono-exponential fit and yields a run length of 1.96 µm. The first bins from 0 – 1 µm were not considered in the fitting procedure. **B** Histogram of the velocity of dynein motors. The red line indicates a Gaussian fit with a central velocity of 147 nm/s. **A and B** The data was acquired with 1 mM ATP and 100% laser intensity.

LP [%]	Rl_{exp} $[\mu m]$	$\Delta\, Rl_{exp}$ $[\mu m]$	v $[nm/s]$	$\Delta\, v$ $[nm/s]$	$\omega_{exp}[\boldsymbol{s^{-1}}]$	Δ $\omega_{exp}[\boldsymbol{s^{-1}}]$	n
47	2.53	0.78	139	2	0.055	0.027	141
79	2.08	0.37	136	2	0.067	0.013	169
100	1.96	0.68	147	2	0.074	0.018	206

Table 2. Result of stepping experiments with dynein at 1 mM ATP. LP refers to the laser power, Rl_{exp} to the measured run length, v to the velocity, ω_{exp} to the measured detachment rate and n to the number of events. The errors Δ are the standard errors of the fitting parameters (exponential fit for Rl_{exp} and Gaussian fit for v) while the error for the detachment rate is calculated according to error propagation.

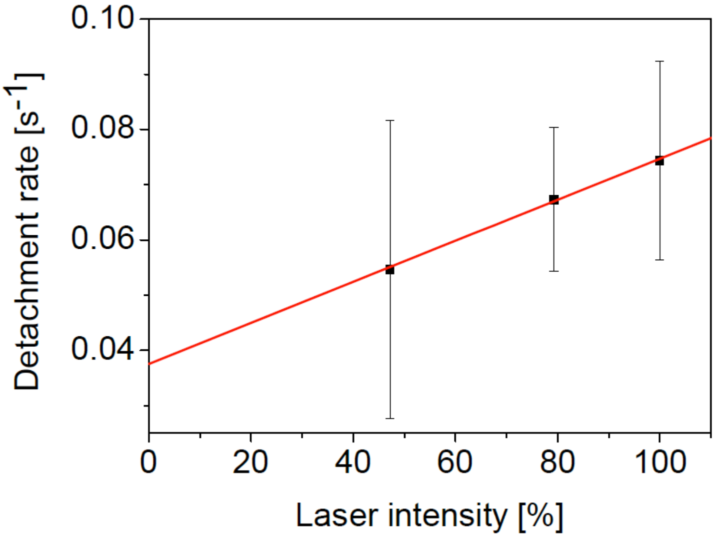

Figure 14. The run length of dynein at 1 mM ATP. Squares: The experimental detachment rate ω_0 of stepping dynein at 1 mM ATP is plotted against different intensities of the illuminating laser light. The experimental detachment rate was determined by $\omega_{exp} = v / Rl_{exp}$ with the velocity v and the experimental run length Rl_{exp} (see Figure 13 and Table 2). The error bars are thus dominated by the standard error of the fit for Rl_{exp}. The red line indicates a linear fit (weighted with the individual errors). Thus the real detachment rate ω_0 is corrected for photo-bleaching effects. The fit yields $\omega_0 = (0.037 \pm 0.001)\ s^{-1}$ which corresponds to the real run length Rl = (3.8 ± 0.2) μm.

3.2 Results for multi-motor gliding assays

3.2.1 The effect of ATP on the gliding motility

Characterizing the multi-motor behavior in the absence of load is a necessary prerequisite for understanding the collective behavior of antagonizing motors and of multiple motors acting against an external force. Here the gliding motility of multiple motors is characterized in the dependence of the ATP concentration, because the gliding velocity can be easily controlled via the ATP concentration. Thus changing the ATP concentration might allow for testing the velocity dependency of theoretical predictions, which describe how multiple motors act against a force or antagonize each other. Hence the gliding motility of TAMRA labeled microtubules was observed. The experimental results are presented in Figure 15, including a fit with the Hill equation [Hill, 1910]:

$$v = v_{max} \frac{[ATP]^n}{k_d + [ATP]^n} \qquad \textit{Eq. 8}$$

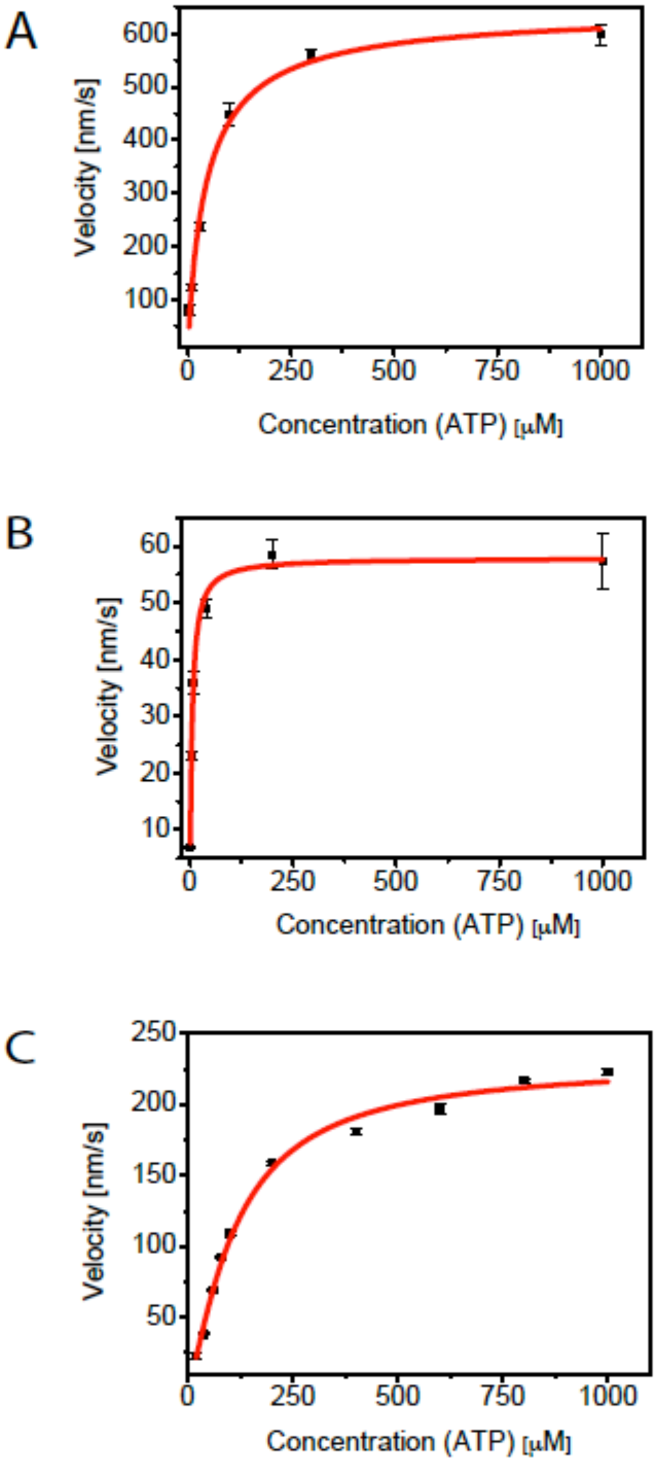

Figure 15. Hill curves describe the ATP dependency of gliding motility. A Kinesin-1 **B** Dynein **C** Ncd. The error bars indicate SEM and were used as weight for the fit. The Hill coefficients (Table 3) for kinesin-1 and dynein gliding do not differ significantly from 1 for kinesin-1 and dynein. Ncd mediated gliding shows a clearly positive cooperative effect with n > 1.

v is the measured gliding velocity, v_{max} is the maximal gliding velocity, [ATP] is the ATP concentration, k_d the dissociation constant and n the Hill coefficient, which describes the degree of cooperativity.

The Hill equation turns into the Michaelis-Menten equation for $n = 1$, for $n > 1$ ($n < 1$) the system cooperates positively (negatively). It was shown previously, that the Hill coefficient for kinesin-1 depends on the motor density and is generally $n \geq 1$ [Howard et al, 1989], while the ATP dependence of Ncd was so far only fitted with a Michaelis-Menten equations, which enforces $n = 1$ [deCastro et al, 1999].

The results for the fitting procedures are presented in Table 3. Kinesin-1 and dynein gliding can be described by Michaelis-Menten kinetics, since n does not differ significantly from 1. Ncd, however, shows a clearly positively cooperative behavior with $n > 1$. A new kinetic model for the Ncd powered gliding motility supports this finding (personal communication with Dr. B. Nitzsche, B CUBE, Dresden).

Motor	v_{max} [nm/s]	Δ v_{max} [nm/s]	k_d [µM]	Δ k_d [µM]	n	Δ n
Kinesin-1	645	41	46	10	0.92	0.14
Ncd	229	10	114	12	1.29	0.14
Dynein	57.9	1.7	5.7	0.7	1.08	0.15

Table 3. Fitting parameters for ATP dependent gliding according to the Hill equation. The Hill equation is given by $v = v_{max} [ATP]^n / (k_d + [ATP]^n)$ with the ATP concentration [ATP], the maximal velocity v_{max} and the dissociation constant k_d. $n > 1$ indicates positive cooperation.

3.2.2 The effect of temperature on the gliding motility

Temperature is an easily controllable parameter in biophysical assays (e.g. via an objective heater or a heating chamber), at least if no precision better than 0.5 K is needed. Increasing and decreasing the temperature might be a rather simple way to increase or decrease the velocity of gliding microtubules by changing the rate constant of ATP hydrolysis. Controlling the temperature might, therefore, offer new opportunities to test theoretical predictions in dependence on the gliding velocity (side to side with employing different ATP concentrations). The rate constant k of chemical reactions depends according to the Arrhenius equation on the activation energy E_a and the temperature T (with the exponential prefactor A and the Boltzmann constant k_B) [Atkins, 1996]:

$$k = Ae^{-E_a/k_B T} \qquad \text{Eq. 9}$$

In order to calibrate the temperature-velocity curve at 1 mM (and therefore saturating) ATP concentration of multi-motor gliding assays, I employed a Peltier element, which was connected via a heat-conductive paste to the backside of the cover slip [Korten et al, 2011]. A temperature feedback and constant heating/cooling guarantee stable temperatures over the whole field of view. In order to minimize the temperature gradient through the assay an air objective was used.

This experiment was performed for all three motors of interest, kinesin-1, Ncd and dynein. The velocity of the TAMRA labeled microtubules was evaluated either via filament tracking with a tracking software [Ruhnow et al, 2011] or with the help of kymographs. The natural logarithm of the measured velocities was plotted against the inverse of the temperature in order to obtain the activation energy via a simple linear fit, see Figure 16.

For fitting each dataset a single slope is sufficient, and thus only a single activation energy is necessary to describe each of the motor's temperature dependency. Thus the temperature is a good parameter for controlling the gliding velocity of microtubules. The activation energies for kinesin-1, Ncd and dynein all fall in the interval between 37 and 48 kJ/mol. Previously a slightly higher value for the activation energy of kinesin-1 was reported (50 kJ/mol by [Kawaguchi & Ishiwata, 2000]), and one measurement even indicates, that two different activation energies (65 and 9 kJ/mol) are necessary to describe the temperature dependence of kinesin-1 mediated microtubule gliding [Bohm et al, 2000]. It is not clear where the differences come from, but uncertainties in the temperature measurement would have a great effect. The data from Böhm et al. shows a highly increased error above 300 K, most likely due to denaturation of proteins.

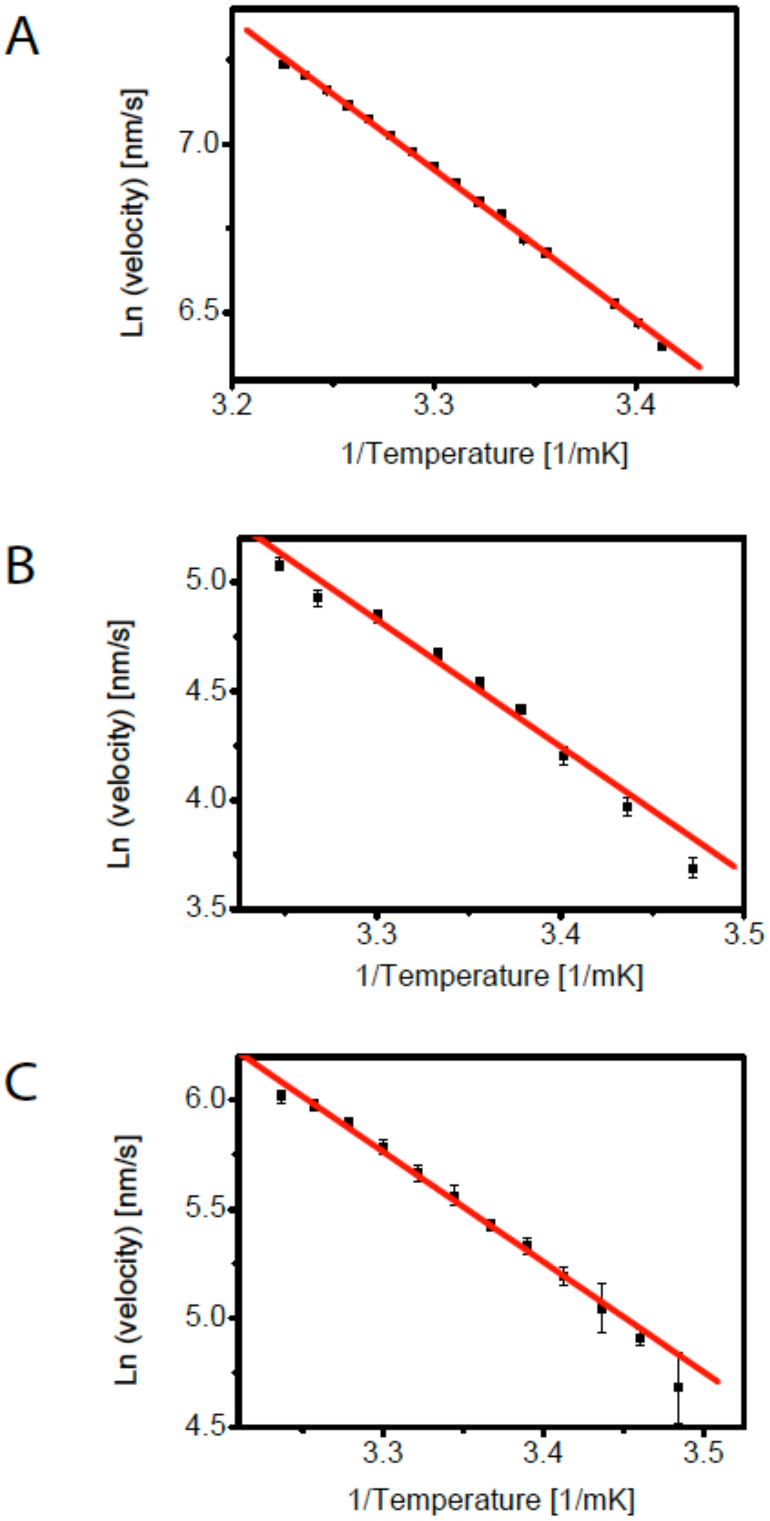

Figure 16. Arrhenius plot for kinesin-1, Ncd and dynein. A Kinesin-1 (data from V. Schroeder, MPI-CBG, Dresden) **B** Ncd **C** Dynein. The error bars indicate SEM. The activation energies are: E_a(kinesin-1) = (37.1 ± 0.1) kJ/mol; E_a(Ncd) = (42.0 ± 1.2) kJ/mol; E_a(dynein) = (48.3 ± 1.4) kJ/mol. The errors of the activiation energy are standard errors of the fit. The fit was weighted with the error (SEM) of the data points.

3.2.3 Bead transport does not influence gliding motility

The transport of superparamagnetic beads (diameter: 2.8 µm) by microtubules serves as a control for two experiments. It is a prerequisite for the tweezing work presented in chapter 4 that the presence of a bead does not influence the velocity of microtubule gliding. It is, furthermore, known, that at least kinesin-1 and Ncd rotate microtubules around their longitudinal axis in a gliding assay. The size of the bead suppresses any rotation of the microtubule. If the bead does not influence the velocity of microtubule gliding, it can be concluded that rotations of the microtubule are not necessary for proper motility. This is important for the doublet experiments presented in chapter 5, since two microtubules, which are connected along their long axis, cannot rotate while gliding. For dynein and Ncd mediated gliding microtubules with and without bead were analyzed from the same assay.

The velocity for dynein mediated gliding without bead was measured to be v_{Dyn} = (61.4 ± 1.2) nm/s (n = 45), while the velocity with bead was measured to be $v_{DynBead}$ = (59.4 ± 2.4) nm/s (n = 14) (both values are mean ± SEM; the data was analyzed via kymographs). As a control, the gliding motility of microtubules carrying a bead was also analyzed with an automated tracking software [Ruhnow et al, 2011], which fits a 2-dimensional Gaussian curve to the intensity distribution stemming from a bead. The center of the Gaussian curve corresponds to the tracked position data of the bead. This software was also employed for data analysis of the tweezing experiments presented in chapter 4. After tracking a running average of 3 frames was applied to the position data of the bead. Then the (tracked and smoothed) bead position of 10 consecutive frames (at frame rates of typically 30/s) was fitted against the time by a line. The slope of the line corresponds to the velocity of the bead. This evaluation yields $v_{DynBead}$ = (56.3 ± 1.5) nm/s (n = 6932 from 14 microtubules/beads, mean ± SEM). Thus the analysis via kymographs and automated tracking does not lead to significantly different values. The analysis of Ncd gliding leads, too, to the conclusion, that the presence of the bead does not influence the velocity of Ncd mediated gliding. The following values were measured via kymographs (mean ± standard deviation): v_{Ncd} = (192 ± 6) nm/s (n = 11) and $v_{NcdBead}$ = (188 ± 6) nm/s (n = 14). Previous experiments showed, that the velocity of kinesin-1 gliding was also not influenced by bead attachment [Geyer, 2008].

3.3 Discussion

In this chapter I characterized the run length, detachment rate and velocity of cytoplasmic dynein as well as kinesin-1. The measured values for the run length are slightly higher than expected (by about a factor of 2). The (stepping and gliding) velocity of kinesin-1 agrees well with literature values. The stepping velocity of dynein is higher than the gliding velocity (and values from literature). The raw data shows, however, that both, dynein and kinesin-1 motors, are fully functional. The discrepancy in run length and velocity might be easily explained by buffer conditions. The different velocities of stepping and gliding dynein hint at strong collective effects, which are not investigated further here. Alternatively, the surface immobilization of dynein might also lead to a reduced gliding velocity compared to the stepping velocity.

Interestingly, the run length of kinesin-1 does not depend on the ATP concentration. Vice versa the detachment rate of kinesin-1 from the microtubule does depend on the ATP concentration.

The ATP dependent gliding of dynein and kinesin-1 does not show significant cooperative effects. The ATP dependent gliding of Ncd shows, however, a clearly cooperative effect. This effect is confirmed by similar measurements in a neighboring laboratory (personal communication with Dr. B. Nitzsche, B CUBE, Dresden).

The activation energies according to the Arrhenius plot lie for all three motor proteins between 37 and 48 kJ/mol. Thus the temperature dependent kinetics of gliding motility is similar for all three motor proteins. The activation energy for kinesin-1 differs slightly from previous experiments.

Taken together it was possible to characterize the motor-proteins Ncd, dynein and kinesin-1 well under standard conditions, which were also used to carry through further experiments.

4 Magnetic tweezing of multiple molecular motors

In this chapter I describe the magnetic tweezing setup, which I used to probe the reaction of multiple dynein molecules towards a well-defined external force. Here I also present the results, in particular force-velocity curves of multiple dynein motors.

4.1 Concepts of the magnetic tweezing setup

As lined out in chapter 2 there are several different methods to apply external, well-defined forces onto molecular motors. In order to study the effects of a force on multiple motors I relied on magnetic tweezing in a gliding geometry. This technique allows exerting constant forces with inherent force-feedback in exactly one plane without a vertical component. Formulas and theoretical concepts are taken from [Jackson, 1998].

4.1.1 Theoretical concepts

Magnetism is the reaction of a material to a magnetic field. Moving electric charges and temporally varying electric fields can cause magnetic fields as described by the Maxwell equations. There are two commonly used vector fields, $\boldsymbol{B}$ and $\boldsymbol{H}$, with the name magnetic field (here vectors are denoted by bold letters). The $\boldsymbol{B}$-field can be defined via the famous Lorentz force (here without electric field), where the force $\boldsymbol{F}$ is measured, which acts on a particle with charge q and velocity $\boldsymbol{v}$:

$$\boldsymbol{F} = q \ \boldsymbol{v} \times \boldsymbol{B} \qquad \text{Eq. 10}$$

The $\boldsymbol{H}$-field is defined (in SI units) as $\boldsymbol{H} = \boldsymbol{B}/\mu_0 - \boldsymbol{M}$, where μ_0 is the permeability in the vacuum and $\boldsymbol{M}$ the magnetization of the material. Thus $\boldsymbol{H}$ considers the magnetic field, which is induced in the material by the external field $\boldsymbol{B}$.

The atomic basis of magnetism is the magnetic moment $\boldsymbol{m}$ an electron exerts. In a semi-classical picture the electron circles around the nucleus on discrete orbits, which correspond to discrete energy levels. This movement of a charge results in a magnetic moment $\boldsymbol{m} = e/(2\, m_e)\, \boldsymbol{L}$ with the electron mass m_e, the electric charge e and the angular momentum $|\boldsymbol{L}| = n\, h$ where n is a positive integer and h the Planck constant. The minimal magnetic moment $m_B = e/(2\, m_e)\, h$ is called Bohr's magneton.

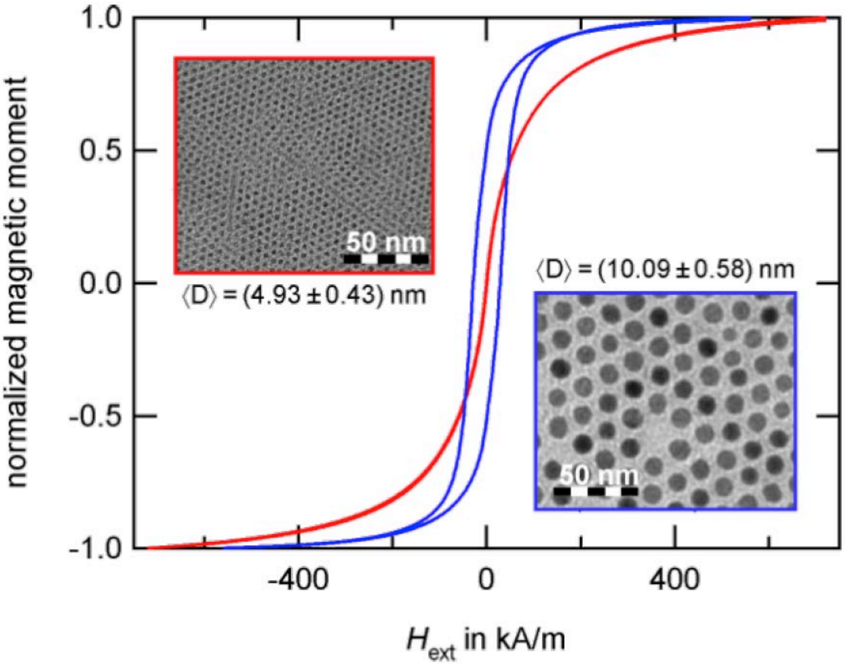

Figure 17. Magnetic moments of nanoparticles at room temperature. The larger Co particles with a diameter of about 10 nm show a hysteresis (blue), while the small particles with half the diameter are superparamagnetic (red). Figure taken from [Weddemann et al, 2010].

The magnetic moments of a material align if an external field is applied. Paramagnetic materials only show magnetic behavior when an external field is applied. In paramagnetic materials the energy, which is necessary to change the direction of the magnetic moments, is comparable to room temperature. Therefore no macroscopic magnetization can be observed in the absence of a magnetic field.

In ferromagnetic materials coupling forces between the magnetic moments lead to an alignment of neighboring magnetic moments. In the absence of a magnetic field many magnetic moments align spontaneously and form so-called Weiss-domains. Once all magnetic moments are aligned in a ferromagnetic material, energy above the level of thermal energy at room temperature is necessary to change the orientation of the Weiss-domains. Thus ferromagnetic materials, once magnetized, exhibit a magnetization even in the absence of a magnetic field. Superparamagnetic particles are single-domain ferromagnetic particles with a size of several nm. Due to their small size they show paramagnetic behavior. The small number of magnetic moments in such a particle results in a low coupling energy.

Therefore the thermal energy at room temperature is sufficient to change the direction of the magnetic moments randomly. Figure 17 shows the effect of size on the magnetic properties. While very small particles show superparamagnetic behavior, slightly larger particles exhibit already a hysteresis and belong therefore to the class of ferromagnetic particles. Superparamagnetic particles combine the advantages of paramagnetic particles – the absence of a hysteresis – with the high magnetic susceptibility of ferromagnets. The magnetic susceptibility χ_v characterizes the magnetization $\boldsymbol{M}$ in dependence on the magnetic field $\boldsymbol{H}$ and is defined as:

$$\boldsymbol{M} = \chi_v \, \boldsymbol{H} \qquad \textit{Eq. 11}$$

where $\chi_v > 0$ is defined as paramagnetism and $\chi_v >> 0$ as ferromagnetism; the case $\chi_v < 0$ is referred to as diamagnetism and not discussed here. In general the magnetic susceptibility is not (as assumed here) a scalar but a tensor.

In the case of an ideal paramagnetic material the Langevin equation is the analytic solution for describing how the magnetic susceptibility depends on the magnetic field B: $\chi_v = coth(x) - 1/x,$ with $x = \mu\, B/(k_B T)$, where $k_B T$ is the thermal energy and μ the permeability of the material, which can also be expressed as $\mu = \mu_0(1 + \chi_v)$. The force acting on a superparamagnetic particle is given by [Shevkoplyas et al, 2007]:

$$\boldsymbol{F} = \left(\boldsymbol{m_p} \, \nabla\right) \boldsymbol{B} \qquad \textit{Eq. 12}$$

where $\boldsymbol{m_p} = \rho\, V\, \boldsymbol{M}$ is the magnetic moment of the whole particle (with the density ρ and the volume V).

For measuring forces of motors pulling or pushing a microtubule no forces perpendicular to the axis of interest should be present, while the force along the axis of interest should be maximized. A bar magnet was designed by V. Geyer, Dresden, MPI-CBG, to serve exactly this condition [Geyer, 2008]. If the beads lie in a centered line in front of (and close to) one of the sides of the bar magnet, then Eq. 12 can be simplified. Since the bar magnet is several orders of magnitudes larger than the beads, the magnetic field lines are perpendicular to the magnet's front and parallel to each other. In this case $\boldsymbol{M}$ has only one component and the force acting on the bead can be written as:

$$F_i = \rho\, V\, M_i \frac{\partial B_i}{\partial_i} \qquad \textit{Eq. 13}$$

where i is the coordinate in direction of the magnetization $\boldsymbol{M}$. Further considerations concerning the size and shape of the magnet are discussed in [Geyer, 2008].

4.1.2 Implementation

Here the assay and the technical setup are described. Dynein with a GFP tag on its tail was specifically immobilized to the surface of a glass capillary via anti-GFP antibodies. Control experiments without anti-GFP antibodies showed that no dynein bound unspecifically to the surface. The motors propelled TAMRA labeled and biotinylated microtubules, to which streptavidin coated superparamagnetic beads were bound, see Figure 18. As shown before (in chapter 3.2.3) the beads did not influence the gliding motility.

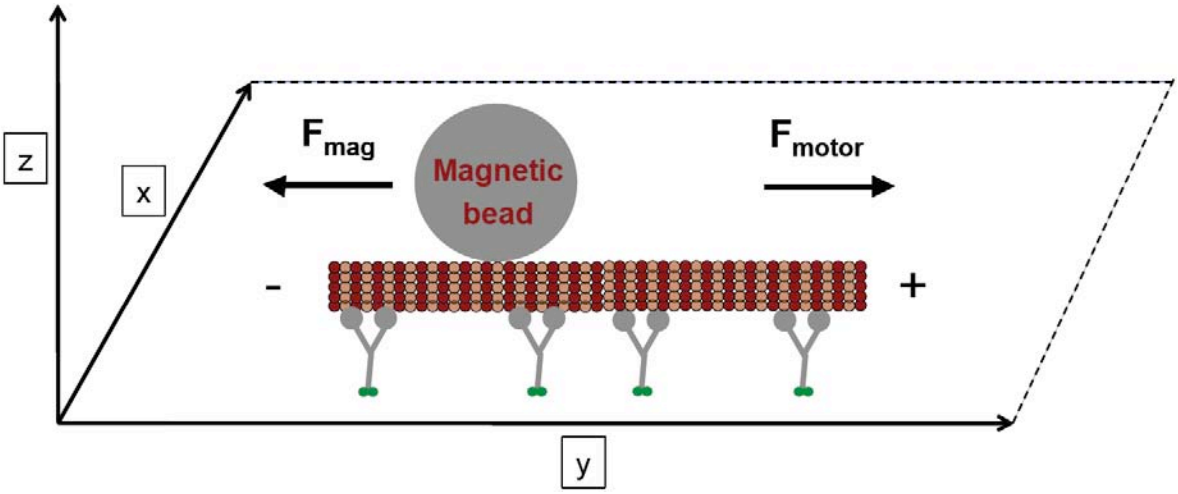

Figure 18. Scheme of the magnetic tweezing assay. Molecular motors are bound via a specific tag to the glass surface, e.g. dynein with GFP at its tail can be bound via anti-GFP antibodies. The motors propel biotinylated microtubules, to which a streptavidin coated superparamagnetic bead (2.8 µm, not drawn to scale) is bound. A well-defined magnetic force can be exerted via a bar magnet to the bead and therefore to the motors. If the motors propel the microtubule to the right direction, then the force opposes the action of the motors.

A rectangular glass capillary of nominal 145 μm wall thickness was used. The effective thickness at the corners is larger, since the profile of the capillary is not perfectly rectangular. Thus the magnet could approach the probing bead down to a distance of 250 μm.

After flushing the different solutions through the capillary it was mounted onto a standard microscopy stage. Once the beads were in focus, the capillary was not moved any more, see Figure 19.

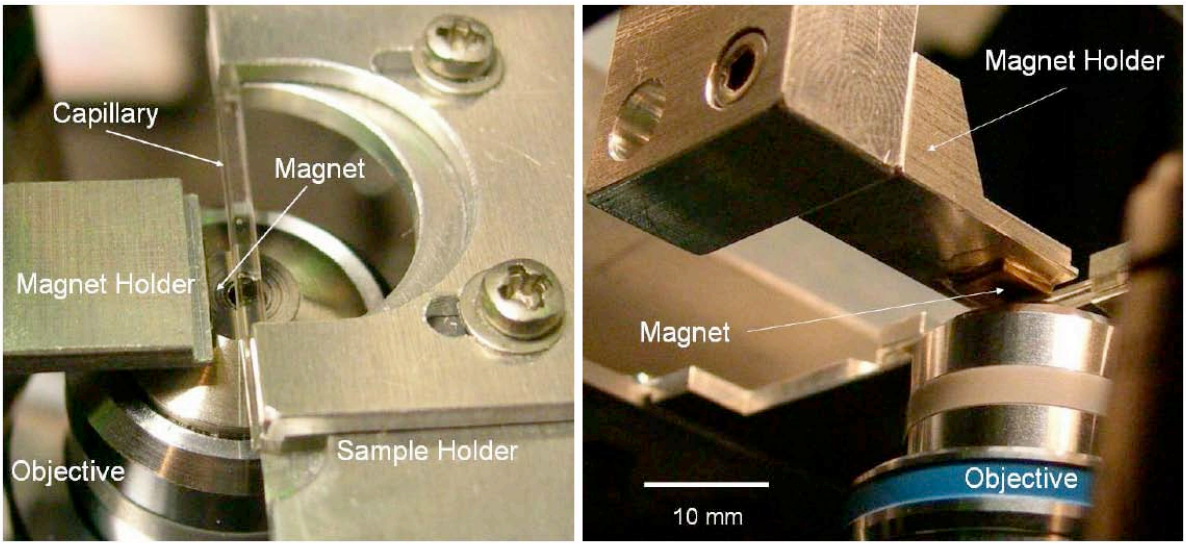

Figure 19. Magnet positioning in the magnetic tweezing setup. The magnet is fixed to a holder, which can be translated freely in all three dimensions with the help of piezo driven positioning devices. The capillary is mounted independently from the magnet. The magnet and the capillary are parallel to each other. Figure taken from [Geyer, 2008].

The force was applied via a bar magnet, which provided a high gradient in the imaging plane perpendicular to the long axis of the capillary (x-direction), and a very low gradient parallel to the long axis of the capillary (y-direction). The edge of the magnet is oriented parallel towards the capillary. The force along the vertical axis (z-direction) was minimized by calibration of the magnet position. Measurements with floating beads in a viscous medium allowed calibrating the forces in dependence on the magnet position, in particular on the distance towards the center of the field of view. The calibration provided ideal values for the z- and the x-position and a table of positions along the y-direction with the corresponding forces. The calibration was carried through once and was subsequently used for all other measurements. In order to set the absolute distance of the magnet toward the center of the field of view accurately before each measurement, a reference point on the bottom of the magnet was used. This reference point was aligned with a digital mask covering the field of view.

A problem arose, in particular at high forces (small distances bead - magnet): The applied force varied over the field of view due to the high gradient of the magnetic field, which spanned typically 205 µm (40x objective) or 82 µm (100x objective). The force differences could be easily determined from the calibration procedure. Here "distance" refers to the distance from the edge of the magnet to the center of the field of view. Thus the force difference from the center to the edge of the field of view was at 2000 µm distance +0.37 pN and -0.32 pN (40x) or +0.14 pN and -0.13 pN (100x), respectively, and at 1000 µm distance it was +1.6 pN and -1.4 pN (40x) or ±0.6 pN (100x), respectively. With the force of 9.9 pN at 1000 µm distance and 2.2 pN at 2000 µm distance, the relative force error from the edge to the center of the field of view was about 15% for the 40x objective and about 6% for the 100x objective. The magnetic bead moved (due to the low velocity of dynein) even in long movies not further than 10 µm. If the bead position was on average another 10 µm away from the center of the field of view then the effective error due to a difference between the nominal and the real position of the bead was around 3%. Thus the force error in direction of the magnet was dominated by inhomogeneities of the magnetic properties of the single beads. The forces along the vertical axis (z-direction) were negligible; this is in general an advantage of the magnetic tweezing setup in combination with a gliding assay compared to optical tweezing experiments based on the bead assay.

During the actual measurements the position of the magnet was changed via motorized stages. The magnet position could be changed arbitrarily and typically either the reaction of the motors towards a constant force or to a stepwise increasing and decreasing force was measured. Ideally the microtubule was aligned antiparallel to the external magnetic force, meaning that the microtubule glided in the direction opposite of the external magnetic force. In the following section only measurements of microtubules with an angle of less than 20 degree towards the x-direction are considered. The microtubules typically aligned (parallel or antiparallel) along the direction of the applied force. A direct conversion of the applied forces for microtubules with more than an angle of 20 degree was not considered, because it is difficult to account for the effect of sideward forces, which are also able to slow down motors [Block et al, 2003].

The movement of the beads is observed via their autofluorescence with a conventional fluorescence light microscope (see methods). The microtubule and the bead are visible in the same channel (TAMRA filter), but the peak intensity is typically 10 x times higher than the intensity stemming from the microtubule. In combination with a custom-built particle-tracking program [Ruhnow et al, 2011], it is possible to determine the velocity of the bead with high precision.

4.1.3 Calibration

In order to measure force-velocity relationships, it is necessary to control the applied magnetic force with high precision. The force calibration was carried through by measuring the velocity of beads with a well-defined mass and radius in a medium with high viscosity (Brookfield Silicone Fluid, nominal 500 mPas, real: 482 mPas) in dependence of the position of the magnet (for details see [Geyer, 2008]). The beads were imaged at least 50 µm above the surface of the capillary (with a 100x objective) to avoid any distortion of the bead movement by the walls of the capillary. The calibration procedure helped, furthermore, to define the correct vertical position of the magnet (perpendicular to the applied force). The force due to gravitation led in the silicone oil to a slow vertical displacement of 0.6 µm in 100 s. Weak trapping forces along the vertical direction (with 0.01 pN/µm at 1200 µm magnet-bead displacement) helped, furthermore, to prevent vertical displacements of the bead (simulation according to [Geyer, 2008]). The position of the magnet was set in such a way, that no additional displacement in the vertical direction due to magnetic forces was observed. This reference value for the magnet position was used for all following force measurements. (This value differs slightly for 100x and the 40x objective, the force calibration in direction of the magnet remained, however, unaffected by changing the objective.) The force was calculated according to Stoke's law assuming laminar flow [Landau & Lifschnitz, 1991]:

$$\boldsymbol{F} = 6\pi\eta\, r\, v \qquad \text{Eq. 14}$$

with the viscosity η, the radius r, and the velocity $\boldsymbol{v}$ of the magnetic bead. The calibration curve is presented in Figure 20.

It is desirable to employ beads with a high magnetization in order to exert high forces up to many pN and a low variation in size, mass and magnetic properties to guarantee faithful force measurements. Previous calibration measurements with the same setup were carried through with beads of 2.8 µm diameter (Dynabeds M-270) [Geyer, 2008]. The actual measurements presented here were carried through with beads of the same diameter (Dynabeads M-280), assuming very similar properties for both batches of beads, see also [Geyer, 2008]. The actual calibration with the Dynabeads M-280 was conducted after the measurements with motor proteins, and it turned out that these beads were much more heterogeneous in their distribution of size and/or mass of the superparamagnetic material. Therefore the error in the potentially biologically relevant measurements was higher than technically necessary.

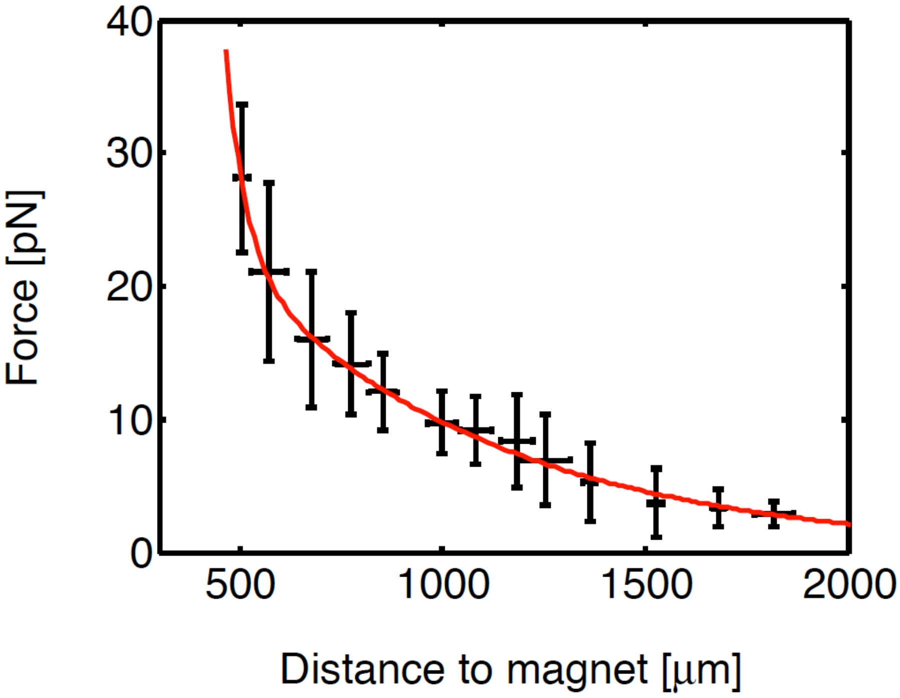

Figure 20. Calibration of the magnetic tweezing setup. The data points indicate mean values, the error bars standard deviations. The red curve is a bi-exponential fit. The fit values are used to calculate the force at a given distance of the edge of the magnet to the imaging plane.

4.2 Results of multi-motor force measurements

4.2.1 External force leads to microtubule re-orientation

It was shown that magnetic forces in the pN range are able to guide microtubules gliding on kinesin-1 motors [Geyer, 2008]. I tested, whether such guidance can also be achieved for microtubules gliding on dynein motors. If the long axis of the microtubule was not aligned with the direction of the magnetic force, then the microtubule bended, see Figure 21. Bending (and eventually turning) requires an anchor point, which acts as a hinge, and in a gliding assay a motor protein fulfills this function. Thus the pivoting point indicated the position of a motor protein. The discrete displacement of a gliding microtubule under force can, therefore, be used to determine the surface motor density [Fallesen et al, 2011b]. In Figure 21 a typical redirection of a microtubule due to a magnetic force in the pN range is shown. The pivoting point is marked by the yellow asterisk and indicates the position of a dynein motor protein.

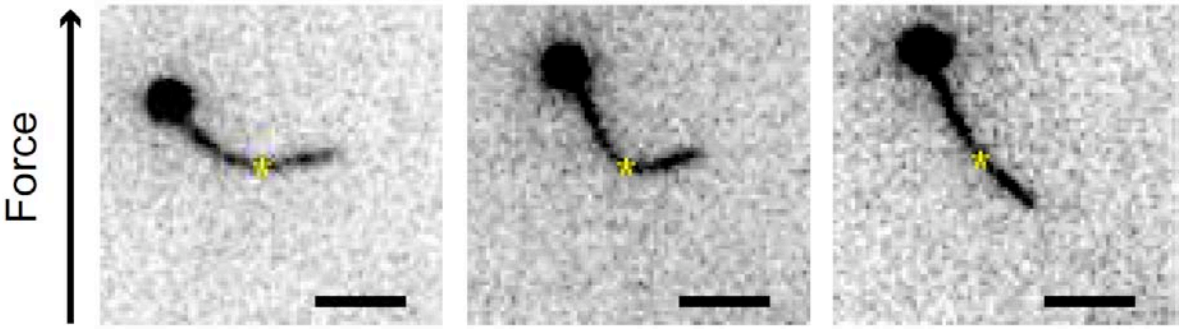

Figure 21. Magnetic beads align gliding microtubules in a magnetic field. In the image series the force (in the pN range) due to the magnetic field is directed towards the top. 20 seconds lie between the first (left) and the last (right) image. Initially the microtubule travels to the left (with the bead on the leading side). The yellow asterisk indicates the pivoting point of the microtubule. Thus a hinge, here a motor protein, is located at the indicated position. A second motor at the end of the microtubule unbinds between the second (middle) and the last (right) image. Scale bar: 10 µm.

The re-orientation of a microtubule was not always as obvious as shown in Figure 21. Tracking the position of the bead allowed localizing it with a precision of about 30 nm, which was necessary for determining the velocity of the bead (and therefore the microtubule). Tracking quantum dots, which were attached to the microtubule, allowed increasing the tracking precision even further, down to 5 - 10 nm.

Combining magnetic tweezing with TIRF allowed the imaging of quantum dots, which could be attached – as the magnetic beads – via the biotin-streptavidin bond to microtubules. The tracking of quantum dots enabled e.g. to observe discrete back- and sideward movement, which arose from the detachment of a motor protein. In Figure 22 the raw tracking data of the quantum dot was plotted for a typical example with a constant force of 23.5 pN. Here the x coordinate was perpendicular to the magnetic force while the y coordinate was antiparallel to the magnetic force. Thus forward movement of the microtubule with respect to the opposing external force was directed towards positive y values, see Figure 18. In Figure 22 the x (red) and the y (black) coordinate were plotted against the time (running average with window size 5 of the tracked position data). First the microtubule stalled and 4 - 5 motor were pulling against the load. After 5 seconds the microtubule re-orients abruptly including a backward jump of about 50 nm. The most plausible interpretation for such a discrete backward movement is, that one motor detached from the microtubule. Upon re-binding the microtubule moved again very slowly forward.

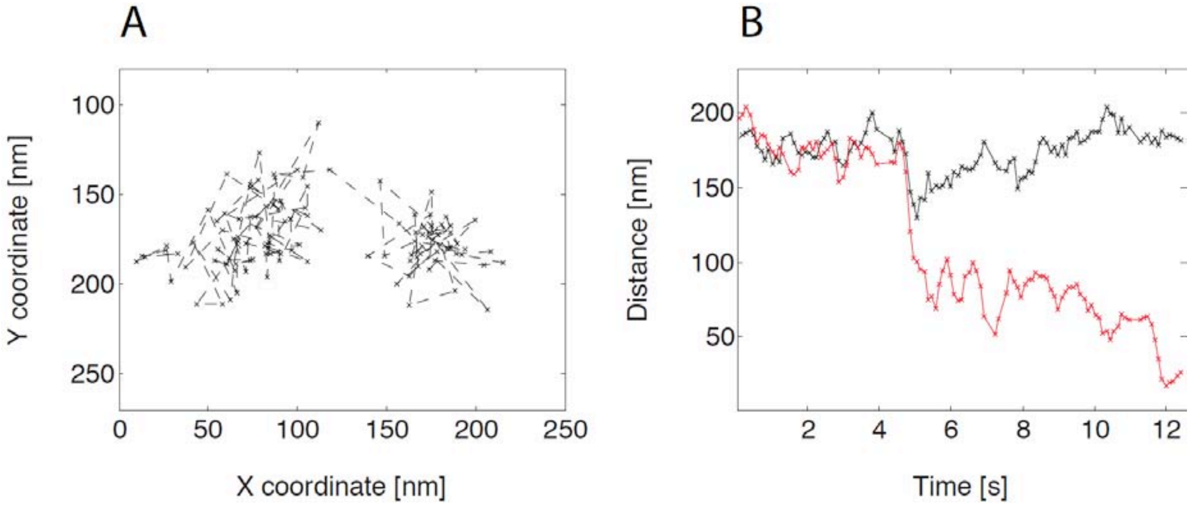

Figure 22. Quantum dot tracking reveals motor detachment. A Raw tracking data of a quantum dot attached to a microtubule with two magnetic beads. The opposing force was constantly 23.5 pN. The x coordinate is perpendicular and the y coordinate is antiparallel to the magnetic force. Forward movement of the microtubule against the external force is directed towards positive values of the y coordinate. **B** X (red) and the y (black) coordinate against the time of the event in A.

4.2.2 Cytoplasmic dynein is able to withstand high opposing loads

Once a microtubule was aligned with the gradient of the magnetic field, its velocity could be measured and interpreted easily. In Figure 23 the travelling distance of a gliding microtubule along the y-axis (antiparallel to the magnetic force) is plotted together with the applied force against the time. The force intervals were 3 seconds long and increased in steps of slightly more than 2 pN. The velocity decreased with increasing force until the microtubule eventually stalled at around 20 pN. In order to obtain a force-velocity relationship from such a dataset, the measured force-displacement relationship was fitted with a line; the slope indicated the velocity. The velocities were then plotted as a function of the force.

In Figure 24 two typical force-velocity relationships are shown, both were obtained from a series of increasing or decreasing force values as depicted in Figure 23. It is remarkable, that the microtubule moved backward consecutively for several seconds. Such backward movement implies that all the motors attached to the microtubule step backward. Backward stepping indicates, furthermore, that the applied force was higher than the cumulative stall force of the motors. Thus the motors were able to withstand forces above their cumulative stall force.

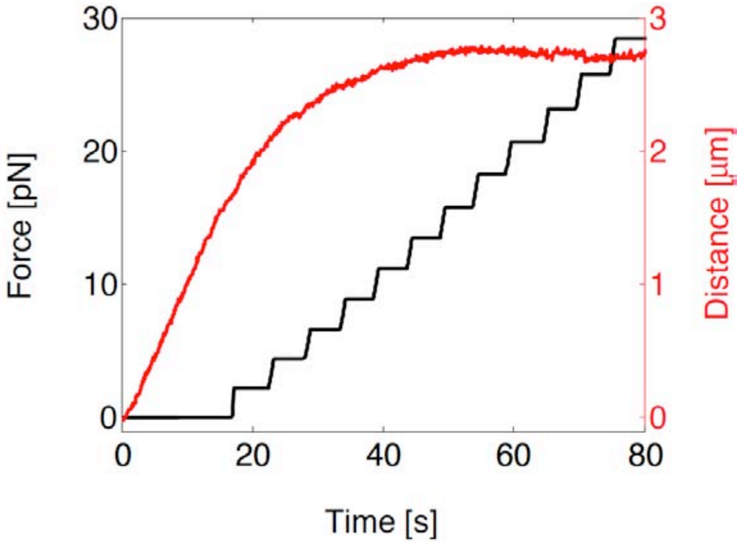

Figure 23. Example of force induced slowdown. The force (black) and the distance along the y-axis in direction of the magnet (red, running average of 5 frames) is plotted against the time. The data stems from a quantum dot attached to a microtubule (with two magnetic beads). This data is recorded at an effective frame rate of 10/s. The low frame rate is due to the long illumination time for quantum dot imaging.

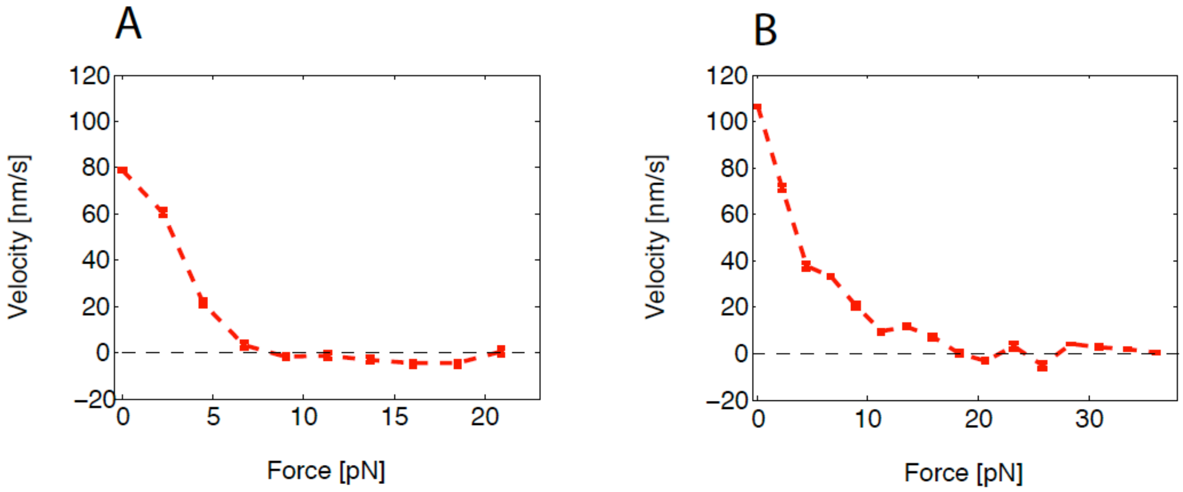

Figure 24. Examples of multi-motor force-velocity relationships. A Force-velocity relationship for an event with maximal three motors according to the GFP signal. Two motors are active according to the stall force of about 9 pN. Remarkably the motors withstand the force and walk backward for about 25 s. **B** The force-velocity relationship was obtained with 2 beads attached to the microtubule. The stall force of about 20 pN corresponds to 4 motors. The data corresponds to Figure 23. In A and B the errors display the standard error of the linear regression for each force plateau.

4.2.3 Force-velocity curves at very low motor densities

One of the main challenges in characterizing the response of several motor proteins to a force is to control the number of active motor proteins accurately. In a recent approach a DNA construct was used to attach two kinesin-1 motors 50 nm apart from each other to a bead [Jamison et al, 2010]. In a gliding assay fluorescently labeled motors were employed to determine the number of motors via TIRF microscopy. I immobilized GFP-tagged dynein via anti-GFP antibodies to the glass surface and combined the established tweezing assay with TIRF. Once acceptable TIRF conditions were found, the number of motors was determined by recording a time-lapse in the green channel (until all GFP molecules were bleached). Then the normal tweezing procedure with lamp illumination and TRITC filter was carried through. The two channels were aligned after acquisition manually via the signal of the TetraSpeck beads, which emit light in both, the red and the green channel.

Figure 25 A shows an overlay of the maximum-intensity projection of the green channel and one time point of the red channel for a typical example. The bleaching steps in Figure 25 C of the green fluorescence signals show that only a single motors and not a cluster of them was present at the position marked in Figure 25 A.

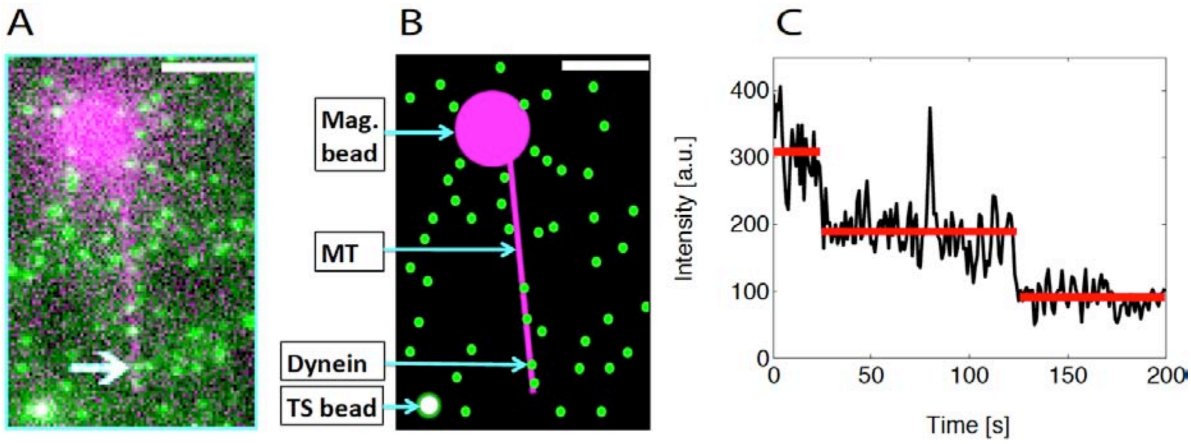

Figure 25. Combining tweezing and TIRF allows for counting single motors. A Fluorescence image of a tweezing event at very low motor densities. The GFP (green) channel was recorded prior to the TRITC (magenta) channel to observe the bleaching steps of GFPs associated to single motors (2 x GFPs per motor). The magnetic force is directed towards the upper side of the image. Scale bar: 5 µm. **B** Schematic of the fluorescence image in A where "Mag." abbreviates magnetic, "MT" microtubule and "TS" TetraSpeck **C** The intensity profile of the marked motor in A (arrow) is shown in black. In red the average intensity over the respective time intervals is plotted to visualize the bleaching steps. The two bleaching steps are a clear signature of a single motor protein (with 2 x GFPs).

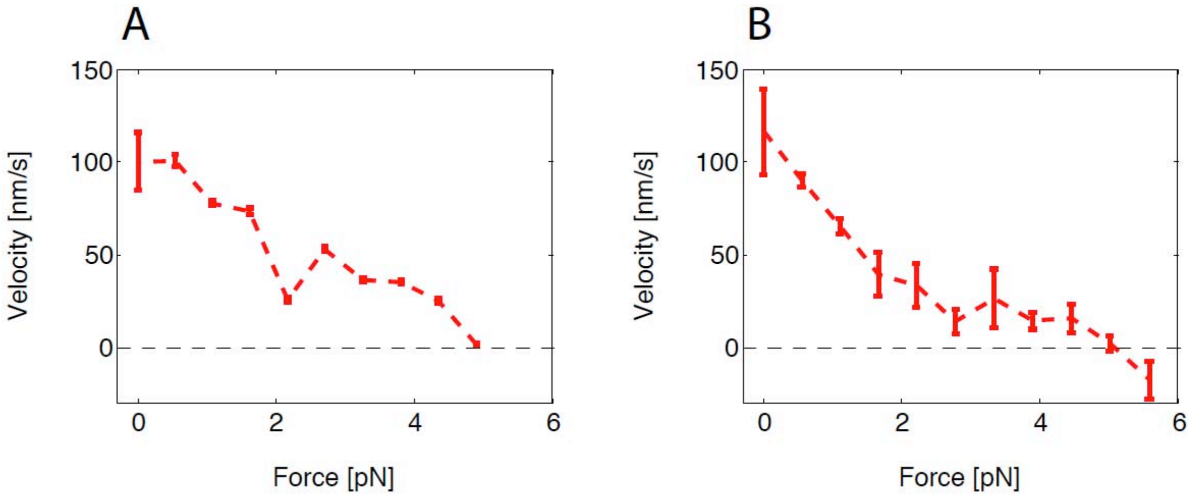

Figure 26. Examples of single-motor force-velocity relationships. A The data corresponds to Figure 25. Apart from one outlier the force-velocity relationship is roughly linear and exhibits a stall force corresponding to a single motor. The error bars display the standard error of the linear fit. **B** Here 2 - 4 velocity values (obtained from one microtubule within one movie) are averaged per force plateau. The movie lasts 195 seconds, in which the microtubule moves 7 µm forward and about 1 µm backward. The stall force of 5 pN corresponds to one motor. The error bars display SEM.

The force-velocity curve corresponding to this event is shown in Figure 26 A. The stall force of 5 pN and the corresponding, roughly linear force response indicates that most likely only one motor was actively pulling against the load. The stall force of 5 pN agrees well with published values for the same dynein construct [Gennerich et al, 2007]. The hypothesis, that only one motor was active, is in accordance with the analysis from the fluorescence image, which limits the number of active motors to 3.

Furthermore several events as the one in Figure 26 B showed backward movement of microtubules under force. Such backward movement implies, that multiple motors were able to walk backward processively. It might, however, be possible, that short backward movements were caused by the detachment of a motor protein from the microtubule. An example of such a backward jump is shown in Figure 22.

4.2.4 Averaging of multi-motor force-velocity relationships

In order to characterize the force-velocity curves of multiple dynein motors, I normalized and plotted 322 data points from 24 individual force-velocity curves in one diagram, see Figure 27. The 24 curves were selected according to the quality of the raw data (e.g. the angle between the microtubule and the y-axis should be constant and maximal 20 degree). Furthermore the microtubule should slow down significantly due to the applied force (minimal velocity < 0.25 maximal velocity) and the slow-down should be continuous to exclude obvious cases of motor detachment. No assumption was made about the shape of the force-velocity curve. All selected curves showed, however, a linear trend for positive velocities (forward movement). The velocity values were normalized to the velocity in the absence of load, $V_{F=0}$, and the force values were normalized to the stall force, F_{stall}. $V_{F=0}$ and F_{stall} were calculated separately for each of the 24 datasets. Thus each force-velocity curve was normalized individually. For each curve the values for $V_{F=0}$ and F_{stall} were obtained by fitting the positive velocities with a line and determining the intercepts. The values for $V_{F=0}$ lie between 116 nm/s and 47 nm/s, the mean ± standard deviation is given by 85.8 ± 15.5 nm/s. The values for F_{stall} lie between 25 pN and 4.5 pN, and the mean ± standard deviation is given by 12.5 ± 4.8 pN. If one assumes, that the stall forces are additive, it follows (together with the stall force of 5 pN) that between 1 and 5 motor were active at stall force in the individual events. In Figure 27 the red values indicate mean ± standard deviation of the velocities, binned in intervals of 0.1 F/F_{stall}. The averaged force-velocity curve (indicated by the red dashed line) can be well described by a bilinear function with a single slope above stall force. Thus the multi-motor force-velocity curve in a gliding assay seems to differ from the single-motor force-velocity curve measured in an optical tweezing bead assay.

A single slope above stall force is not sufficient to describe the previously published single-motor curve [Gennerich et al, 2007]. It should be noticed, however, that the previously published single-motor force-velocity curve was obtained with a slightly different construct ($Dyn1_{471kDa}$) than the one used here ($GST\text{-}Dyn1_{331kD}$) (and under slightly different buffer conditions). Most importantly, the different orientation of the applied force in the optical tweezing bead assay and in the magnetic tweezing gliding assay can lead to differences in the force-velocity relationships.

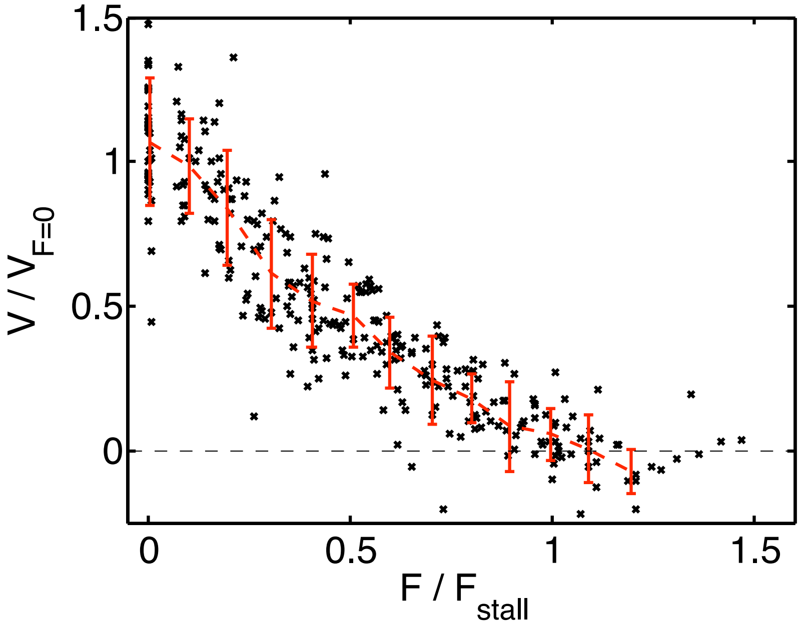

Figure 27. Normalized force-velocity relationship of multiple dynein motors in a gliding assay. 322 normalized data points from 24 force-velocity curves are plotted in black. The 24 force-velocity curves were fitted separately to obtain the stall force, F_{stall}, and the velocity in the absence of load, $V_{F=0}$. The velocity and force values were then normalized to $V_{F=0}$ and F_{stall}. The red data points indicate mean ± standard deviation, binned in intervals of 0.1 F/ F_{stall}.

4.3 Discussion

In this chapter I described a new approach based on magnetic tweezing for measuring the force-velocity relationship of single and in particular multiple dynein motors in a gliding geometry. I presented force-velocity relationships of single and multiple motors. Furthermore, I showed how to detect single surface-immobilized GFP tagged motor proteins with TIRF microscopy in combination with the magnetic tweezing setup. I demonstrated how the number of active motors could be estimated via the fluorescence signal of the surface immobilized motor proteins.

Averaged force-velocity curves of multiple but few motors (up to 5) could be described by a linear function above stall force. In this respect multiple dynein motors seem to differ from single dynein motors. In order to exclude effects, e.g. due to surface immobilization or due to the different orientation of the externally applied force compared to the optical tweezing bead assay, further single-motor force-velocity curves should be obtained in the gliding geometry as a control experiment. The limiting factor was here, however, that microtubules together with 2.8 µm sized beads exhibit very low binding rates towards the surface immobilized motors. The size of the bead prevented the microtubule in many cases from approaching the surface. Sequential flushing of the channel with microtubules and beads was not feasible at very low motor densities, because microtubules were flushed out too easily. It is, therefore, more promising to focus in future experiments on the regime of higher motor densities and to probe the reaction of more than 10 motors bound to a single microtubule. At higher motor densities it is, furthermore, justified to assume a direct relationship between the length of the microtubule and the number of attached motors. For such experiments it might be necessary to employ even bigger beads to exert even higher forces and to increase the binding strength between bead and microtubule. A single biotin-streptavidin bond cannot withstand several hundred pN. Once this problem is overcome, the assay can be applied directly to other motor proteins.

It would be of great interest to use the gliding geometry in order to probe the force-velocity curve of motors with two microtubule binding domains, e.g. native axonemal dynein and native Ncd. In such an experiment one microtubule would be fixed to the surface, while another probing microtubule would be attached to a bead. This geometry would be very similar to the native configuration within the axoneme (for axonemal dynein) or the spindle (for Ncd). It would be particularly interesting to probe the force-response of multiple Ncd motors, because its non-motor microtubule binding domain is known to facilitate diffusion along the microtubule [Fink et al, 2009]. Thus it would be possible to measure how two different mechanisms, diffusion and stepping, contribute to a highly stable, yet dynamic spindle structure.

5 Reconstitution of antagonizing motor activity

In this chapter I describe the assay for probing the collective behavior of antagonizing molecular motors. Here I present the results obtained with kinesin-1, dynein and Ncd as well as the theories for describing the experimental data.

5.1 The doublet assay

As reviewed in chapter 2.3, several approaches have been implemented to probe the behavior of antagonizing molecular motors. In most assays motors of different polarities were used, e.g. kinesin-1 and dynein. This complicates the theoretical description, because different parameters have to be employed to model the behavior of each of the motor teams. In order to understand the physical principles governing the collective effects of antagonizing motors it is necessary to design an assay, in which multiple motors of one kind compete against each other. Unequal load distribution due to geometric effects such as different angles of the motors to each other (and therefore to the mutual load force) should be avoided. Furthermore the assay should mimic the geometry of antagonozing motors *in vivo*, e.g. the dynein-driven nuclear oscillations during the meiotic prophase of the fission yeast *S. pombe*. The gliding assay of antiparallel crosslinked microtubules, so-called doublets fulfills all these requirements and is depicted in Figure 28, see also [Leduc et al, 2010].

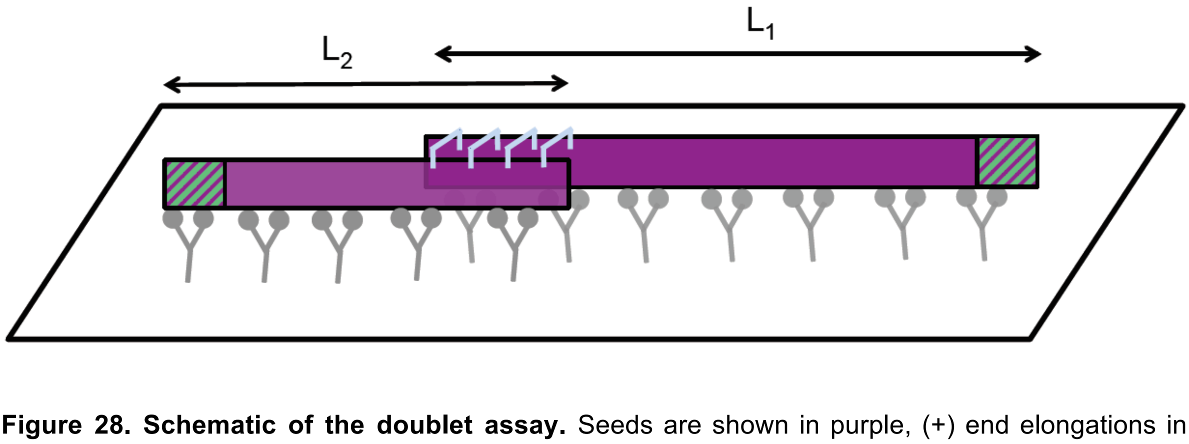

Figure 28. Schematic of the doublet assay. Seeds are shown in purple, (+) end elongations in purple/green. Two dual-color polarity marked microtubules are crosslinked via anti-tubulin antibodies (light blue brackets) and form antiparallel doublets. The doublets glide on motor proteins (grey). The lengths of the two microtubules correspond to the number of motors antagonizing each other.

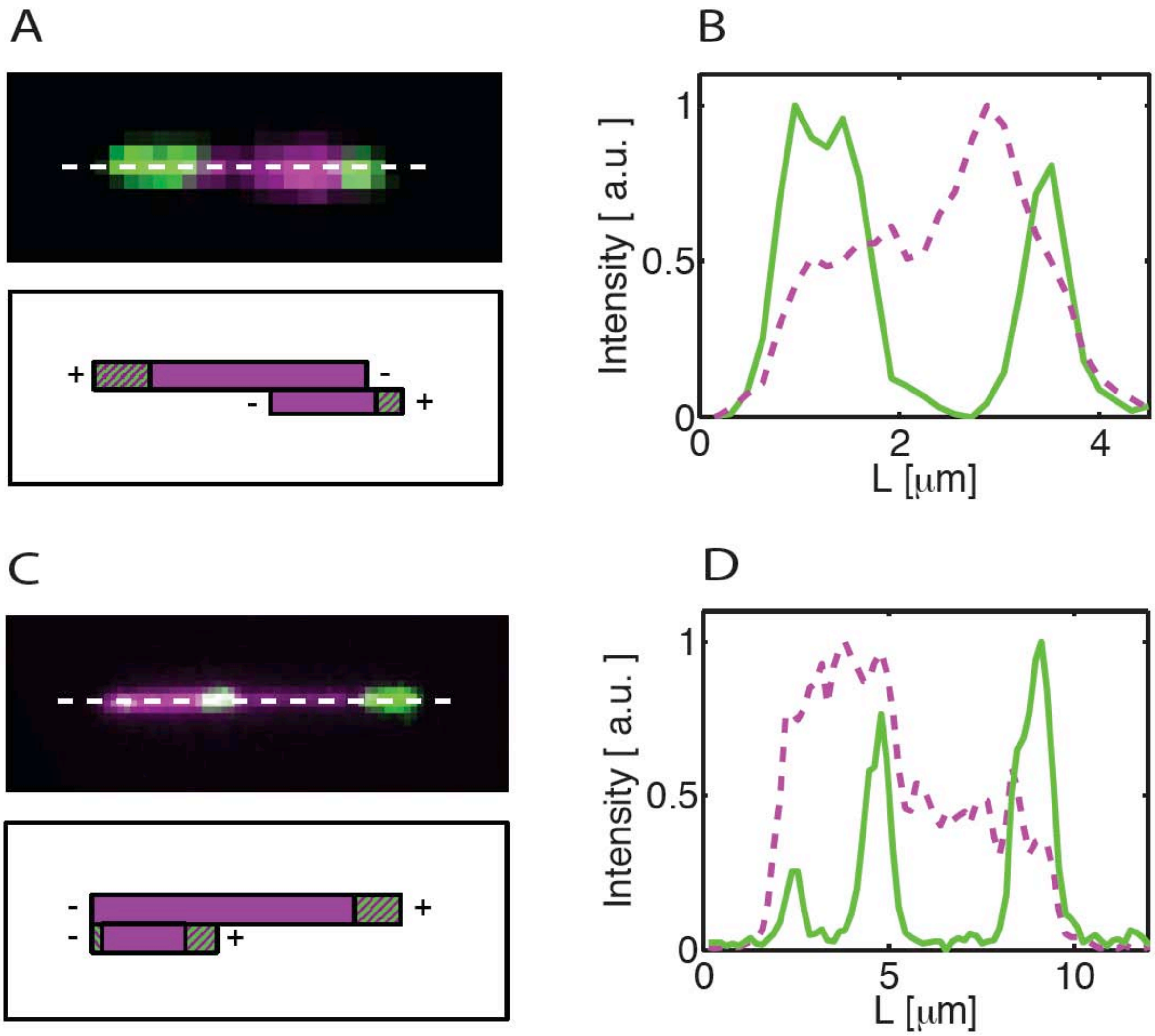

Figure 29. Polarity marking reveals doublet orientation. A and C Top: Fluorescence image of an antiparallel (A) and a parallel (C) doublet, respectively. The seeds are labeled in purple, the (+) ends in purple/green. Bottom: The scheme depicts the orientation of the microtubules forming the doublet. **B and D** Normalized intensity profile (along the dotted line depicted in A and C) of the two channels confirms the orientation of the doublet.

The doublets are formed by crosslinking stabilized polarity marked microtubules via anti-tubulin antibodies. The seeds of the microtubules are labeled with TAMRA (red), while the (+) end is labeled with Alexa-488 (green) and TAMRA (red). Due to the polarity marking and the fluorescence intensity it is possible to distinguish parallel and antiparallel doublets as shown in Figure 29. The polarity marking of 6 typical experiments was evaluated. At least 50% of all microtubules were marked by green extensions, 101 microtubules were marked correctly and only 5 false positives occurred. 27 microtubules had green extensions at the (+) and (-) end.

The gliding motility was recorded with fluorescence microscopes and evaluated via kymographs. The velocity of the doublets was evaluated in dependence of the relative length ratio of the two microtubules forming the doublet $\Delta L = \frac{L_1 - L_2}{L_1 + L_2}$, which is proportional to the relative number of antagonizing motors.

5.2 Experimental results of the doublet assay

5.2.1 Kinesin-1 driven doublets move in discrete velocity regimes

Here data from 16 different experiments is presented, in which doublets were gliding at saturating 1 mM ATP on a high density of kinesin-1 motors. 39 events of antiparallel doublets were selected for further evaluation based on the quality of the raw data. For evaluating these events the velocity of the antiparallel doublets is normalized to the velocity of single freely gliding microtubules, v_0. The average value of v_0 for all experiments, $v_0 = (574 \pm 12)$ nm/s (mean ± SEM), is calculated from the average velocities of freely gliding microtubules in individual experiments. For calculating v_0 for each and every event typically 6 microtubules from the same field of view as the doublet - or at least in the same flow cell - were considered. As a control for the gliding velocity I used parallel doublets with velocity v_p; their normalized velocity was $v_p/v_0 = 0.89 \pm 0.04$ (mean ± SEM, 5 events from 3 experiments). Antiparallel doublets did not move (11 events), moved extremely slowly with $0 < v_0 < 0.2$ (13 events) or fast with $v/v_0 > 0.8$ (13 events). Only 2 antiparallel doublets moved with $0.6 < v/v_0 < 0.8$ and no antiparallel doublet was found in the range of $0.2 < v/v_0 < 0.6$. For each type of movement, fast and slow, an example event is shown in Figure 30. 8 of the antiparallel doublets in the slow regime with $v/v_0 < 0.2$ tore apart, which is, of course, the best control to verify the antiparallel nature of the doublets. Only slow antiparallel doublets tore apart, because they are subjected to much higher loads than fast antiparallel doublets. In the case of fast motility the load the motors exerted was much lower (see chapter 5.4). All antiparallel doublets showed regular movement, typically over minutes, so that the velocity of the doublet could be defined clearly. It could also be ruled out, that the regime of fast movement stemmed from the motility of a single microtubule, which carried the second microtubule, because it is known, that kinesin-1 rotates microtubules with a periodicity of 7.9 µm at saturating ATP [Nitzsche et al, 2008].

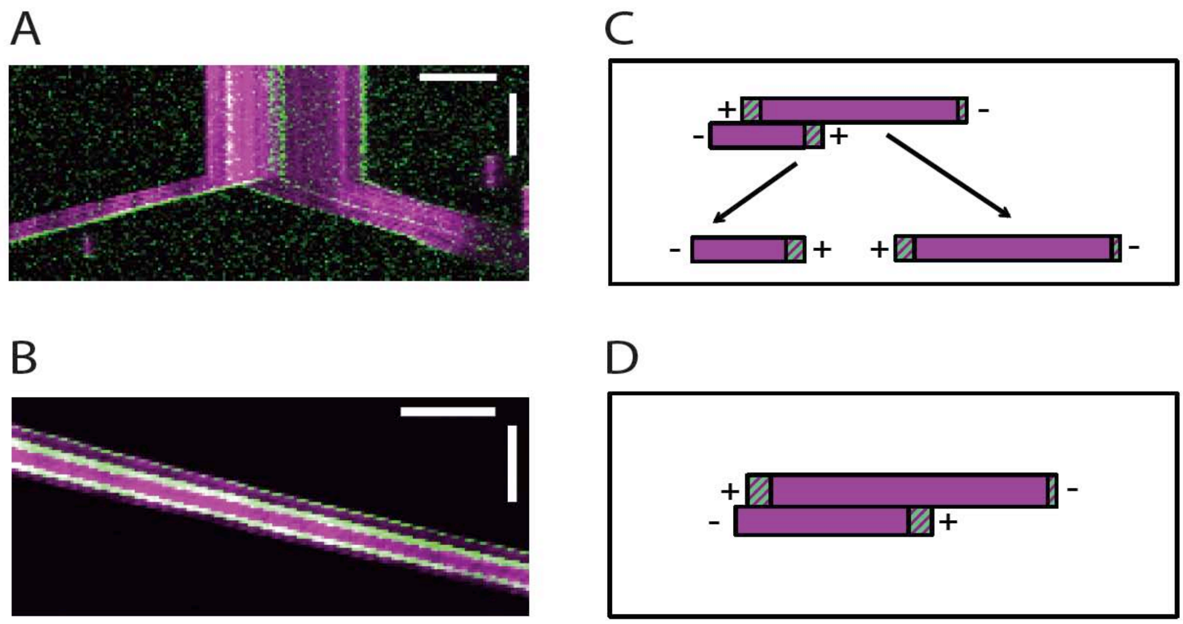

Figure 30. Doublets exhibit either fast or slow movement. A Kymograph of a very slowly moving antiparallel doublet tearing apart. Horizontal scale bar: 5 µm; vertical scale bar: 30 seconds. **C** Schematic of the doublet shown in A. The gliding orientation of the single microtubules confirms that the doublet is antiparallel. **B** Kymograph of a fast moving antiparallel doublet. Horizontal scale bar: 5 µm; vertical scale bar: 30 s. **D** Schematic of the doublet shown in B. In both kymographs, A and B, time is progressing from top to bottom. The doublets glide at 1 mM ATP on kinsin-1 motors.

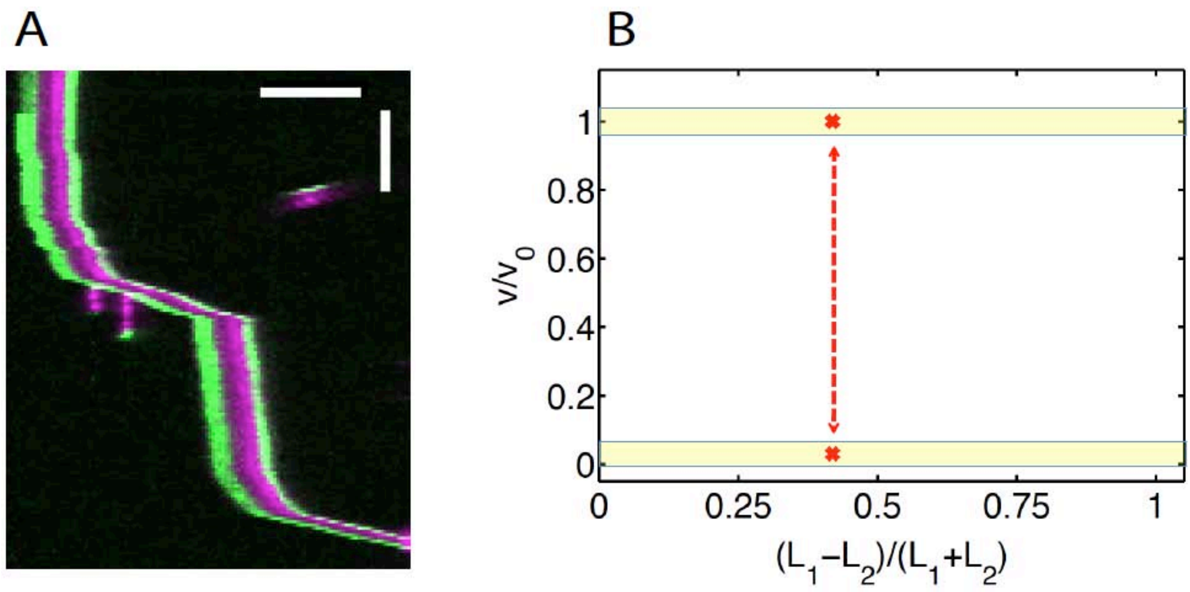

Figure 31. Doublets are able to switch between fast and slow motility. A Kymograph of an antiparallel doublet switching between fast and slow movement. Horizontal scale bar: 5 µm; vertical scale bar: 30 s. The doublet glides at 1 mM ATP on kinsin-1 motors. **B** Quantitative evaluation of the event depicted in A reveals a bistability. The well-separated regions of fast and slow motility are indicated by the yellow shaded bands.

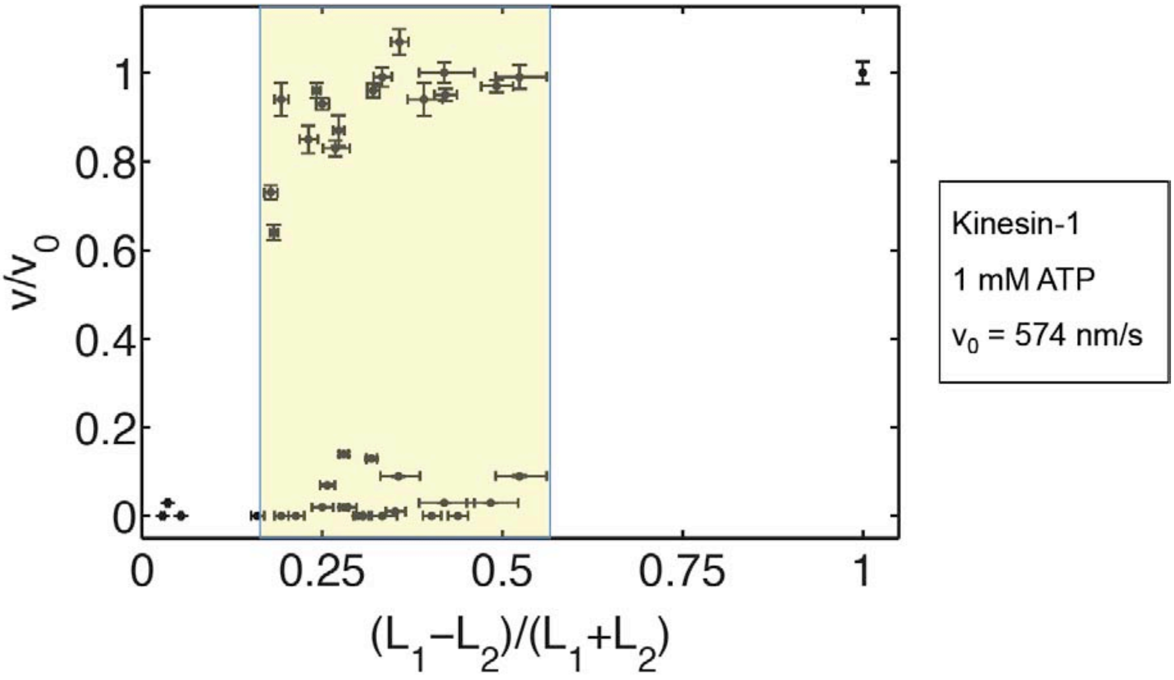

Figure 32. Antagonizing kinesin-1 motors exhibit bistability. The velocity v of the antiparallel doublets is normalized to the velocity v_0 of freely gliding microtubules and plotted against the normalized length ratio of the doublet, where L_1 and L_2 are the lengths of the two doublets (v_0 = (574 ± 12) nm/s, mean ± SEM). Here the run length of the kinesin-1 motors is about 2 µm, while it was more than 50 µm in similar experiments [Leduc et al, 2010]. The antiparallel doublets always moved with positive velocities, meaning, that the motors on the longer microtubule L_1 won the tug-of-war. Regions of slow and fast movement are clearly separated and both states of motility exist for the same length ratio, thus the system exhibits a bistability. The length errors are the measurement uncertainty; the velocity errors arise from the SEM of v_0 (, which dominates over the measurement uncertainty for the velocity of an individual doublet). The error of v_0 is determined by analyzing the velocity of typically 6 single microtubules gliding either in the same field of view as the actual doublet event, or at least in the same flow cell.

A single change from fast to slow and from slow to fast motility was each observed once. Repeated switching from slow to fast and back to slow etc. movement was observed in only 1 event, see Figure 31. This example shows nicely, that the fast and slow branch are clearly separated. It indicates, furthermore, that both velocity states, fast and slow, can be achieved with the same relative number of antagonizing motors. This idea is verified by plotting all events in one diagram, see Figure 32. Thus the system exhibits a bistability. The necessary prerequisites for achieving such a bistability are analyzed in chapter 5.4.

Furthermore, the velocity in the slow branch tends to increase with increasing length ratio, while the velocity in the fast branch tends to decrease with decreasing length ratio. The fact, that no events beyond a length ratio of 0.55 were observed, can be easily explained: The average length L_1 was 7.3 µm; at a length ratio of 0.55 L_2 was, therewith, on average 2.1 µm. It is very hard to determine the polarity and length of microtubules, which are only 2.1 µm long or even much shorter.

5.2.2 Velocity affects the shape of the bistability curve

A theoretical description of the doublet assay (see chapter 5.4) and previous experimental work [Leduc et al, 2010] indicate, that the shape of the bistability curve of antagonizing kinesin-1 motors changes with the velocity v_0 of freely gliding microtubules. Thus I tested the hypothesis that the width of the overlap zone is reduced at lower velocity. I used a lower ATP concentration to achieve a reduced velocity; 7.5 µM ATP yielded a value of $v_0 = (92 \pm 5)$ nm/s (mean ± SEM).

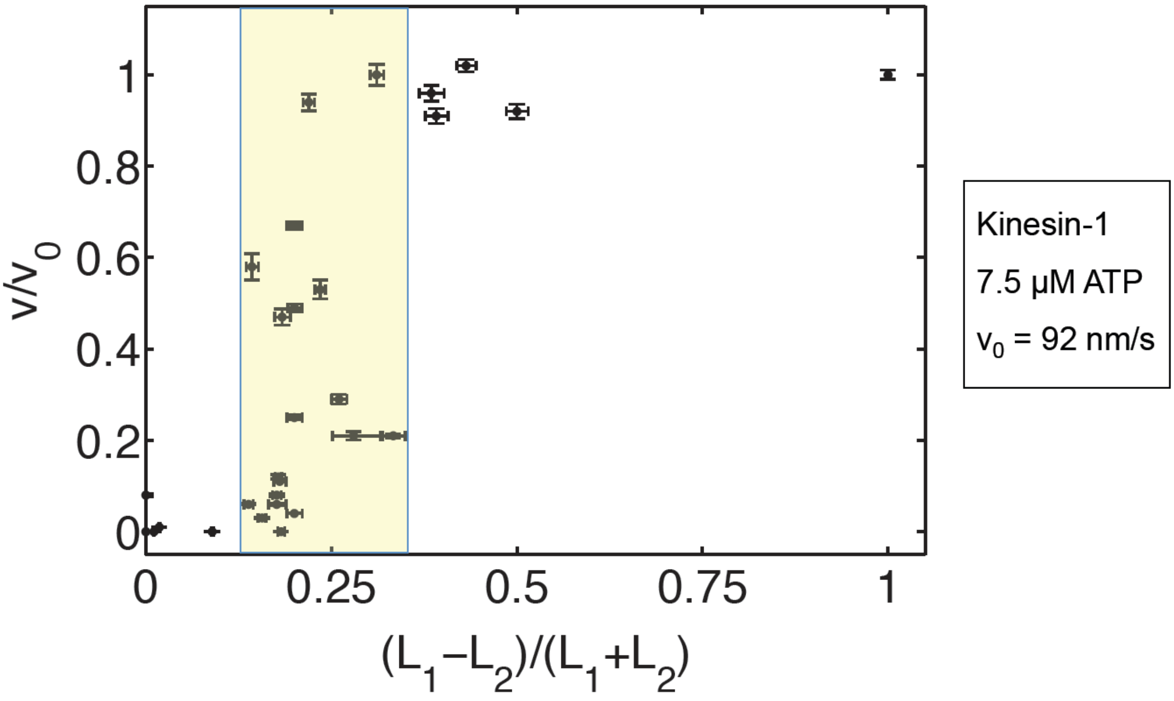

Figure 33. Antagonizing kinesin-1 motors exhibit a smaller region of bistability at low velocity. The width of the bistable region at low velocity with $v_0 = (92 \pm 5)$ nm/s (mean ± SEM) is decreased and shifted towards smaller relative lengths compared to the high velocity case at saturating ATP. The error is calculated as for Figure 32.

The experiment results in Figure 33 show, that the width of the overlap zone reduced indeed, in particular the slow branch ends at much lower values of the normalized doublet length. Out of the 29 events from 17 experiments, 4 tore apart

(v/v_0 was in the range of 0 - 0.21), only one doublet changed its velocity between $v/v_0 = 0.04$ and $v/v_0 = 0.25$. The control velocity of parallel doublets was $v_p/v_0 = 0.94 \pm 0.03$ (mean ± SEM, 19 events from 11 experiments).

5.2.3 Dynein's processivity allows bistability at low velocity

Several studies indicate that dynein behaves, in particular in multi-motor assays, markedly different from kinesin-1, although step size and stall force are (according to most publications) very similar. The processivity of dynein is slightly higher but still comparable to kinesin-1. Thus I want to compare the multi-motor properties of antagonizing dynein motors directly with the ones of antagonizing kinesin-1 motors and explain potential differences quantitatively. In the end it should be possible to explain the different behavior according to one of the parameters, which are included in the physical model, such as attachment or detachment rate.

I use a "minimal" dynein construct (GST-Dyn1_{331kD}) consisting of two dimerized heavy chains from budding yeast for several reasons. First of all it is very well characterized and a straightforward purification protocol is established [Gennerich et al, 2007; Reck-Peterson et al, 2006]. Furthermore it is evolutionary, but also according to its velocity, closer to the dynein from fission yeast than mammalian dynein. And one of the motivations for establishing this assay is also to learn more about the underlying principles of dynein driven nuclear oscillations in fission yeast.

Considering the result for kinesin-1 at 7.5 µm ATP with $v_0 = 92$ nm/s and the low velocity of the dynein construct (at saturating 1 mM ATP) of $v_0 = (64 \pm 2)$ nm/s (mean ± SEM), one could expect, that dynein driven doublets do not exhibit a bistability. On the contrary I observed clearly separated regions of fast and slow doublet gliding velocity for the same normalized length differences.

23 events were evaluated in total. Either the doublet did not move (7 events), moved extremely slowly with $0 < v/v_0 < 0.1$ (5 events) or fast with $v/v_0 > 0.8$ (11 events). 6 of the events in the slow regime with $v/v_0 < 0.1$ tore apart. Again, only slow - but no fast - events tore apart. The experiment results in Figure 34 show, that the region of bistability spans a similar region of normalized length differences as for the kinesin-1 driven doublets at 1 mM ATP. The separation of the two branches, is however, even more pronounced than for kinesin-1 driven doublets,

the slow branch extends only up to $v/v_0 \approx 0.1$ and no intermediate values with $0.1 < v/v_0 < 0.8$ were observed.

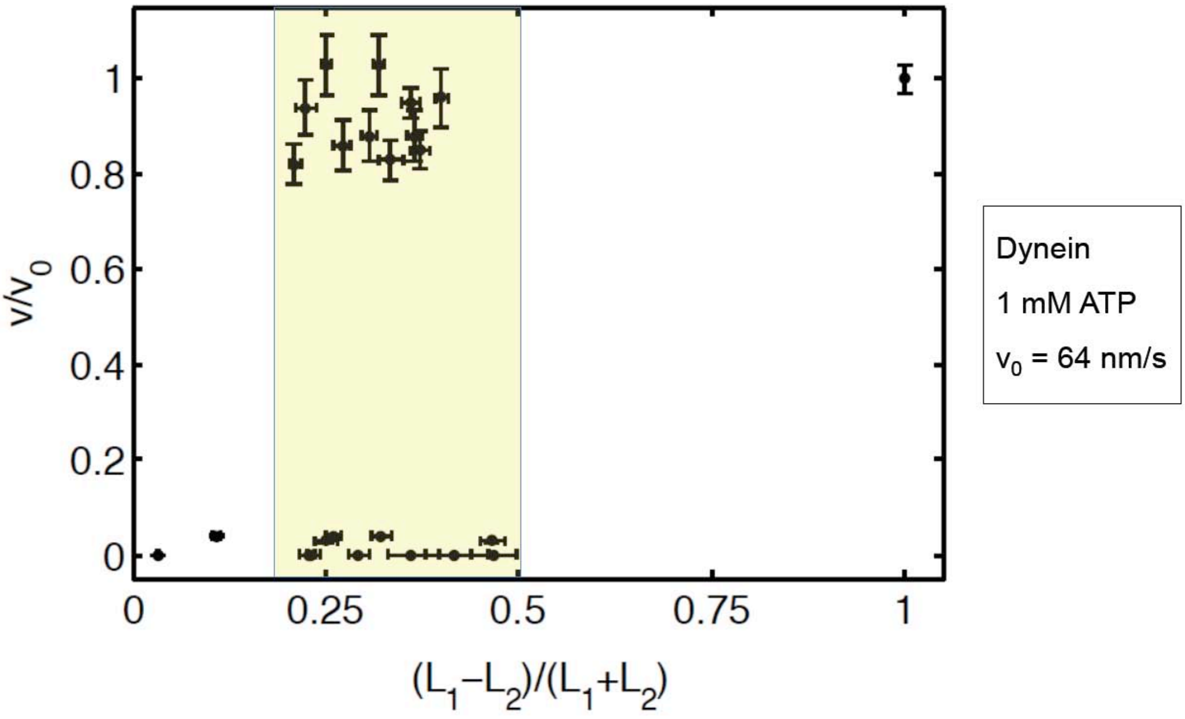

Figure 34. Antagonizing dyneins also exhibit a bistability. The width of the bistability region for doublets gliding on dynein with v_0 = (64 ± 2) nm/s (mean ± SEM) is comparable to doublets gliding on kinesin-1. The region of slow and fast movement are clearly separated. The error is calculated as for Figure 32.

5.2.4 Ncd does not exhibit a bistability curve

In order to understand the differences between the collective behavior of processive and non-processive motors quantitatively, I applied the doublet assay to the non-processive motor Ncd. Here, I used a construct with a GST tag on the (truncated) tail region, thus the second, non-motor microtubule binding domain was not present. The motor is immobilized via a GST-antibody, so that unspecific binding was prevented together with surface blocking.

The result is shown in Figure 35. 27 events from 11 experiments were evaluated with v_0 = (205 ± 6) nm/s (mean ± SEM). 12 antiparallel doublets did not move; 2 antiparallel doublets tore apart, one of them did not move before, the other one moved slowly with $v/v_0 \approx 0.1$. Only 4 events lie significantly above the line defined by $v/v_0 = \Delta L$. Thus it seems as if Ncd driven doublets do not exhibit a bistablity, although it cannot be excluded, that the 4 events classified as outliers are (at least partially) part of a fast branch.

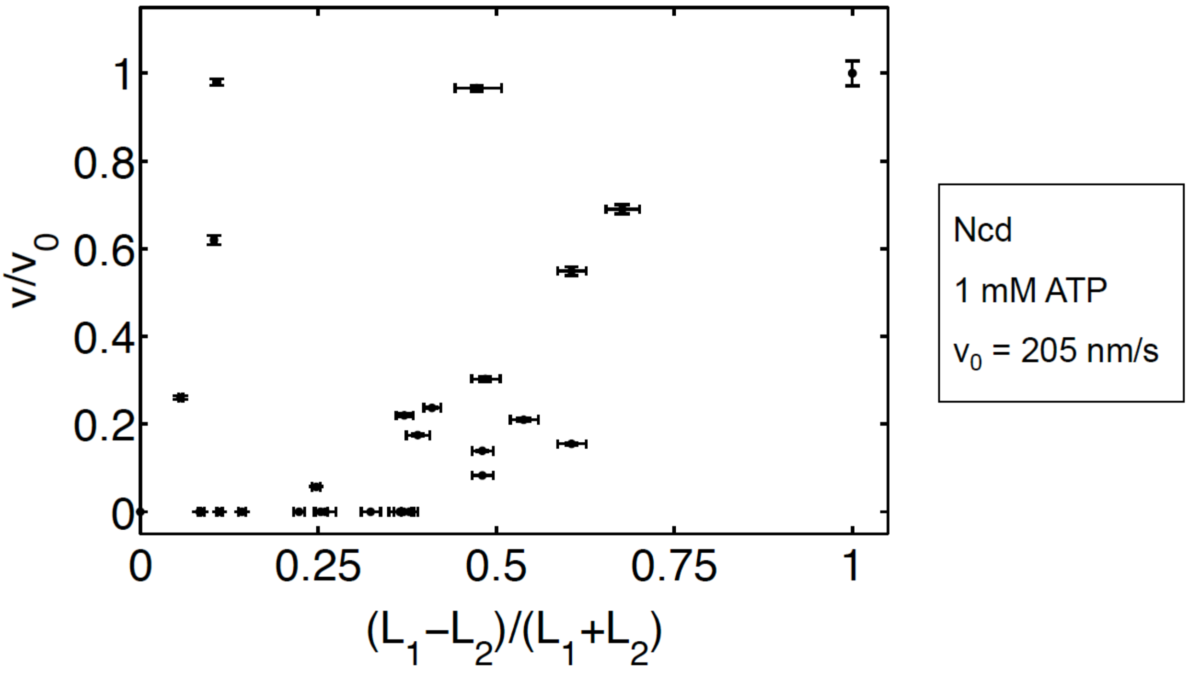

Figure 35. Antagonizing Ncd motors do not exhibit bistability. Only 4 events lie significantly above the line defined by $v/v_0 = \Delta L$. The average velocity of freely gliding microtubules is $v_0 = (205 \pm 6)$ nm/s (mean ± SEM). The error is calculated as for Figure 32.

5.3 Theoretical results of the doublets assay

First I present expressions for the force acting on a microtubule in the doublet assay and the corresponding force-velocity relationships. In chapter 5.3.2 I follow essentially the work by Leduc et al. [Leduc et al, 2010]. In chapter 5.3.3 and 5.3.4 I rely mainly on a recent article by Guerin et al. [Guerin et al, 2011] and unpublished work by my theoretical collaborator Rui Ma (Institute for advanced study, Tsinghua University, Beijing, China; visiting scientist at the Max-Planck-Institute of the Physics of Complex Systems).

5.3.1 General concepts

A scheme of the experimental system is depicted in Figure 36 and it is assumed to work in one dimension. The left microtubule has the length L_2, the right microtubule the length L_1, and the number of motors associated with the two microtubules is proportional to their lengths (and the motor density n_0). The two microtubules are rigidly coupled to each other and form a doublet. The whole doublet moves with a positive velocity v, if it moves to the right direction, while individual motors step towards the (+) end (marked by the purple/green region in Figure 36) with the force-velocity relationship $v_m(f)$. The basic equation for describing this mechanical system is the force balance with the force $\boldsymbol{F}$ and the coefficient denoting viscous friction ξ:

$$F = \xi\, v = 0 \qquad \textit{Eq. 15}$$

The friction coefficient of the microtubule is negligible and therefore set to 0. Thus the load force of the motors on one microtubule equals the load force of the motors on the other microtubule. In the following section the detailed expression for the force balance is derived.

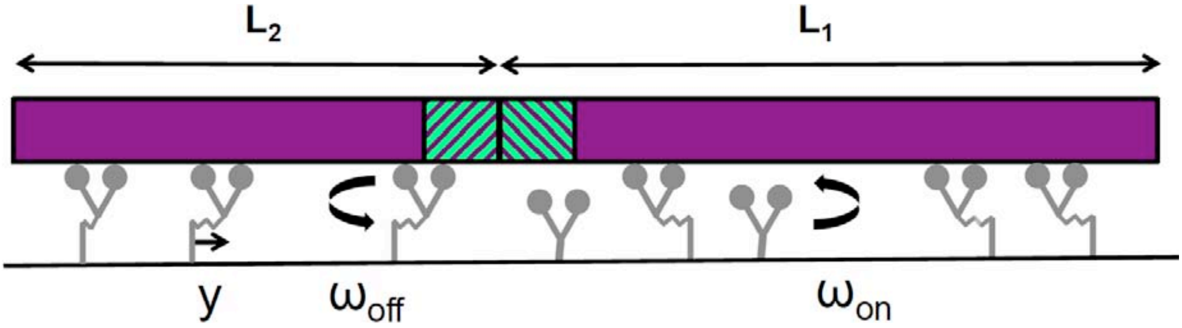

Figure 36. Single-motor properties for a multi-motor theory. The (+) ends of the microtubules are marked by the purple/green regions, the motors are sketched in grey. Important motor properties for the modeling of collective dynamics of antagonizing motors are the force-dependent detachment ω_{off}, the force-independent attachment rate ω_{on} and the linker extension y. The linker extension defines the load of a single motor via Hooke's law.

There are three basic assumptions concerning the attachment and detachment of the motor proteins from the microtubule. First, the rate describing the detachment of the motor protein from the microtubule, ω_{off}, depends exponentially on a load force f. Second, this load force f is given by the elastic properties of the motor protein itself; the protein is modeled as a linear (or Hookean) spring with stiffness k and extension y. The extended region of the protein is from now on referred to as linker.

Thus the load force exerted by an individual motor protein on the right microtubule is given by $f = -k\,y$. The first two assumptions lead to the following expression:

$$\omega_{off}(y) = \omega_0\, e^{(k|y|/f_c)} \qquad \textit{Eq. 16}$$

where ω_0 is the detachment rate in the absence of force and f_c is a characteristic force. The third assumption is, that the attachment rate ω_{on}, with which the motor protein binds to the microtubule, is constant.

5.3.2 Theory for processive motors

The extension of the linker arises from the relative movement of the doublet with respect to the fixed position of the motor protein. The linker extension changes over time for the motors on the right microtubule according to:

$$dy/dt = v - v_m(f) \qquad \textit{Eq. 17}$$

where $v_m(f)$ is the force-velocity relationship of a single motor protein. The exact shape of $v_m(f)$ influences the dynamic of antagonizing motors strongly, see chapter 5.3.5.

In the steady state the velocity of the doublet and the number of attached and detached motors is constant, thus $\partial_t p_a = \partial_t p_d = 0$ with the probability density function of the motor to be in a attached state, $p_a(y,t)$, or to be in a detached state, $p_d(y,t)$, respectively. In the steady state the average force exerted by a motor on the right microtubule $\overline{f}(v)$ is given by

$$\overline{f}(v) = -k \int_{-\infty}^{\infty} y\, p_a dy \qquad \textit{Eq. 18}$$

In order to calculate the average force per motor, an expression for p_a (and thus for p_d as well) is needed. The relationship between p_a and p_d is given by:

$$\partial_t p_a = -\partial_y \left[\frac{dy}{dt} p_a\right] - \omega_{off}\, p_a + \omega_{on}\, p_d \qquad \textit{Eq. 19}$$

If the linker relaxation after detachment is fast compared to the attachment rate, then the probability density function for a motor to be in a detached state, can be written as:

$$p_d(y,t) = Q_d(t)\, A\, e^{(-ky^2)/(2k_BT)} \qquad \textit{Eq. 20}$$

where $Q_d(t) = \int_{-\infty}^{\infty} p_d(y,t)dy$ is the probability for a motor to be detached and $A = [k/(2\pi k_B T)]^{1/2}$ a normalization constant. Now it is possible to calculate the distribution of attached and detached motors and therewith the average force per motor numerically (for further details see supplement of [Leduc et al, 2010]).

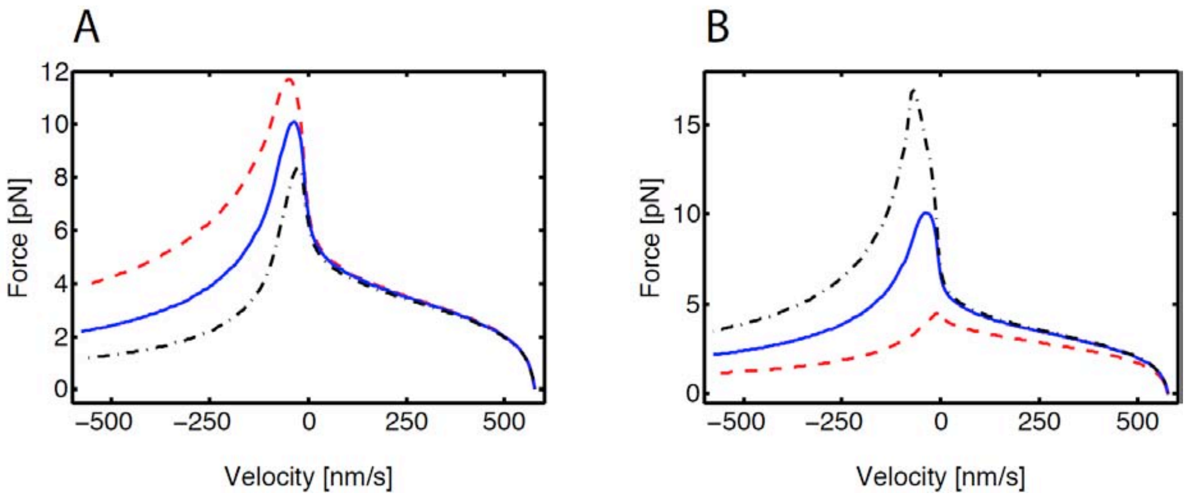

Figure 37. Multi-motor force-velocity relationships for processive motors. A $\overline{f}(v)$ for ω_0 = 0.05/s, f_c = 4 pN, k = 2 pN/nm and ω_{on} = 10/s (--), 5/s (-), 2.5/s (.-). Higher values of ω_{on} lead to a higher ratio of attached motors, Q_a, and therefore to higher restoring forces at a given backward velocity. **B** $\overline{f}(v)$ for ω_{on} = 5/s, f_c = 4 pN, k = 2 pN/nm and ω_0 = 0.5/s (--), 0.05/s (-), 0.005/s (.-). Increasing values of ω_0 lead to a lower ratio of attached motors, Q_a, and therefore to lower restoring forces, in particular close to very small velocity values. Changing ω_{off} via k (or f_c) has similar effects on negative velocities, but leaves the maximal restoring force nearly unaffected.

There are multiple parameters, which contribute to calculating $\overline{f}(v)$: First of all the force-velocity relationship of the single motor, $v_m(f)$, which itself contains several parameters. Here I rely on a model for the force-velocity relationship, which includes the step size of the motor and two forward and two backward rates [Kolomeisky & Fisher, 2007]. The parameters for $v_m(f)$ were chosen to match the experimental data. $v_m(f)$ and the associated parameters are presented in chapter 3.5.3. Other parameters for $\overline{f}(v)$ are the stiffness k, the attachment rate ω_{on}, the detachment rate ω_0 in the absence of force and the characteristic force f_c, which describes the force dependency of the detachment rate ω_{off} (together with the stiffness k). Figure 37 shows the effect of the detachment rate ω_{off} on $\overline{f}(v)$ by varying ω_0, which is directly related to the run length measured in chapter 3, R_l, via $\omega_0 = \frac{v}{R_l}$ and the effect of ω_{on}.

5.3.3 Theory for non-processive motors

The first difference between processive and non-processive motors occurs upon defining the elongation of the motor linker with length y. For a non-processive motors attached to the right microtubule it holds

$$dy/dt = v \qquad \textit{Eq. 21}$$

because a non-processive motor does not walk with a well-defined velocity v_m, but makes only a single step before detachment. The classical crossbridge model assumes, furthermore, that the motor makes a conformational change of length y_0 upon attaching to the microtubule. If the conformational change, or power stroke, is directed towards the (+) end of the microtubule, then the strained linker exerts a force into the opposite direction on the microtubule, which can be described by $\delta(y + y_0)$. Thus the flux of the probability density function (analogue to Eq. 19 for processive motors) turns into:

$$\partial_t p_a = -\,\partial_y[v\, p_a] - \,\omega_{off}\, p_a + \omega_{on}\, Q_d \delta(y + y_0) \qquad \textit{Eq. 22}$$

where $Q_d = 1 - \int_{-\infty}^{\infty} dy p_a$ is the fraction of motors in a detached state. Here, the probability density function of a motor to be in a detached state is defined as $p_d(y,t) = Q_d \delta(y)$. While for processive motors a Gaussian function was used to describe the distribution of the linker length for detached motors, a δ function is employed here. This approach neglects fluctuations of the linker length (and therefore noise), but allows for an analytical solution of the problem. In the steady state the average force per motor is calculated as for the processive motor, $\overline{f}(v) = -k \int_{-\infty}^{\infty} y\, p_a dy$.

It is simpler to solve Eq. 22 in a different parameter space. Instead of denoting the linker elongation by the spatial component y it is convenient to denote it by $v\,\tau$, where τ is the attachment time of the motor protein. The transformation leads to the following expression for force-velocity relationship of a motor on the right microtubule:

$$\bar{f}(v) = -\frac{\omega_{on}\,k\,\int_0^\infty d\tau\,(v\tau - y_0)e^{-I_1}}{\omega_{on}\int_0^\infty d\tau\,e^{-I_1} + 1} \qquad \textit{Eq. 23}$$

with $I_1 = \int_0^\tau d\tau'\omega_{off}\,(v\tau' - y_0)$. Once the necessary parameters are known, $\bar{f}(v)$ can be calculated directly.

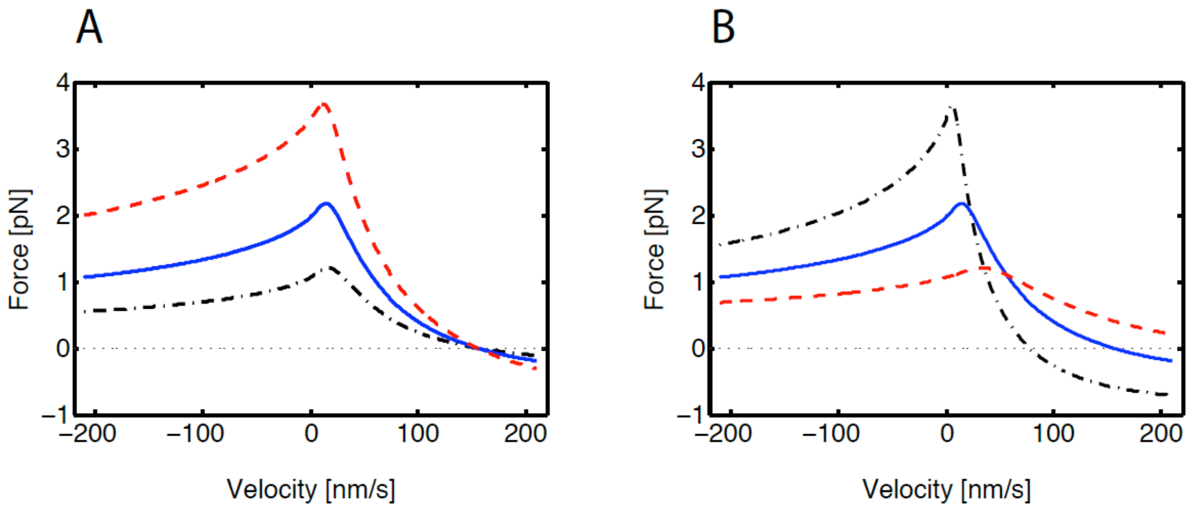

Figure 38. Multi-motor force-velocity relationships for non-processive motors. A $\bar{f}(v)$ for ω_0 = 1/s, f_c = 4 pN, k = 1.5 pN/nm and ω_{on} = 10/s (--), 5/s (-), 2.5/s (.-). The effect of ω_{on} is comparable to processive motors. **B** $\bar{f}(v)$ for ω_{on} = 5/s, f_c = 4 pN, k = 1.5 pN/nm and ω_{on} = 2/s (--), 1/s (-), 0.5/s (.-). The effect of ω_0 is comparable to processive motors for negative velocities and changes, furthermore, the velocity in the absence of force. Lower detachment rates correspond to more bound motors, which can act as springs and slow down the microtubule. Changing ω_{off} via k (or f_c) has similar effects on $\bar{f}(v)$.

In a next step, the approach for non-processicve motors is generalized by introducing a third step before the power stroke. The rate, with which the motor performs the power stroke after attachment is denoted by ω_p. The probability density function must be subdivided in two populations, where p_a^1 refers to those motors, which have not performed the powerstroke yet, and p_a^2 to those motors, which have already performed the powerstroke. It follows:

$$\partial_t p_a^1 = -\,\partial_y[v\,p_a^1] - \,\omega_{off}\,p_a^1 + \omega_{on}\,Q_d\delta(y) - \,\omega_p p_a^1 \qquad \text{Eq. 24}$$

$$\partial_t p_a^2 = -\,\partial_y[v\,p_a^2] - \,\omega_{off}\,p_a^2 + \,\omega_p p_a^1(y + y_0) \qquad \text{Eq. 25}$$

where $Q_d = 1 - \int_{-\infty}^{\infty} dy(p_a^1 + p_a^2)$ is the fraction of motors in the unbound state. It should be noticed, that the term $\omega_{off}\,p_a^1$ includes the detachment of those motors, which have not performed the power stroke yet. This is different than in the original theory by Guerin et al. [Guerin et al, 2011]. Analogue to the two-step model $\overline{f}(v)$ is given by

$$\overline{f}(v) = -k\int_{-\infty}^{\infty} y\,(p_a^1 + p_a^2)dy \qquad \text{Eq. 26}$$

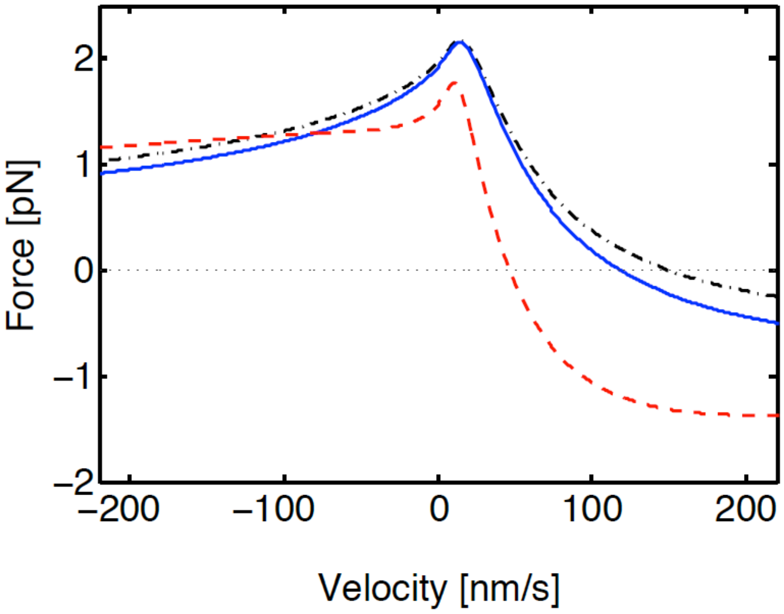

Figure 39. Multi-motor force-velocity relationship for non-processive motors in the three-state model. $\overline{f}(v)$ for ω_0 = 1/s, f_c = 4 pN, k = 1.5 pN/nm, ω_0 = 5/s and ω_p = 20/s (--), 200/s (-), 2000/s (.-). Low values of ω_p lead to binding events without power stroke and hence decrease the velocity in the absence of force.

5.3.4 The emergence of bistability

The force balance (Eq. 15) describing the antagonizing activity of motors in the doublet experiment can generally be expresses as:

$$L_1 \bar{f}(v)\ n_0 - L_2 \bar{f}(-v)\ n_0 = 0 \qquad \textit{Eq. 27}$$

The motor density n_0, however, cancels out and is not relevant for interpreting the data, as long as it is high enough to justify the mean-field approach. Without loss of generality it can be assumed, that $L_1 > L_2$, and Eq. 27 can be rewritten in the following way:

$$\Delta L = \frac{L_1 - L_2}{L_1 + L_2} = \frac{\bar{f}(-v) - \bar{f}(v)}{\bar{f}(-v) + \bar{f}(v)} \qquad \textit{Eq. 28}$$

Substituting $\bar{f}$ with the expressions mentioned above (or at least the numerical values) gives the velocity of the doublet in dependence of the relative length ΔL.

In order to understand the occurrence of the bistability it is necessary to describe the regimes of slow and fast movement as distinct phenomena. For the regime of slow movement, where $v = 0$, the average force per motor can be expressed by a Taylor expansion: $\lim_{v \to 0} \bar{f}(v) = \bar{f}(v)|_{v=0} + \zeta v$ with the effective friction $\zeta = \left.\frac{d\bar{f}(v)}{dv}\right|_{v=0}$. Thus it follows with Eq. 28:

$$\Delta L = -\frac{\zeta v}{\bar{f}(v)|_{v=0}} \qquad \textit{Eq. 29}$$

ζ is the effective protein friction between the motors and the microtubule. Under which conditions can such slow movement occur? Since $L_1 > L_2$ it follows $\bar{f}(v) < \bar{f}(-v)$, and thus

$$\zeta = \left.\frac{d\bar{f}(v)}{dv}\right|_{v=0} = \lim_{\Delta \to 0} \frac{f(\Delta \mathrm{v}) - f(-\Delta \mathrm{v})}{2\Delta \mathrm{v}} < 0 \qquad \textit{Eq. 30}$$

Vice versa solution with $\zeta > 0$ are not stable. In order to define the sign of ζ a general expression for $\bar{f}(v)$ in the vicinity of 0 has to be found. The average force per motor acting on the right microtubule can be estimated in a simple manner:

$$\bar{f}(v) = -k \int_{-\infty}^{\infty} y \, \frac{p_a}{Q_a} Q_a dy = -k \, \bar{y} \, Q_a \qquad \textit{Eq. 31}$$

where $\bar{y}$ is the average elongation of the linkers, and $Q_a \cong \int_{-\infty}^{\infty} p_a \, dy = \frac{\omega_{on}}{\omega_{on} + \omega_{off}}$ the fraction of attached motors. In the vicinity of $v = 0$ Taylor expansion yields

$$\lim_{v \to 0} \bar{f}(v) = -k \frac{\omega_{on}}{\omega_{on} + \overline{\omega_{off}(0)} + \overline{\omega_{off}(0)}' v} (\bar{y}(0) + \frac{v}{\overline{\omega_{off}(0)}}) \qquad \textit{Eq. 32}$$

, where $\overline{\omega_{off}(v)} = \int_{-\infty}^{\infty} p_a(y; v) \; \omega_{off}(y; v) dy$ is the average detachment rate and $\overline{\omega_{off}}'(v) = \frac{d \, \omega_{off}(v)}{dv}$. Further derivation yields

$$\zeta = -k \frac{\omega_{on}}{[\omega_{on} + \overline{\omega_{off}(0)}]} (\frac{1}{\overline{\omega_{off}(0)}} - \frac{\overline{\omega_{off}(0)}' \, \bar{y}(0)}{\omega_{on} + \overline{\omega_{off}(0)}}) \qquad \textit{Eq. 33}$$

The absolute value of the first, negative term grows with a decreasing detachment rate and can be interpreted as negative protein friction. It arises from energy dissipation due to relaxing linkers upon detachment. At a lower detachment rate, the linkers stretch further and store - but eventually also release - more energy. The second term exists only, if $\overline{\omega_{off}(0)}' \neq 0$, i.e. if there is force dependent detachment. Thus strongly force dependent detachment can prevent the existence of the slow branch.

In the next paragraph the necessary prerequisites for the existence of a fast branch are discussed. In order to analyze the doublet behavior at high velocities, a general valid expression of ΔL must be found for this regime. Since $\bar{f}(v_{max}) = 0$, a Taylor expansion can be applied to Eq. 28:

$$\Delta L = \frac{\overline{f}(-v_{max}) - \eta(v - v_{max})}{\overline{f}(-v_{max}) + \eta(v - v_{max})} \qquad \textit{Eq. 34}$$

, where $\eta = \left.\frac{d\overline{f}(v)}{dv}\right|_{v=v_{max}} < 0$, because $L_1 > L_2$. For a bistability the fast branch should exhibit a shallow slope, which means, that $\frac{\partial \Delta L}{\partial v}$ should have high values. Differentiation of Eq. 34 yields:

$$\left.\frac{\partial \Delta L}{\partial v}\right|_{v=v_{max}} = -\frac{2\eta}{\overline{f}(-v_{max})} > 0 \qquad \textit{Eq. 35}$$

because $\overline{f}(-v_{max}) > 0$. A bistibality becomes therefore more likely for large η and small $\overline{f}(-v_{max})$. The values for η and $\overline{f}(-v_{max})$ are, of course, strongly model dependent and both depend on the attachment and detachment rates. In order to understand the effects of these parameters better, η can be rewritten. At $v \rightarrow v_{max}$ one can estimate $\overline{y} = (v - v_m)\frac{1}{\omega_{off}(0)}$ and it follows

$$\eta = \left.\frac{d\overline{f}(v)}{dv}\right|_{v\rightarrow v_{max}} = -k\, Q_a \frac{1}{\omega_{off}(0)} \qquad \textit{Eq. 36}$$

Thus η tends to be large at a low detachment rate at zero linker elongation. The average force per motor, $\overline{f}(-v_{max})$ correlates negatively with the force dependency of the detachment rate. This connection can be derived from Eq. 31, $\overline{f}(-v) = -k\,\overline{y}\,Q_a > 0$, because $\overline{y} < 0$ for $-v$. If the force sensitivity (due to a high k or small f_c) is high, then the ratio of attached motors, Q_a, becomes automatically smaller. A high attachment rate is also desirable for the fast branch, because Q_a increases with the attachment rate.

Thus there is a tradeoff for achieving a bistability between low detachment rates, which support the existence of a slow branch and highly variable detachment rates with a strong force-dependency, which support the existence of a fast branch.

5.3.5 Model for single-motor force-velocity relationships

The force-velocity relationship of a single processive motor, $v_m(f)$, is modeled according to [Kolomeisky & Fisher, 2007]. In this model u_j denotes forward rates and w_j denotes backward rates, while d denotes the step size of the whole motor protein, and $v_m(f)$ with n = 2 chemical states is given by:

$$v_m(f) = d(u_0 u_1 - w_0 w_1)/(u_0 + u_1 + w_0 + w_1) \qquad \textit{Eq. 37}$$

With the characteristic forces $d_\pm$ the individual transition rates are given by the following set of equations:

$$u_0\,(f) = u_0\,(0)\,e^{f\,d_+/\,(k_B\,T)} \qquad \textit{Eq. 38}$$

$$u_1\,(f) = u_1\,(0) \qquad \textit{Eq. 39}$$

$$w_0\,(f) = w_0\,(0)\,e^{-f\,d_-/\,(k_B\,T)} \qquad \textit{Eq. 40}$$

$$w_1\,(f) = w_1\,(0) \qquad \textit{Eq. 41}$$

The parameters were chosen to fit previously published data, but also to allow a satisfying description of the doublet experiments. All values are listed in Table 4.

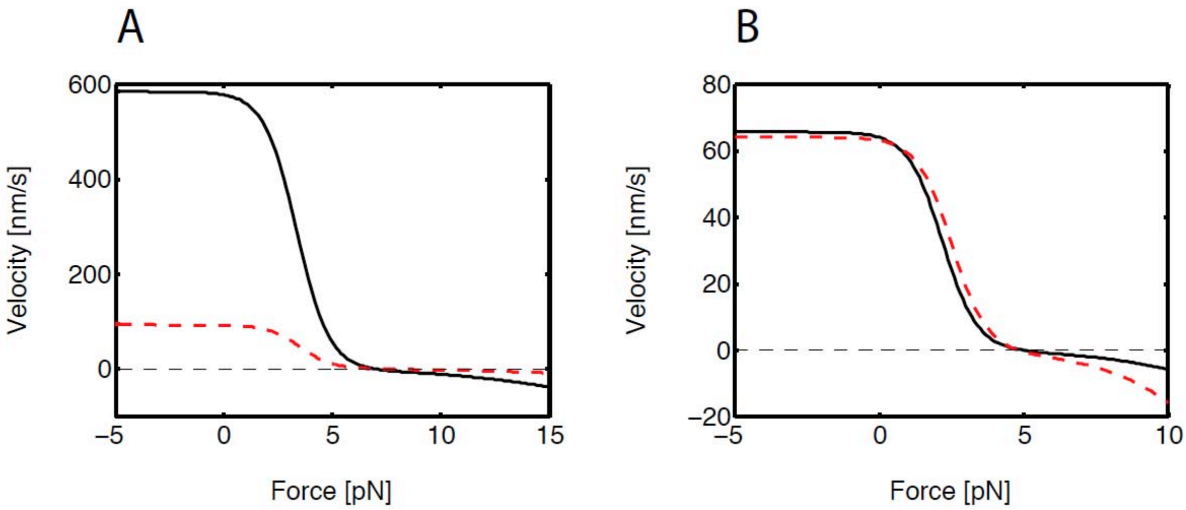

Figure 40. Single-motor force-velocity relationships. A $v_m(f)$ for kinesin-1. The solid black line corresponds to 1 mM ATP, the dashed red line to 7.5 µM ATP. They were chosen to fit the data by [Carter & Cross, 2005]. **B** $v_m(f)$ for dynein. The black curve is used to model dynein's behavior. The dashed red line is more similar to a previously published data [Gennerich et al, 2007], but does not allow to obtain a bistability, see Figure 41.

Parameter	Kinesin-1 (fast)	Kinesin-1 (slow)	Dynein 1	Dynein 2
$u_0\ (0)\ [1/s]$	7500	1500	400	1200
$u_1\ (0)\ [1/s]$	73	10.6	8.2	8
$w_0\ (0)\ [1/s]$	0.5	0.04	0.04	0.03
$w_1\ (0)\ [1/s]$	10	2	2	10
$k_B\ T\ /\ d_+\ [pN]$	0.75	0.75	0.6	0.6
$k_B\ T\ /\ d_-\ [pN]$	3	2.5	2	2
$d\ [nm]$	8	8	8	8

Table 4. Parameters for modeling single-motor force-velocity relationships.

The modeled curves for kinesin-1 are shown in Figure 40 A; two possible curves for dynein are shown in Figure 40 B. For the particular dynein construct used in this work no force-velocity curve is published yet. Nevertheless, its stall force is measured and the force-velocity curve of a very similar construct is known. This construct exhibits rather high backward velocities at loads beyond the stall force; the red dashed curve in Figure 40 B considers such high backward velocities. The force measurements were, however, carried through under different salt conditions (30 mM HEPES) [Gennerich et al, 2007] than the doublet experiments with dynein (30 mM HEPES + 50 KAcetate). Thus it seems reasonable to use a more conservative estimate of the backward velocity at high opposing loads. The force-velocity curve depicted in black in Figure 35 B allows obtaining final curves for v/v_0 vs. ΔL, which describe the experiments without assuming extreme values for attachment or detachment rates.

In Figure 41 the effect of different slopes for backward movement at high loads becomes apparent. Faster backward movement of one team of motors results in faster forward movement of the other team of motors, which is already about to win the tug-of-war. Thus the faster motors are subjected to a lower average load and detach less frequently. Such positive feedback can prevent the existence of a slow branch, as it is the case here.

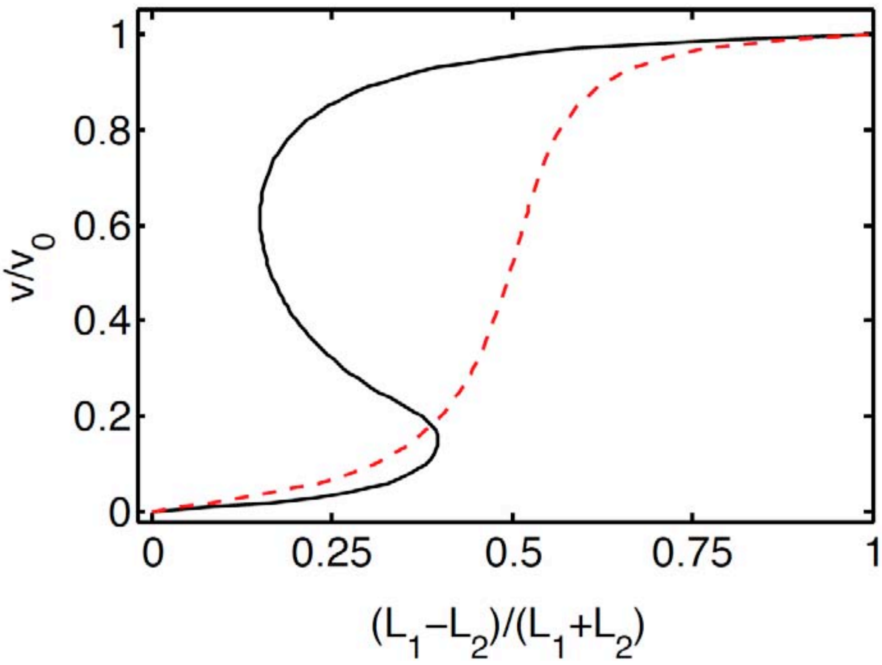

Figure 41. Single-motor force-velocity relationships influence collective effects. The black curve corresponds to the function $v_m(f)$ plotted in black in Figure 40 B and is also used in chapter 5.4 for describing the doublet experiments with dynein. The dashed red line corresponds to the function $v_m(f)$ plotted in dashed red in Figure 40 B. The following parameters are the same for both curves: $f_c = 2.5$ pN, $\omega_0 = 0.005$/s, $\omega_{on} = 1$/s, k = 2 pN/nm.

5.4 Comparison between theoretical and experiment results

In order to test the theory presented in the previous chapter, it is desirable to determine as many parameters as possible from experimental data. Generating the final plots for v/v_0 (ΔL) should require, therefore, only very few free parameters. The kinetic properties of kinesin-1 are comparatively well known. There is less, and sometimes contradictory data for dynein, and even less trustworthy measurements are published for Ncd.

For kinesin-1 the value for ω_{on} was measured to be 5/s, although in a different geometry than here [Leduc et al, 2004]. The value for ω_0 is principally known from stepping experiments. f_c was measured to be 3 pN [Schnitzer et al, 2000], while values for k are around 0.5 pN/nm [Jeney et al, 2004; Kawaguchi et al, 2003]. Previously published doublet experiments with superprocessive motors required, however, a higher value of k = 2 pN/nm to obtain a satisfactory agreement between theory and experiment. This value is also used here.

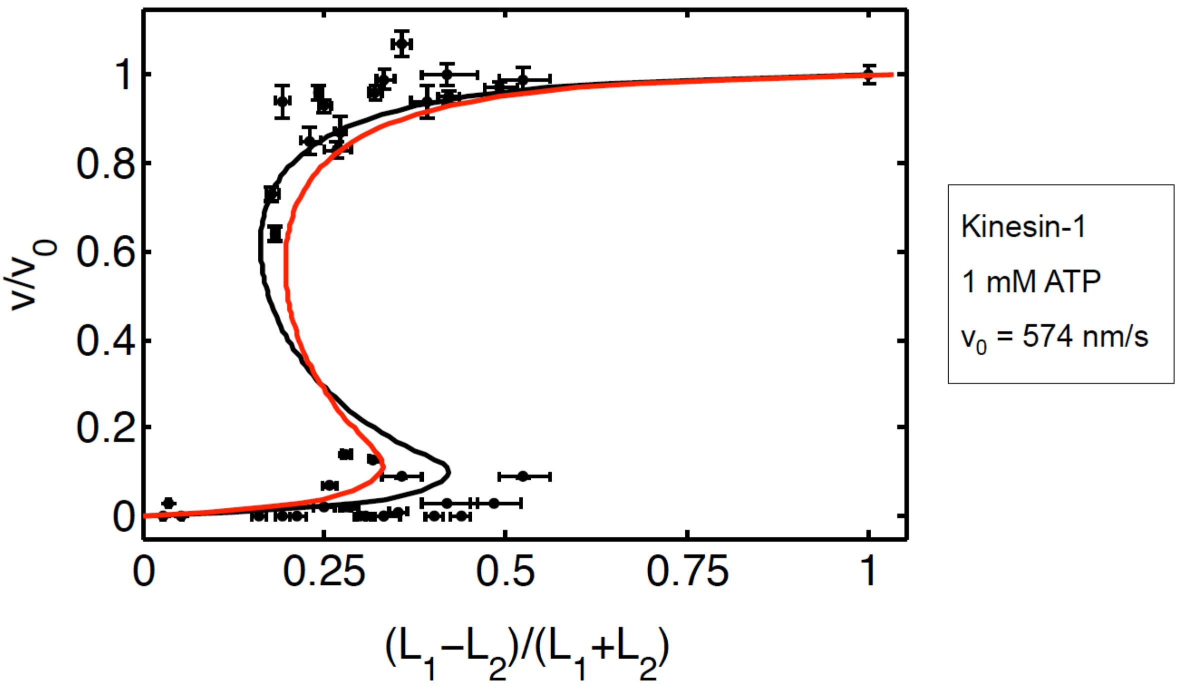

Figure 42. Theoretical results for doublets gliding on kinesin-1 at 1 mM ATP. Data corresponds to Figure 32. The two curves correspond to two different set of parameters for the model for processive motors: Black curve: f_c = 4.5 pN, ω_0 = 0.05/s, ω_{on} = 5/s, k = 2 pN/nm. Red curve: f_c = 8 pN, ω_0 = 0.5/s, ω_{on} = 3.5/s, k = 2 pN/nm.

In Figure 42 the two different theoretical curves are overlaid with the experimental data for kinesin-1 at 1 mM ATP. For the black curve f_c = 4.5 pN is assumed; for lower values of f_c the slow branch would be shorter. More critical is the fact that a higher processivity than measured has to be assumed (with f_c = 4.5 pN) in order to achieve a bistability. Here the detachment rate ω_0 = 0.05/s is about 10x lower than the value measured in chapter 3. Of course it might simply be possible that motors in a gliding geometry really exhibit a different run length than in the stepping assay. This is indicated by older experiments from Howard et al. [Howard et al, 1989], which were later on explained by unobserved, fast rebinding of the microtubule. The second plot in red relies on a detachment rate much closer to the experimentally determined value, ω_0 = 0.5/s. In order to achieve a bistability under this condition, the characteristic force and the attachment rate have to be changed, here the following values are used: f_c = 8 pN and ω_{on} = 3.5/s. These values make it more difficult to explain the theoretical results for the low ATP case, because f_c and ω_{on} are not expected to vary strongly in dependence of the stepping rate.

The theoretical result for kinesin-1 at low ATP concentration is shown in Figure 43, values of f_c = 3 pN and ω_0 = 0.05/s are used. The value for f_c is in agreement with the literature value and ω_0 = 0.05/s corresponds to the measured detachment rate. Thus the theory is able to explain the low ATP case more consistently than the high ATP case.

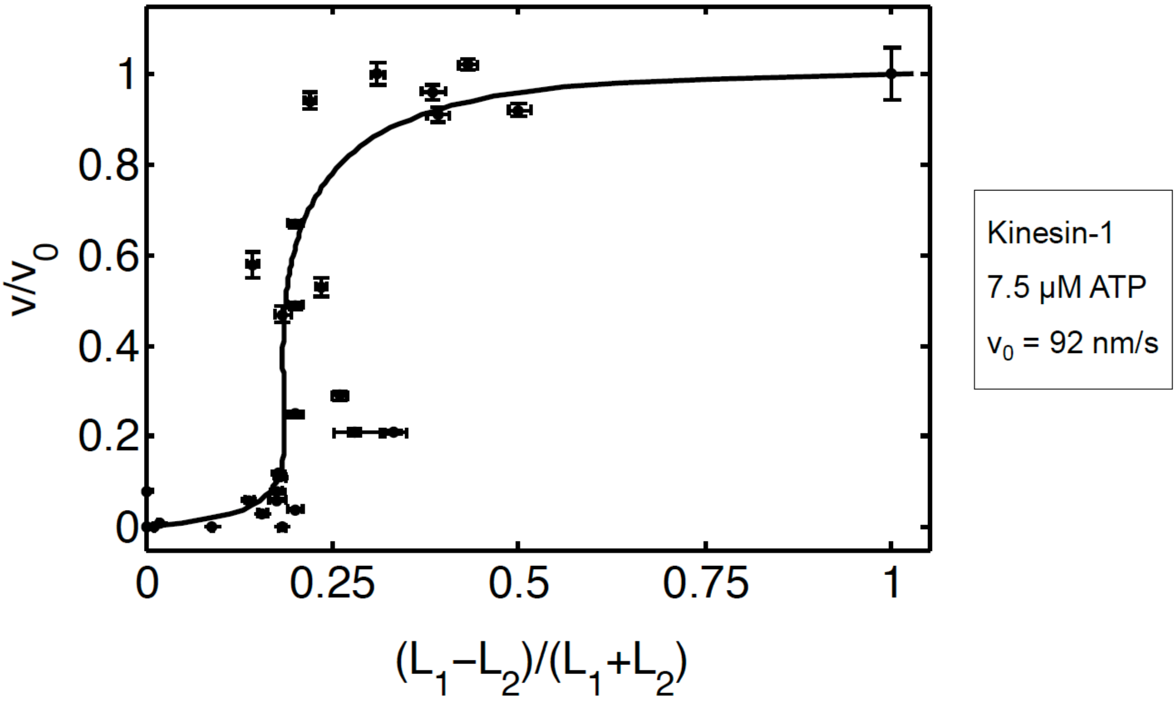

Figure 43. Theoretical results for doublets gliding on kinesin-1 at 7.5 µM ATP. Data corresponds to Figure 33. The theoretical curve is obtained with the model for processive motors and the following parameters: f_c = 3 pN, ω_0 = 0.05/s, ω_{on} = 5/s, k = 2 pN/nm.

For cytoplasmic dynein ω_{on}, f_c and k are not known. Single-molecule tweezing experiments indicate, that force-dependent detachment is not very strong for dynein, thus f_c should be high. Furthermore the stiffness should be similar to kinesin, maybe a little bit higher, since the particular construct is very short and therefore stiff. The best agreement between theory and the experimental data is plotted in black in Figure 44 and is obtained (with the restriction k = 2 pN/nm) with ω_{on} = 1/s, f_c = 2.5 pN and ω_0 = 0.005/s. The problem is similar to the case of kinesin at high ATP: an unusually long run length (and therefore low detachment rate ω_0) has to be assumed. A second set of parameters with ω_0 = 0.04/s, f_c = 5 pN and ω_{on} = 0.5/s results in the red plot in Figure 44.

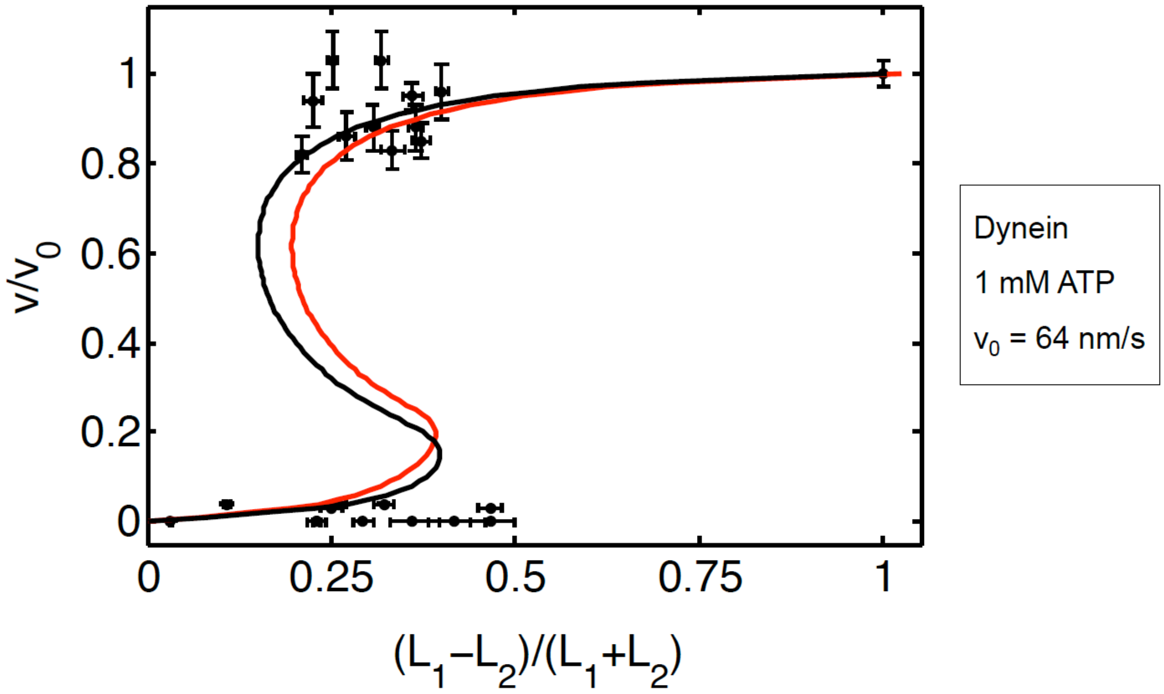

Figure 44. Theoretical results for doublets gliding on dynein. Data corresponds to Figure 34. The two curves correspond to two different set of parameters for the model for processive motors: Black curve: f_c = 2.5 pN, ω_0 = 0.005/s, ω_{on} = 1/s, k = 2 pN/nm. Red curve: f_c = 5 pN, ω_0 = 0.04/s, ω_{on} = 0.5/s, k = 2 pN/nm.

For Ncd there is even less quantitive data about the single-molecule response to force. It is know that the motor is non-processive, the length of the power stroke is 9 nm, and the stiffness should be comparable with the one of kinesin-1. The value for the detachment rate ω_0 was measured to be ~ 1/s at saturating ATP [deCastro et al, 2000]. This value contradicts, however, the constant gliding velocity of 200 nm/s, which can already be achieved by five motors [deCastro et al, 1999]. Even if these 5 motors show maximal positive cooperativity and attach immediately, more than four power strokes per second and motor are necessary to achieve 200 nm/s. Thus the motors must detach more frequently than once per second. It is, furthermore, known, that the power stroke is performed typically at the end of the binding cycle. In terms of the three-state model this corresponds to a value of ω_p comparable to ω_0. The force dependent detachment of Ncd is not characterized, yet. A very strongly force dependent detachment might compensate for a low value of ω_0, but this is not assumed here. Figure 45 shows that the three-state model is not able to describe the experimental results quantitatively with parameters obeying the previous considerations. The very slow motility of some doublets is not captured by the theoretical curve depicted in black.

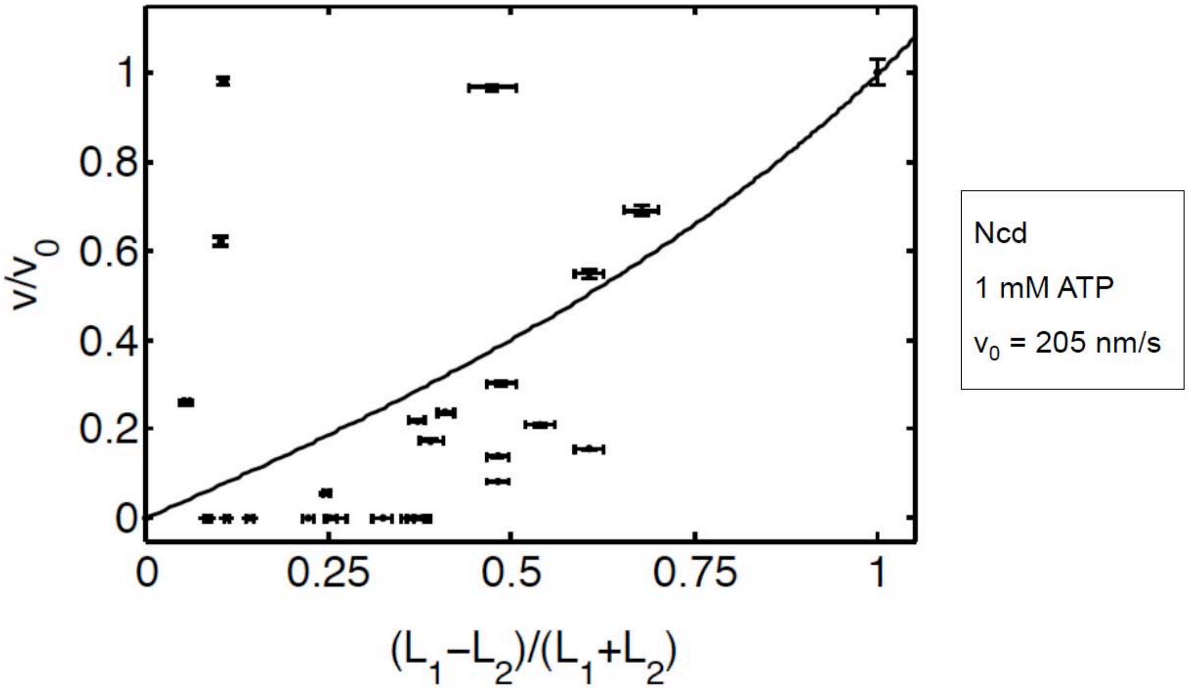

Figure 45. Theoretical results with the three-state model for doublets gliding on Ncd. Data corresponds to Figure 35. The parameters according to the three-state model for non-processive motors are f_c = 4 pN, ω_0 = 50/s, ω_{on} = 50/s, k = 1.65 pN/nm and ω_p = 140/s.

5.5 Discussion

The aim of chapter 5 is to describe the collective behavior of antagonizing motors experimentally and theoretically. In particular I want to answer the question under which experimental conditions doublets gliding on motors show bistable behavior. Here three different motor proteins were tested: kinesin-1, dynein, and the kinesin-14 Ncd. The motility of antagonizing kinesin-1 motors was investigated at different ATP concentrations and therefore at different velocities.

For kinesin-1 at 1 mM ATP with a run length of about 2 µm (and therefore a detachment rate $\omega_0 \approx 0.4$/s) a bistability was not expected. Here bistability means, that two different velocity regimes can be achieved by the same normalized ratio of antagonizing motors. The experiments showed, however, clearly the existence of a bistability, which is comparable to the bistability by antagonizing superprocessive motors with $\omega_0 \approx 0.01$/s [Leduc et al, 2010]. Thus the following problem occurs: previously measured values for single-motor properties contradict the necessary parameters for achieving a reasonable agreement of the multi-motor theory with the experimental data of my doublet experiments. This surprising bistability for kinesin-1 at 1 mM ATP can be explained easily, if the motors are more processive than measured (by at least a factor of 10). Thus the question is raised in how far motors in a gliding geometry might exhibit a different run length than in the stepping geometry. If the hypthesis, that the run length in the gliding geometry is higher than in the stepping gemoetry, holds true, then it is, however, difficult to explain the results for kinesin-1 in the low ATP case.

For the doublets gliding on dynein a bistability was observed as well. Dynein has a low maximal velocity at 1 mM ATP compared to kinesin-1. In order to explain a bistability with the current theory at such a low velocity, it is necessary, to assume a very low detachment rate. It should be noted, that the force-dependent detachment rate of dynein is, however, not well characterized. It would be very interesting to measure the (force dependent) run length of dynein in dependence of different ATP and salt concentrations in single-molecule experiments. These results of such experiments would allow more precise predictions of the doublet behavior and would provide, therefore, a more rigorous test of the theory.

The doublet experiments with Ncd indicate, that this motor does not exhibit a bistability. The theory is able to explain qualitatively the absence of the bistability. A quantitative agreement is, however, not possible. The contradiction between data and experiments is not as pronounced as for processive motors, since fewer parameters are measured. Furthermore the data for the Ncd experiments is more scattered.

Despite the deviations between theoretical prediction and experimental results several conclusions can be drawn:

First of all, collectively antagonizing processive motors exhibit a bistability even at run lengths around 2 - 4 µm. Second, a theory based on established assumptions about single- and multi-motor properties is able to account for this observation qualitatively. Third, such a bistability can even occur at low velocities below v_0 = 100 nm/s of single freely gliding microtubules. The occurence of the bistability depends on the properties of the individual molecules, most likely on the stiffness and/or the force dependent detachment rate. Fourth, antagonizing non-processive Ncd motors are not able to provide a bistability under standard conditions.

These findings can be compared to the *in vivo* function of the motors. As laid out in chapter 1, cytoplasmic dynein and kinesin-1 are mainly involved in intracellular transport and often antagonize other motors. Even cargo with several antagonizing motors moves often with the velocity of a single motor (interrupted by pauses or changes of direction), see e.g. [Soppina et al, 2009]. The experimental results obtained here support the idea, that a tug-of-war is often sufficient for determining the velocity and direction of cargo.

In the meiotic prophase of the fission yeast *S. pombe* multiple dynein motors antagonize each other in geometrical constraints, which are very similar to the doublet assay. *In vivo* only fast movement without intermediate velocities is observed. This type of movement corresponds to the fast branch of the *in vitro* doublet experiments with dynein. The existence of a slow branch *in vivo* might be prevented by an elevated detachment rate of the motors due to detachment from the cortex (surface), which does not exist *in vitro*.

Multiple Ncd motors are, on the other hand, involved in setting the spindle length together with a different kind of antagonizing motors. The results shown here indicate that Ncd is able to respond more continuously to antagonizing motors (with similar properties), which might help in setting the spindle length via a force balance.

The general bottleneck for this kind of experiments is, of course, a reliable protocol for producing doublets. The two problems which might (and did) occur are a) the quality of the polarity marking and b) the stability of the doublets themselves. Although standard protocols for polarity marking are available, they provided good results for only less than 50% of all experiments. The second, more severe problem is the production of doublets, which are able to withstand the high forces exerted by the antagonizing motors. Attempts to use biotinylated microtubules with neutravidin as a connecting molecule failed, and thus the "brute force" method of chemical crosslinking (additionally to the antibody connection between the two microtubules) was applied. But even this method did not provide a satisfactory yield. On average only 1 - 2 antiparallel doublets were found per successful experimental day - and at least 50% of all experimental attempts are not counted here at all, because the polarity marking was not satisfactory.

Once a more stable doublet protocol is developed, this assay can be applied to many different conditions to test the theoretical predictions more carefully, not only for the effect of the velocity, but also for the effect of run length and other parameters. It might also be interesting to apply the assay to other motors, in particular axonemal dynein, because its *in vivo* role is to facilitate collective motility coordinated by a tug-of-war. It might be, furthermore, interesting to extend the assay to dynamic microtubules in order to mimic the *in vivo* situation, e.g. in the fission yeast *S. pombe*, better. Dynamic microtubule (+) ends would also allow probing the transitions between the different branches in more detail. It is expected, that transitions from the fast to the slow branch and vice versa lead to a hysteresis.

6 Materials and Methods

6.1 List of chemicals and equipment

ATP	Roche	519979
NaCl	Merck	1.06404.1000
MgCl2	Merck	1.05833.1000
GMPCPP	JenaBioScience	NU-405L
GTP	Sigma	49601
PIPES	Sigma	80635
Casein	Sigma	C7078
DTT	Sigma	43815
Catalase	Sigma	C9322
Glucose	Sigma	G7528
Glucose oxidase	Sigma	G2133
KAcetate	AppliChem	A4279,0500
MgAcetate	AppliChem	A69699,0500
EGTA	Sigma	E4378
Glycerol	Merck	1.04092.1000
HEPES	Roth	9105.3
Ethanol	VWR	20821.330
Mucasol	Merz	60434
Anti-ß-tubulin antibody clone SAP.4G5	Sigma	T7816
TAMRA	Invitrogen	C-1171
AlexaFluor 488	Invitrogen	A-30005
BS3	ThermoScientific	21580
Anti-GST antibody	antibodies-online.com	ABIN120765
Anti-GFP antibody	Facility MPI-CBG	
TEV protease	Facility MPI-CBG	
Dynabead M280	Invitrogen	112.06D
Coverslips 18x18mm	Corning	2870-18
Coverslips 22x22mm	Corning	2870-22
Parafilm	Pechiney	PM-996
Pluronic F127	Sigma	P2443
Biotinylated tubulin	Cytoskeleton	T333
2-mercapto-ethanol	Sigma	M-370-1
Paclitaxel	Sigma	T7191
Trichloroethylene	Merck	M 1.11872.1000
Hydrogen peroxide	Sigma	21.6767-3
Sulfuric acid	Merck	1.00732.2500
KOH	Sigma	P6310
Acetone	VWR	1.00014
MOPS running buffer	Invitrogen	NP0001
IgG sephareos	GE Healthcare	17-0969-01
N-Ethylmaleimide	Sigma	E1271
TetraSpeck beads 0.1µm	Invitrogen	T7279
TetraSpeck beads 0.2µm	Invitrogen	T-7280
NuPage 7% TA Gel	Invitrogen	EA0355

NuPage 4-12% BT Gel	Invitrogen	NP0322
Protein ladder PageRuler	Fermentas	SM0661
Protein ladder HiMark	Invitrogen	LC5699
Film	GE Healthcare	28906835
Detection reagents	GE Healthcare	RPN2106
Milk powder	Heirler	
Anti-TAMRA antibody	Invitrogen	A6397
MicroSpin Column	GE Healthcare	27-3565-01
Simply Blue SafeStain	Invitrogen	LC6065
Capillaries	VitroCom	
Quantum Dots 655 Streptavidin	Invitrogen	Q10121MP
Protease Inhibitor	Roche	04693159001
Benzonase	Novagen	70746-4
DNAse1	Facility MPI-CBG	
Ampicillin	Sigma Aldrich	A9518
Chlorampphenicol	Roth	3886.1
Pefabloc	Sigma	76307
Leupeptin	AppliChem	A2183,0010
Pepstatin A	Sigma	P5318
Tris	Roth	4855.2
Sucrose	Fluka	84100
IPTG	Fermentas	R0392
Na_2HPO_4 * H_20	Merck	1.06346.0500
Imidazole	Sigma	I2399
LB medium	Media kitchen MPI-CBG	
PBS	Media kitchen MPI-CBG	
HiTrap chelating column	GE Healthcare	17-0408-01
HiTrap sepharose column	GE Healthcare	17-1151-01
Silicone Fluid 500cps	Brookfield	
Optima LE-80K	Beckman Coulter	
Optima MAX	Beckman Coulter	
Airfuge	Beckman Coulter	

6.2 Buffer recipes

BRB 80
80 mM PIPES pH 7.2
1 mM $MgCl_2$
1 mM EGTA

BRB 80 C
BRB 80
0.5mg/ml casein

BRB 80 CA
BRB 80C
ATP as desired (e.g. 1 mM ATP)

Dynein lysis buffer (DLB)
30 mM HEPES pH 7.2
50 mM KAcetate
2 mM MgAcetate
1 mM EGTA
10% glycerol

DLB C
DLB
0.5 mg/ml casein

DLB CA
DLB C
ATP as desired (e.g. 1 mM ATP)

BRB 80 MOT
BRB 80
0.1 mg/ml casein
0.02 mg/ml catalase
20 mM glucose
0.02 mg/ml glucose-oxidase
10 mM DTT
ATP as desired (e.g. 1mM ATP)

HEM 10
10 mM HEPES pH 7.2
1 mM EGTA
1 mM $MgCl_2$

HEM 50
50 mM HEPES pH 7.2
1 mM EGTA
1 mM MgCl2

HEM 10 Na
HEM10
100 mM NaCl

HEM 10 CA
HEM 10 Na
0.2 mg/ml casein
0.1 mM ATP
10 mM DTT

HEM 50 CA
HEM 50 Na
0.2 mg/ml casein
0.1 mM ATP
10 mM DTT

HEM 50 MOT
HEM 50 Na
0.2 mg/ml casein
0.02 mg/ml catalase
20 mM glucose
0.02 mg/ml glucose-oxidase
10 mM DTT
ATP as desired (e.g. 1 mM ATP)

DLB MOT
DLB
0.2 mg/ml casein
0.02 mg/ml catalase
20 mM glucose
0.02 mg/ml glucose-oxidase
10 mM DTT
ATP as desired (e.g. 1 mM ATP)

Ncd lysis buffer
HEM 10
50 mM NaCl
50 µM ATP
0.5 mM DTT
Protease inhibitor (1 tablet / 50ml)

Ncd elution buffer
Hem 10
250 mM NaCl
50 µM ATP
0.5 mM DTT
Protease inhibitor (1 tablet / 50ml)

Buffer A
50 mM Na_2HPO_4
300 mM NaCl
10 % glycerol
1 mM $MgCl_2$
10 µM ATP
Protease inhibitor (1 tablet / 50ml)

Buffer B
Buffer A
300 mM imidazole

Lysis buffer
Buffer A
40 mM imidazole

6.3 Protein purification

Expression of Ncd195-700GST

Pick a single colony of the bacterial strain BL21(DE3)pRARE with the pGEX4T1Ncd195-700 plasmid and inoculate in 5 ml of LB medium with antibiotics

(1 mg/ml ampicillin and 0.34 mg/ml chlorampicillin), henceforth denoted LB_A. Grow the pre-culture at 37°C, shaking at 180 rpm, overnight (~ 16 hours). Add 1 ml of the pre-culture to 375 ml of LB_A and let it grow at 37°C, shaking with 180 rpm, up to an OD600 of 1.2 (typically during the day time). Add 375 ml of 4°C cold LB_A with 1 mM IPTG to start the over-expression of Ncd, and incubate the cell culture overnight (~ 16 hours) at 15°C, shaking with 180 rpm.

Spin the cell culture at 8000 g with a pre-cooled JLA-8.1000 rotor (Beckman Coulter) for 10 minutes at 4°C. Discard the supernatant and keep the pellet in the centrifuge tubes on ice. Wash the pellet with 4°C cold HEM10, weigh the pellets and suspend the pellets in 4°C HEM10 (1 ml buffer for 1 g of cells). Freeze the cells by dropping the cell suspension into liquid nitrogen. Store the frozen cells at -80°C (or proceed directly with the next step).

Purification of Ncd195-700GST

Add 8 ml of Ncd lysis buffer for 2 ml unfrozen cell suspension. Add benzonase to reach a final concentration of 12.5 U/ml and DNAse1 to reach 2 U/ml. Keep the solution on ice. Lyse the cells, e.g. via French press or with mortar and pestle. Centrifuge the lysate at 25 000 g for 30 minutes with a pre-cooled Ti-45 rotor (Beckammn Coulter) at 4°C. Centrifuge the supernatant at 140 000 g for 120 minutes with a pre-cooled Ti-45 rotor at 4°C.

The following procedure is carried through in the cold room and with pre-cooled buffer solutions. The flow rates should be kept below 1ml/minute. Saturate a HiTrap sepharose column with 3 M NaCl. Equilibrate the column with Ncd lysis buffer and load the sample. Wash with Ncd lysis buffer before collecting the protein (in 0.5 ml fractions) by flowing the Ncd elution buffer through the column.

Check the protein concentration and add sucrose (in HEM 10) to reach a final concentration of 10% (w/v) sucrose to the fractions with high protein content. Make 5 µl aliquots, freeze them in liquid nitrogen and store them at -80°C.

Expression and purification of cytoplasmic dynein (VY 208)

See [Reck-Peterson et al, 2006]

Comment: The microtubule spin down step was not carried through.

Expression of full-length kinesin-1 and truncated kinesin-1 (rkin430$_{GFP}$)

The protocol equals essentially the expression of Ncd195-700GST. The pPK113 plasmid is used for the full length kinesin-1 [Hancock & Howard, 1998], while the rkin430$_{GFP}$ plasmid is described in [Rogers et al, 2001]. Instead of HEM10 the buffer PBS is used for washing and suspending the cells.

Purification of full-length kinesin-1 and truncated kinesin-1 (rkin430$_{GFP}$)

The protocol equals the purification of Ncd up to the centrifugation step. Instead of Ncd lysis buffer, however, a kinesin lysis buffer is used. The two centrifugation steps can be replaced by one step at 100 000 g for one hour.

The actual purification is carried through via chromatography on a HiTrap chelating column (column volume (CV): 1 ml). The metals should be stripped off the column a day before. In the following steps the flow rates should be kept below 1ml/minute. The whole procedure is carried through in the cold room and with pre-cooled buffer solutions. Equilibrate with 10 CV of 3% Buffer B + 97% Buffer A. Wash with 10 CV of 10% buffer B (+ 90% buffer A). Wash with 10 CV of 30% Buffer B (+ 70% buffer A). Elute with 10 CV of 100% Buffer B and collect 0.5 ml fractions.

Check the protein concentration and add sucrose (in buffer B) to reach a final concentration of 10 % (w/v) sucrose to the fractions with high protein content. Make 5 µl aliquots, freeze them in liquid nitrogen and store them at -80°C.

Tubulin purification
The tubulin was purified from pig's brain according to a standard protocol available at:
http://mitchison.med.harvard.edu/protocols/tubprep.html

Tubulin labeling
The tubulin was labeled according to a standard protocol available at:
http://mitchison.med.harvard.edu/protocols/label.html

6.4 Preparation of microtubules

Seeds for polarity marked microtubules
Grow microtubules from 5.7 µM porcine tubulin (TAMRA labeling ration 1:8), 1 mM GMPCPP and 1 mM $MgCl_2$ in BRB 80 at 37°C for 90 minutes. Then spin microtubules down in an Airfuge with 25 psi for 5 minutes. Elute spun down microtubules do yield a final concentration of 18 µM (assuming 90% polymerization rate).

Polarity marked microtubules
Incubate 1.6 µM porcine tubulin (TAMRA and Alexa-488 labeling ratio each 1:8) with 1 mM $MgCl_2$, 1 mM GMPCPP and 10 µM N-Ethylmaleimide for 5 minutes on ice (39 µl). Quench with 1 µl 1:5 2-mercapto-ethanol for 5 minutes on ice. Pre-warm this extension mix for 10 seconds at 37°C in a heat block. Add 10 µl of seeds and let extensions grow for 20 minutes. Add 50 µl BRB 80 and proceed directly with next step.

Doublets with polarity marked microtubules
Mix 4 µl polarity marked microtubules with 1 µl diluted anti-tubulin antibodies (1:40) and incubate for 5 minutes. Add 45 µl 2 mM BS^3 in BRB 80 and incubate for 30 minutes. Add 1 µl 1 M Tris-HCl and quench for 30 minutes.

Bright TAMRA microtubules
Grow microtubules from 2 µM porcine tubulin (TAMRA labeling ration 1:4), 1 mM GMPCPP and 1 mM $MgCl_2$ in BRB 80 at 37°C for 120 minutes. Then spin microtubules down in an Airfuge with 25 psi for 5 minutes. Elute spun down microtubules do yield a final concentration of 1.8 µM (assuming 90% polymerization rate)

Bright / dim TAMRA biotinylated microtubules
Grow microtubules from 2.4 µM porcine tubulin (TAMRA labeling ration 5:24 for bright and 1:40 for dim microtubules, biotin labeling ratio 1:6), 1 mM GMPCPP and 1 mM $MgCl_2$ in BRB 80 at 37°C for 120 minutes. Then spin microtubules down in an Airfuge with 25 psi for 5 minutes. Elute spun down microtubules to yield a final concentration of 2.16 µM (assuming 90% polymerization rate).

6.5 Preparation of flow cells

If not mentioned otherwise, all gliding and stepping assays including the tweezing experiments were carried through at room temperature (18°C - 23°C, typically 20°C).

Motor densities
The gliding assays for kinesin-1 should yield a nominal motor density of about 500 motors µm^{-2}, see [Fallesen et al, 2011b] and references therein. The density of functional motors for the Ncd and dynein gliding assays (in the absence of force) is at least as high as the density of functional motors in the kinesin-1 assay, because even shorter microtubules (below 1 µm) were gliding smoothly on Ncd and dynein coated surfaces. The dynein density in the magnetic tweezing experiments can be estimated from the fluorescence signal of the motors, see Figure 25, and were about 0.25 - 5 µm^{-2}.

Easy clean coverslips (capillaries)
Sonicate coverslips in 1:20 Mucasol (20 minutes), wash with de-salted water and dry completely with pressured air, sonicate in ethanol (20 minutes), wash first with desalted, then with nanopure water, dry completely with pressured air.

Silanized coverslips
Piranha solution: 75 ml hydrogen peroxide + 175 ml sulforic acid. Cleaning procedure for coverslips: acetone (55 minutes), ethanol (10 minutes), wash with desalted water, piranha solution (60 minutes at 60°C), wash with nanopure water, KOH (0.1 M, 15 minutes), wash with nanopure water, dry coverslips completely with pressured air. Silanization procedure: 200 ml TCE + 100 µl DDS (60 minutes), sonicate in methanol (first 5 minutes, then 15 minutes, then 30 minutes; exchange methanol after each step, wash with nanopure water, dry completely with pressured air.

Preparation of a flow cell
Cut four parafilm stripes of about 25 x 2 mm. Place them on a 22 x 22 coverslip (cleaned as needed), so that 3 channels with a width of about 2 mm are formed, with about 5 mm free space between the outer parafilm stripes and the edge of the coverslip. Put a 18 x 18mm coverslip (cleaned as needed) on top and heat the parafilm for about 10 seconds. Press the two slides gently together to yield tight channels. Cut of the overhanging parafilm with a scalpel.

Doublets assay kinesin-1
Use easy clean coverslips for the flow cell. Flow the following solutions (20 µl) through one channel of the flow cell. The incubation time is given in brackets.
1. BRB 80 C (5 minutes) 2. BRB 80 CA with 1:100 kinesin-1 (stock concentration of 0.6 mg/ml). (5 minutes). 3. BRB 80 CA 4. BRB 80 MOT with 1:20 doublets (5 minutes) 5. 2 x BRB 80 MOT

Doublets assay dynein
Use easy clean coverslips for the flow cell. Flow the following solutions (20 µl) through one channel of the flow cell. The incubation time is given in brackets.

1. anti-EGFP antibody (15 µg/ml) in DLB (5 minutes) 2. 2 x DLB C 3. DLB C (5 minutes). 4. DLB CA with 1:20 VY 208 (stock concentration: 0.5 mg/ml) (5 minutes) 5. DLB CA 6. DLB MOT with 1:20 doublets (5 minutes) 7. 2 x DLB MOT

Doublet assay Ncd

Use silanized coverslips for the flow cell. Flow the following solutions (20µl) through one channel of the flow cell. The incubation time is given in brackets.
1. 0.1 mg/ml anti-GST antibody in PBS (5 minutes) 2. 2 x 1% F127 in PBS 3. 1% F 127 in PBS (30 minutes) 3. 2 x PBS 4. HEM 10 Na 4. HEM 10 CA with 1:20 Ncd (stock concentration: 1.5 mg/ml) (10 minutes) 5. 2 x HEM 50 CA 6. HEM 50 MOT with 1:20 doublet solution 7. 2 x HEM 50 MOT

ATP dependent gliding of dynein

Use easy clean coverslips for the flow cell. Flow the following solutions (20 µl) through one channel of the flow cell. The incubation time is given in brackets.
1. anti-EGFP antibody (15 µg/ml) in DLB (5 minutes) 2. 2 x DLB C 3. DLB C (5 minutes). 4. DLB CA with low ATP concentration and 1:20 VY 208 (stock concentration: 0.5 mg/ml) (5 minutes) 5. DLB CA 6. DLB MOT with low ATP concentration and 1:100 bright TAMRA microtubules (5 minutes) 7. 2 x DLB MOT with increasing ATP concentration up to 1 mM ATP

ATP dependent gliding of kinesin-1

Use easy clean coverslips for the flow cell. Flow the following solutions (20 µl) through one channel of the flow cell. The incubation time is given in brackets.
1. BRB 80 C (5 minutes) 2. BRB 80 CA with low ATP concentration and 1:100 kinesin-1 (stock concentration of 0.6 mg/ml) (5 minutes). 3. BRB 80 CA with the low ATP concentration 4. DLB MOT with low ATP concentration and 1:100 bright TAMRA microtubules (5 minutes) 5. 2 x DLB MOT with increasing ATP concentration up to 1 mM ATP

ATP dependent gliding of Ncd

Use silanized coverslips for the flow cell. Flow the following solutions (20µl) through one channel of the flow cell. The incubation time is given in brackets.
1. 0.1 mg/ml anti-GST antibody in PBS (5 minutes) 2. 2 x 1% F127 in PBS 3. 1% F 127 in PBS (30 minutes) 3. 2 x PBS 4. HEM 10 Na 4. HEM 10 CA with 1:20 Ncd (stock concentration: 1.5 mg/ml) (10 minutes) 5. 2 x HEM 50 CA 6. HEM 50 MOT with low ATP concentration and 1:100 bright TAMRA microtubules 7. 2 x HEM 50 MOT with increasing ATP concentration up to 1mM ATP

Stepping assay kinesin-1

Use silanized coverslips for the flow cell. Flow the following solutions (20µl) through one channel of the flow cell. The incubation time is given in brackets.
1. Anti-TAMRA antibodies (1:100, 5 minutes) 2. 2 x 1% F127 in PBS 3. 1% F127 in PBS (30 minutes) 4. Bright TAMRA microtubules (1:100 in BRB 80, 5 minutes) 5. 2 x BRB 80 MOT 6. BRB 80 MOT with 1:10 000 rkin430 (stock concentration: 0.6 mg/ml).

Stepping assay dynein
Follow procedure for the stepping assay kinesin-1 up to step 3. Next steps: 4. Bright TAMRA microtubules (1:100 in DLB, 5 minutes) 5. 2 x DLB MOT 6. DLB MOT with 1:1000 VY 208 (stock concentration: 0.5 mg/ml)

Tweezing assay
Use an easy clean capillary. Flow the following solutions (100µl) through the capillary. The incubation time is given in brackets.
1. 1:100 200 nm TetraSpeck beads in BRB 80 for 40x objective or 1:1000 100 nm TetraSpeck beads in BRB 80 for 100x objective (5 minutes) 2. 2 x BRB 80 3. 10 µg/ml anti-EGFP antibody (5 minutes) 3. DLB CA (30 minutes) 4. 2 x DLB 5. DLB CA with 1:500-1:10 000 VY 208 (stock concentration: 0.5 mg/ml) 6. DLB CA with 0.04 µM bright TAMRA biotinylated microtubules (5 minutes) 7. DLB CA 8. DLB CA with 1% magnetic beads (5 minutes) 9. 2 x DLB MOT

Tweezing assay with quantum dots (for 100x objective)
As tweezing assay for 40x objective but use dim TAMRA biotinylated microtubules in step 5. Flow through two more solution between step 7 and 8: 7.1 DLB CA with 1:500 quantum dots (5 minutes) 7.2 DLB CA.

Temperature dependent gliding speed for dynein
The assay is essentially the same as for the ATP dependent gliding of dynein with 1 mM ATP.

Temperature dependent gliding speed for kinesin-1
The assay is essentially the same as for the ATP dependent gliding of kinesin-1 with 1 mM ATP.

Temperature dependent gliding speed for Ncd
The assay is essentially the same as for the ATP dependent gliding of Ncd with 1 mM ATP.

6.6 Fluorescence microscopy

Microscope Setup 1

Body	Olympus – IX 71 inverted
Objective	Olympus PlanApo 100x NA 1.45
Laser	Andor Laser Combiner with diode pumped solid state laser of 491 nm and 561 nm wavelength
Camera	Andor iXon EM DU 897-BV (16 µm pixel size)
Filters	Semrock BrightLine HC 525/30, Semrock BrightLine HC 617/73
Software	Andor iQ 1.9.1

Microscope Setup 2

Body	Zeiss Axiovert 200M
Objectives	Zeiss Plan Apochromate 40x NA 0.95 Zeiss Plan Neofluor 100x Oil NA 1.3 Zeiss Plan Apochromate 100x Oil-DIC NA 1.46
Laser	Coherent Innova 70c Spectrum 2.5 W

Lamp	Prior Lumen 200
Camera	Andor iXon EM DU 897-E (16 µm pixel size)
Filters	TRITC: excitation 535/50 nm, emission 610/75 nm
	FITC: excitation 480/40 nm, emission 535/50 nm
	quantum dot: excitation 488/10 nm, emission 660/50 nm
Software	MetaMorph 7.1.2.0
	National Instruments LabView 8.5
Transl. table	Physik Instrumente M-126.PD1 (y-axis)
	Physik Instrumente M-126.DG1 (z-axis)

Microscope Setup 3

Body	Zeiss Axiovert 200M
Objectives	Zeiss Plan Apochromate 40x NA 0.95
	Zeiss Plan Neofluor 100x Oil NA 1.3
Lamp	Prior Lumen 200
Camera	Princeton Instruments MicroMAX (13 µm pixel size)
Filters	TRITC: excitation 535/50 nm, emission 610/75 nm
	FITC: excitation 480/40 nm, emission 535/50 nm
Software	MetaMorph 7.1.7.0

The following assays have been carried out at Microscope setup 1

- Doublet experiments with kinesin-1, dynein and Ncd (100x, 100 ms illumination time, Δt = 1 - 10 s, sequential dual color imaging with 491 nm and 561 nm laser)
- ATP dependent gliding speed of dynein (100x NA, 100 ms illumination time, Δt = 1 -10 s)

The following assays have been carried out at Microscope setup 2

- Tweezing measurements with dynein motors (40x and 100x NA 1.46, 20 - 50 ms illumination time, stream acquisition, TRITC)
- TIRF for tweezing measurements with quantum dots and visualization of surface-bound dynein motors (100x NA 1.46, 100 ms illumination time with 488 nm laser, stream acquisition)
- Calibration of the magnetic tweezing setup (40x and 100x NA 1.46, TRITC, Δt = 1 s, TRITC)
- Doublet experiments with kinesin-1, dynein and Ncd (100x NA 1.3, 100 ms illumination time, Δt = 1 - 10 s, sequential dual color imaging, TRITC & FITC)
- Stepping assays for kinesin and dynein in TIRF mode (100x NA 1.46, Optavar 1.6, 100 ms illumination time with 488 nm laser; stream acqusiition (kinesin-1 at 1 mM ATP) or Δt = 0.5 s (kinesin-1 at 7.5 µm ATP and dynein at 1 mM ATP)

The following assays have been carried out at Microscope setup 3

- Temperature dependent gliding speed of dynein, kinesin-1 and Ncd (40x, 100 ms illumination time, Δt = 2 - 4 s, TRITC)
- ATP dependent gliding speed of kinesin-1 and Ncd (100x, 100 ms illumination time, Δt = 1 -10 s, TRITC)
- Doublet experiments with Ncd (100x, 100 ms illumination time, Δt = 1 - 5 s, sequential dual color imaging with lamp, TRITC & FITC filter)

6.7 Errors computation

The standard deviation σ for the data points x_i with $i = 1 \ldots N$ and the mean value $\mu = \frac{1}{N}\sum_{i=1}^{N} x_i$ is given by $\sigma = \sqrt{\frac{1}{N}\sum_{i=1}^{N}(x_i - \mu)^2}$. The standard error of the mean (SEM) σ_M is given by $\sigma_M = \frac{\sigma}{\sqrt{N}}$.

The error for the experimentally measured detachment rate $\Delta\omega_{exp}$ (see chapter 3) is given by $\Delta\omega_{exp} = \frac{\Delta v}{Rl_{ex}} + \frac{v}{Rl_{ex}^2}\Delta Rl_{exp}$ with the standard error of the Gaussian fit for the velocity v, Δv, and the standard error of the exponential fit for the run length Rl_{exp}, ΔRl_{exp}.

The velocity values in the magnetic tweezing experiments were obtained by fitting the tracked position values of the magnetic bead (or a quantum dot) along the y-axis against the time with a line. The slope corresponded to the velocity.

The real detachment rates of kinesin-1 and dynein, $\Delta\omega_0$, were obtained by fitting a line to the measured detachment rate in dependence of the illuminating laser power. The intercept of the line with the y-axis for the dependent variables (detachment rate) yielded the value for $\Delta\omega_0$.

All linear fits were performed with the least-mean-square algorithm. Thus the errors of the slope and the intercept correspond to the standard error of the fitting parameters. If the model for the linear fit is $y_i = \beta_0 + \beta\, x_i$ with the measured data points y_i and x_i and the fitting parameters β_0 and β , then it holds $\Delta\beta = \Delta e\sqrt{1/\sum_{i=1}^{N}(x_i - \mu)^2}$ and $\Delta\beta_0 = \Delta e\sqrt{1/N + \mu^2/\sum_{i=1}^{N}(x_i - \mu)^2}$. The global standard error of the fit is defined as $\Delta e = \sqrt{SSE/\nu}$. SSE is the sum-of-square error and given by $SSE = \sum_{i=1}^{N} e_i^2$ with $e_i = y_i - \hat{y}_i$ and the true value of the dependent variable y_i, the predicted value of the dependent variable (according to the fit) $\hat{y}_i$ and the index $i = 1 \ldots N$ where N is the number of data points used for fitting. $\nu = N - m$ corresponds to the degrees of freedom with the number of fitted variables m (for a linear fit $m = 2$).

Non-linear models (Gaussian, logarithmic, exponential) in this thesis were fitted by the Levenberg-Marquardt algorithm. The errors of fitting parameters for these non-linear models were also given as standard error of the fitting parameters. They can be generally expressed in the following way. If the model of the fit is $Y = f(X, \Theta) + \varepsilon$ with the independent variables $x = (x_1, \ x_2, \ldots, x_N)$ and the parameters $x = (\Theta_1, \Theta_2, \ldots, \Theta_N)$, then the Levenberg-Marquardt algorithm calculates the partial derivatives of the matrix F during each iteration step: $F_{ij} = \partial f(x, \theta)/\sigma_i^2 \partial\theta_j$. It holds that the standard error of the parameters is given by $s_{\Theta \mathrm{i}} = \sqrt{c_{ij}}$ with $C = (F'F)^{-1}\Delta e^2$.

6.8 Software

For the following figures (including data evaluation, fitting and calculation of the errors) OriginPro 7.5 was used:
10, 11, 13, 14, 15, 16

For the following figures (including fitting, FIESTA tracking and calculation of the errors) MathWorks Matlab 7.5.0 was used:

16, 20, 20, 21, 23, 24, 25, 26, 27, 29, 32, 33, 34, 35, 37-45

For the following figures (including data evaluation, but without acquisition) Metamorph (Version 7.1.2.0 - 7.7.0.0) was used:
9, 10, 11, 13, 14, 15, 16, 25, 32, 33, 34, 35, 42-45

For the following figures Fiji was used:
9, 12, 21, 25, 29, 30, 31, 32, 33, 34, 35, 42-45

For the following figures (including data evaluation, but without acquisition) Andor iQ 1.9.1 was used:
30, 31, 32, 33, 34, 35, 42-45

This thesis was written with Word:mac 2011

7 References

Allen RD, Allen NS, Travis JL (1981) Video-enhanced contrast, differential interference contrast (AVEC-DIC) microscopy: a new method capable of analyzing microtubule-related motility in the reticulopodial network of Allogromia laticollaris. *Cell Motil* **1:** 291-302

Allen RD, Metuzals J, Tasaki I, Brady ST, Gilbert SP (1982) Fast axonal transport in squid giant axon. *Science* **218:** 1127-1129

Ally S, Larson AG, Barlan K, Rice SE, Gelfand VI (2009) Opposite-polarity motors activate one another to trigger cargo transport in live cells. *J Cell Biol* **187:** 1071-1082

Asbury CL, Fehr AN, Block SM (2004) Kinesin moves by an asymmetric hand-over-hand mechanism. *Biophys J* **86:** 3a-3a

Atkins PW (1996) *Physikalische Chemie*: Wiley-VCH.

Badoual M, Julicher F, Prost J (2002) Bidirectional cooperative motion of molecular motors. *P Natl Acad Sci USA* **99:** 6696-6701

Beeg J, Klumpp S, Dimova R, Gracia RS, Unger E, Lipowsky R (2008) Transport of beads by several kinesin motors. *Biophys J* **94:** 532-541

Bieling P, Telley IA, Piehler J, Surrey T (2008) Processive kinesins require loose mechanical coupling for efficient collective motility. *Embo Rep* **9:** 1121-1127

Bieling P, Telley IA, Surrey T (2010) A Minimal Midzone Protein Module Controls Formation and Length of Antiparallel Microtubule Overlaps. *Cell* **142:** 420-432

Block SM (2007) Kinesin motor mechanics: Binding, stepping, tracking, gating, and limping. *Biophys J* **92:** 2986-2995

Block SM, Asbury CL, Shaevitz JW, Lang MJ (2003) Probing the kinesin reaction cycle with a 2D optical force clamp. *P Natl Acad Sci USA* **100:** 2351-2356

Block SM, Goldstein LS, Schnapp BJ (1990) Bead movement by single kinesin molecules studied with optical tweezers. *Nature* **348:** 348-352

Bohm KJ, Stracke R, Baum M, Zieren M, Unger E (2000) Effect of temperature on kinesin-driven microtubule gliding and kinesin ATPase activity. *Febs Lett* **466:** 59-62

Borisy GG, Olmsted JB (1972) Nucleated Assembly of Microtubules in Porcine Brain Extracts. *Science* **177:** 1196-&

Bormuth V, Jannasch A, Ander M, van Kats CM, van Blaaderen A, Howard J, Schaffer E (2008) Optical trapping of coated microspheres. *Opt Express* **16:** 13831-13844

Brady ST (1985) A novel brain ATPase with properties expected for the fast axonal transport motor. *Nature* **317:** 73-75

Brady ST, Lasek RJ, Allen RD (1982) Fast axonal transport in extruded axoplasm from squid giant axon. *Science* **218:** 1129-1131

Braun M, Drummond DR, Cross RA, McAinsh AD (2009) The kinesin-14 Klp2 organizes microtubules into parallel bundles by an ATP-dependent sorting mechanism. *Nat Cell Biol* **11:** 724-U755

Braun M, Lansky Z, Fink G, Ruhnow F, Diez S, Janson ME (2011) Adaptive braking by Ase1 prevents overlapping microtubules from sliding completely apart. *Nat Cell Biol* **13:** 1259-1264

Campas O, Sens P (2006) Chromosome oscillations in mitosis. *Phys Rev Lett* **97**

Carter AP, Garbarino JE, Wilson-Kubalek EM, Shipley WE, Cho C, Milligan RA, Vale RD, Gibbons IR (2008) Structure and functional role of dynein's microtubule-binding domain. *Science* **322:** 1691-1695

Carter NJ, Cross RA (2005) Mechanics of the kinesin step. *Nature* **435:** 308-312

Case RB, Pierce DW, HomBooher N, Hart CL, Vale RD (1997) The directional preference of kinesin motors is specified by an element outside of the motor catalytic domain. *Cell* **90:** 959-966

Coy DL, Wagenbach M, Howard J (1999) Kinesin takes one 8-nm step for each ATP that it hydrolyzes. *J Biol Chem* **274:** 3667-3671

Crevenna AH, Madathil S, Cohen DN, Wagenbach M, Fahmy K, Howard J (2008) Secondary Structure and Compliance of a Predicted Flexible Domain in Kinesin-1 Necessary for Cooperation of Motors. *Biophys J* **95:** 5216-5227

deCastro MJ, Fondecave RM, Clarke LA, Schmidt CF, Stewart RJ (2000) Working strokes by single molecules of the kinesin-related microtubule motor ncd. *Nat Cell Biol* **2:** 724-729

deCastro MJ, Ho CH, Stewart RJ (1999) Motility of dimeric ncd on a metal-chelating surfactant: Evidence that ncd is not processive. *Biochemistry-Us* **38:** 5076-5081

DeWitt MA, Chang AY, Combs PA, Yildiz A (2011) Cytoplasmic Dynein Moves Through Uncoordinated Stepping of the AAA+ Ring
Domains. *Sciencexpress*

Dixit R, Ross JL, Goldman YE, Holzbaur EL (2008) Differential regulation of dynein and kinesin motor proteins by tau. *Science* **319:** 1086-1089

Dogterom M, Kerssemakers JW, Romet-Lemonne G, Janson ME (2005) Force generation by dynamic microtubules. *Current opinion in cell biology* **17:** 67-74

Dogterom M, Yurke B (1997) Measurement of the force-velocity relation for growing microtubules. *Science* **278:** 856-860

Dujovne I, van den Heuvel M, Shen Y, de Graaff M, Dekker C (2008) Velocity Modulation of Microtubules in Electric Fields. *Nano Lett* **8:** 4217-4220

Einstein A (1905) Über die von der molekularkinetischen Theorie der Wärme geforderte Bewegung von in ruhenden Flüssigkeiten suspendierten Teilchen. *Annalen der Physik* **322:** 549–560

Elowitz MB, Surette MG, Wolf PE, Stock JB, Leibler S (1999) Protein mobility in the cytoplasm of Escherichia coli. *J Bacteriol* **181:** 197-203

Endow SA, Henikoff S, Soler-Niedziela L (1990) Mediation of meiotic and early mitotic chromosome segregation in Drosophila by a protein related to kinesin. *Nature* **345:** 81-83

Endow SA, Higuchi H (2000) A mutant of the motor protein kinesin that moves in both directions on microtubules. *Nature* **406:** 913-916

Endow SA, Waligora KW (1998) Determinants of kinesin motor polarity. *Science* **281:** 1200-1202

Endres NF, Yoshioka C, Milligan RA, Vale RD (2006) A lever-arm rotation drives motility of the minus-end-directed kinesin Ncd. *Nature* **439:** 875-878

Fallesen TL, Macosko JC, Holzwarth G (2011a) Force-velocity relationship for multiple kinesin motors pulling a magnetic bead. *Eur Biophys J* **40:** 1071-1079

Fallesen TL, Macosko JC, Holzwarth G (2011b) Measuring the number and spacing of molecular motors propelling a gliding microtubule. *Phys Rev E Stat Nonlin Soft Matter Phys* **83:** 011918

Fink G, Hajdo L, Skowronek KJ, Reuther C, Kasprzak AA, Diez S (2009) The mitotic kinesin-14 Ncd drives directional microtubule-microtubule sliding. *Nat Cell Biol* **11:** 717-723

Flemming W (1878) Beiträge zur Kenntniss der Zelle und ihrer Lebenserscheinungen. *Archiv für Mikroskopische Anatomie* **16:** 302-436

Flemming W (1880) Beiträge zur Kenntniss der Zelle und ihrer Lebenserscheinungen. *Archiv für Mikroskopische Anatomie* **18:** 151-289

Galvani L (1792) De viribus electricitatis in motu musculari.

Gennerich A, Carter AP, Reck-Peterson SL, Vale RD (2007) Force-induced bidirectional stepping of cytoplasmic dynein. *Cell* **131:** 952-965

Geyer V (2008) Influencing Kinesin-Microtubule Systems by Application of Magnetic Forces. Dipl.-Biophys. Thesis, Mathematisch-Naturwissenschaftliche Fakultät, Humboldt-Universität zu Berlin, Berlin

Gibbons IR, Rowe AJ (1965) Dynein - a Protein with Adenosine Triphosphatase Activity from Cilia. *Science* **149:** 424-&

Grill SW, Howard J, Schaffer E, Stelzer EH, Hyman AA (2003) The distribution of active force generators controls mitotic spindle position. *Science* **301:** 518-521

Grill SW, Kruse K, Julicher F (2005) Theory of mitotic spindle oscillations. *Phys Rev Lett* **94**

Guerin T, Prost J, Joanny JF (2011) Dynamical behavior of molecular motor assemblies in the rigid and crossbridge models. *Eur Phys J E* **34**

Hancock WO, Howard J (1998) Processivity of the motor protein kinesin requires two heads. *J Cell Biol* **140:** 1395-1405

Helenius J, Brouhard G, Kalaidzidis Y, Diez S, Howard J (2006) The depolymerizing kinesin MCAK uses lattice diffusion to rapidly target microtubule ends. *Nature* **441:** 115-119

Hendricks AG, Perlson E, Ross JL, Schroeder HW, Tokito M, Holzbaur ELF (2010) Motor Coordination via a Tug-of-War Mechanism Drives Bidirectional Vesicle Transport. *Curr Biol* **20:** 697-702

Henningsen U, Schliwa M (1997) Reversal in the direction of movement of a molecular motor. *Nature* **389:** 93-96

Hentrich C, Surrey T (2010) Microtubule organization by the antagonistic mitotic motors kinesin-5 and kinesin-14. *The Journal of cell biology* **189:** 465-480

Hill AV (1910) The possible effects of the aggregation of the molecules of hæmoglobin on its dissociation curves. *Proceedings of the Physiological Society* **40:** 389-403

Hooke R (1665) *Micrographia: Or, Some physiological descriptions of minute bodies made by magnifying glasses*.

Howard J (2009) Mechanical Signaling in Networks of Motor and Cytoskeletal Proteins. *Annual Review of Biophysics* **38:** 217-234

Howard J, Hudspeth AJ, Vale RD (1989) Movement of microtubules by single kinesin molecules. *Nature* **342:** 154-158

Howard J, Hyman AA (2003) Dynamics and mechanics of the microtubule plus end. *Nature* **422:** 753-758

Hunt AJ, Gittes F, Howard J (1994) The Force Exerted by a Single Kinesin Molecule against a Viscous Load. *Biophys J* **67:** 766-781

Huxley AF, Niedergerke R (1954) Structural Changes in Muscle during Contraction - Interference Microscopy of Living Muscle Fibres. *Nature* **173:** 971-973

Huxley AF, Simmons RM (1971) Proposed mechanism of force generation in striated muscle. *Nature* **233:** 533-538

Huxley H, Hanson J (1954) Changes in the Cross-Striations of Muscle during Contraction and Stretch and Their Structural Interpretation. *Nature* **173:** 973-976

Inoue S, Sato H (1967) Cell Motility by Labile Association of Molecules - Nature of Mitotic Spindle Fibers and Their Role in Chromosome Movement. *J Gen Physiol* **50:** 259-&

Jackson JD (1998) *Classical Electrodynamics*, 3rd edn.

Jamison DK, Driver JW, Rogers AR, Constantinou PE, Diehl MR (2010) Two Kinesins Transport Cargo Primarily via the Action of One Motor: Implications for Intracellular Transport. *Biophys J* **99:** 2967-2977

Janke C, Kneussel M (2010) Tubulin post-translational modifications: encoding functions on the neuronal microtubule cytoskeleton. *Trends Neurosci* **33:** 362-372

Jeney S, Stelzer EHK, Grubmuller H, Florin EL (2004) Mechanical properties of single motor molecules studied by three-dimensional thermal force probing in optical tweezers. *Chemphyschem* **5:** 1150-1158

Julicher F, Prost J (1995) Cooperative molecular motors. *Phys Rev Lett* **75:** 2618-2621

Kapitein LC, Peterman EJG, Kwok BH, Kim JH, Kapoor TM, Schmidt CF (2005) The bipolar mitotic kinesin Eg5 moves on both microtubules that it crosslinks. *Nature* **435:** 114-118

Kardon JR, Reck-Peterson SL, Vale RD (2009) Regulation of the processivity and intracellular localization of Saccharomyces cerevisiae dynein by dynactin. *P Natl Acad Sci USA* **106:** 5669-5674

Kardon JR, Vale RD (2009) Regulators of the cytoplasmic dynein motor. *Nat Rev Mol Cell Biol* **10:** 854-865

Kawaguchi K, Ishiwata S (2000) Temperature dependence of force, velocity, and processivity of single kinesin molecules. *Biochem Bioph Res Co* **272:** 895-899

Kawaguchi K, Uemura S, Ishiwata S (2003) Equilibrium and transition between single- and double-headed binding of kinesin as revealed by single-molecule mechanics. *Biophys J* **84:** 1103-1113

Kimble M, Church K (1983) Meiosis and early cleavage in Drosophila melanogaster eggs: effects of the claret-non-disjunctional mutation. *Journal of cell science* **62:** 301-318

King SJ, Schroer TA (2000) Dynactin increases the processivity of the cytoplasmic dynein motor. *Nat Cell Biol* **2:** 20-24

Klumpp S, Lipowsky R (2005) Cooperative cargo transport by several molecular motors. *P Natl Acad Sci USA* **102:** 17284-17289

Kolomeisky AB, Fisher ME (2007) Molecular motors: a theorist's perspective. *Annu Rev Phys Chem* **58:** 675-695

Korten T, Birnbaum W, Kuckling D, Diez S (2011) Selective Control of Gliding Microtubule Populations. *Nano Lett*

Kron SJ, Spudich JA (1986) Fluorescent Actin-Filaments Move on Myosin Fixed to a Glass-Surface. *P Natl Acad Sci USA* **83:** 6272-6276

Kühne W (1864) *Untersuchungen über das Protoplasma und die Contractilität*, Leipzig: Engelmann.

Kural C, Kim H, Syed S, Goshima G, Gelfand VI, Selvin PR (2005) Kinesin and dynein move a peroxisome in vivo: a tug-of-war or coordinated movement? *Science* **308:** 1469-1472

Landau LD, Lifschnitz EM (1991) *Lehrbuch der theoretischen Physik*: Harri Deutsch.

Lawrence CJ, Dawe RK, Christie KR, Cleveland DW, Dawson SC, Endow SA, Goldstein LS, Goodson HV, Hirokawa N, Howard J, Malmberg RL, McIntosh JR, Miki H, Mitchison TJ, Okada Y, Reddy AS, Saxton WM, Schliwa M, Scholey JM, Vale RD, Walczak CE, Wordeman L (2004) A standardized kinesin nomenclature. *The Journal of cell biology* **167:** 19-22

Leduc C, Campas O, Zeldovich KB, Roux A, Jolimaitre P, Bourel-Bonnet L, Goud B, Joanny JF, Bassereau P, Prost J (2004) Cooperative extraction of membrane nanotubes by molecular motors. *P Natl Acad Sci USA* **101:** 17096-17101

Leduc C, Pavin N, Julicher F, Diez S (2010) Collective behavior of antagonistically acting kinesin-1 motors. *Phys Rev Lett* **105:** 128103

Leduc C, Ruhnow F, Howard J, Diez S (2007) Detection of fractional steps in cargo movement by the collective operation of kinesin-1 motors. *P Natl Acad Sci USA* **104:** 10847-10852

Lye RJ, Porter ME, Scholey JM, McIntosh JR (1987) Identification of a microtubule-based cytoplasmic motor in the nematode C. elegans. *Cell* **51:** 309-318

Mallik R, Carter BC, Lex SA, King SJ, Gross SP (2004) Cytoplasmic dynein functions as a gear in response to load. *Nature* **427:** 649-652

Mallik R, Petrov D, Lex SA, King SJ, Gross SP (2005) Building complexity: An in vitro study of cytoplasmic dynein with in vivo implications. *Curr Biol* **15:** 2075-2085

Mashanov GI, Tacon D, Peckham M, Molloy JE (2004) The spatial and temporal dynamics of pleckstrin homology domain binding at the plasma membrane measured by Imaging single molecules in live mouse myoblasts. *J Biol Chem* **279:** 15274-15280

Meyhofer E, Howard J (1995) The force generated by a single kinesin molecule against an elastic load. *P Natl Acad Sci USA* **92:** 574-578

Mitchison T, Kirschner M (1984) Dynamic Instability of Microtubule Growth. *Nature* **312:** 237-242

Muller MJI, Klumpp S, Lipowsky R (2008) Tug-of-war as a cooperative mechanism for bidirectional cargo transport by molecular motors. *P Natl Acad Sci USA* **105:** 4609-4614

Needham J, Kleinzeller A, Miall M, Dainty M, Needham DM, Lawrence ASC (1942) Is muscle contraction essentially an enzymesubstrate combination? *Nature* **150:** 46-49

Nitzsche B, Ruhnow F, Diez S (2008) Quantum-dot-assisted characterization of microtubule rotations during cargo transport. *Nature nanotechnology* **3:** 552-556

Parvinen M, Soderstrom KO (1976) Chromosome Rotation and Formation of Synapsis. *Nature* **260:** 534-535

Paschal BM, Shpetner HS, Vallee RB (1987) Map 1c Is a Microtubule-Activated Atpase Which Translocates Microtubules Invitro and Has Dynein-Like Properties. *J Cell Biol* **105:** 1273-1282

Pecreaux J, Roper JC, Kruse K, Julicher F, Hyman AA, Grill SW, Howard J (2006) Spindle oscillations during asymmetric cell division require a threshold number of active cortical force generators. *Curr Biol* **16:** 2111-2122

Qiu W, Derr ND, Goodman BS, Villa E, Wu D, Shih W, Reck-Peterson SL (2012) Dynein achieves processive motion using both stochastic and coordinated stepping. *Nature Structural & Molecular Biology Advance Online Publication*

Ray S, Meyhofer E, Milligan RA, Howard J (1993) Kinesin follows the microtubule's protofilament axis. *The Journal of cell biology* **121:** 1083-1093

Reck-Peterson SL, Vale RD (2004) Molecular dissection of the roles of nucleotide binding and hydrolysis in dynein's AAA domains in Saccharomyces cerevisiae. *P Natl Acad Sci USA* **101:** 14305

Reck-Peterson SL, Yildiz A, Carter AP, Gennerich A, Zhang N, Vale RD (2006) Single-molecule analysis of dynein processivity and stepping behavior. *Cell* **126:** 335-348

Redemann S, Pecreaux J, Goehring NW, Khairy K, Stelzer EHK, Hyman AA, Howard J (2010) Membrane Invaginations Reveal Cortical Sites that Pull on Mitotic Spindles in One-Cell C. elegans Embryos. *Plos One* **5**

Rogers AR, Driver JW, Constantinou PE, Jamison DK, Diehl MR (2009) Negative interference dominates collective transport of kinesin motors in the absence of load. *Phys Chem Chem Phys* **11:** 4882-4889

Rogers KR, Weiss S, Crevel I, Brophy PJ, Geeves M, Cross R (2001) KIF1D is a fast non-processive kinesin that demonstrates novel K-loop-dependent mechanochemistry. *Embo J* **20:** 5101-5113

Roostalu J, Hentrich C, Bieling P, Telley IA, Schiebel E, Surrey T (2011) Directional Switching of the Kinesin Cin8 Through Motor Coupling. *Science* **332:** 94-99

Ross JL, Shuman H, Holzbaur ELF, Goldman YE (2008) Kinesin and dynein-dynactin at intersecting microtubules: Motor density affects dynein function. *Biophys J* **94:** 3115-3125

Ruhnow F, Zwicker D, Diez S (2011) Tracking Single Particles and Elongated Filaments with Nanometer Precision. *Biophys J* **100:** 2820-2828

Sablin EP, Case RB, Dai SC, Hart CL, Ruby A, Vale RD, Fletterick RJ (1998) Direction determination in the minus-end-directed kinesin motor ncd. *Nature* **395:** 813-816

Scherthan H, Wang HL, Adelfalk C, White EJ, Cowan C, Cande WZ, Kaback DB (2007) Chromosome mobility during meiotic prophase in Saccharomyces cerevisiae. *P Natl Acad Sci USA* **104:** 16934-16939

Schnitzer MJ, Block SM (1997) Kinesin hydrolyses one ATP per 8-nm step. *Nature* **388:** 386-390

Schnitzer MJ, Visscher K, Block SM (2000) Force production by single kinesin motors. *Nat Cell Biol* **2:** 718-723

Schuster M, Lipowsky R, Assmann MA, Lenz P, Steinberg G (2011) Transient binding of dynein controls bidirectional long-range motility of early endosomes. *P Natl Acad Sci USA* **108:** 3618-3623

Shaklee PM, Idema T, Koster G, Storm C, Schmidt T, Dogterom M (2008) Bidirectional membrane tube dynamics driven by nonprocessive motors. *P Natl Acad Sci USA* **105:** 7993-7997

Sharp DJ, Yu KR, Sisson JC, Sullivan W, Scholey JM (1999) Antagonistic microtubule-sliding motors position mitotic centrosomes in Drosophila early embryos. *Nat Cell Biol* **1:** 51-54

Shevkoplyas SS, Siegel AC, Westervelt RM, Prentiss MG, Whitesides GM (2007) The force acting on a superparamagnetic bead due to an applied magnetic field. *Lab Chip* **7:** 1294-1302

Shubeita GT, Tran SL, Xu J, Vershinin M, Cermelli S, Cotton SL, Welte MA, Gross SP (2008) Consequences of Motor Copy Number on the Intracellular Transport of Kinesin-1-Driven Lipid Droplets. *Cell* **135:** 1098-1107

Soppina V, Rai AK, Ramaiya AJ, Barak P, Mallik R (2009) Tug-of-war between dissimilar teams of microtubule motors regulates transport and fission of endosomes. *P Natl Acad Sci USA* **106:** 19381-19386

Svoboda K, Block SM (1994) Force and Velocity Measured for Single Kinesin Molecules. *Cell* **77:** 773-784

Svoboda K, Schmidt CF, Schnapp BJ, Block SM (1993) Direct observation of kinesin stepping by optical trapping interferometry. *Nature* **365:** 721-727

Szent-Györgyi A, Banga I (1941–1942) *Studies from the Institute of Medical Chemistry University Szeged* **1:** 5–15

Szent-Györgyi A, Banga I (1942) *Studies from the Institute of Medical Chemistry University Szeged* **1:** 17–26

Tao L, Mogilner A, Civelekoglu-Scholey G, Wollman R, Evans J, Stahlberg H, Scholey JM (2006) A homotetrameric kinesin-5, KLP61F, bundles microtubules and antagonizes Ncd in motility assays. *Current biology : CB* **16:** 2293-2302

Thorn KS, Ubersax JA, Vale RD (2000) Engineering the processive run length of the kinesin motor. *J Cell Biol* **151:** 1093-1100

Tischer C, Brunner D, Dogterom M (2009) Force- and kinesin-8-dependent effects in the spatial regulation of fission yeast microtubule dynamics. *Mol Syst Biol* **5:** 250

Toba S, Watanabe TM, Yamaguchi-Okimoto L, Toyoshima YY, Higuchi H (2006) Overlapping hand-over-hand mechanism of single molecular motility of cytoplasmic dynein. *P Natl Acad Sci USA* **103:** 5741-5745

Vale RD (2003) The molecular motor toolbox for intracellular transport. *Cell* **112:** 467-480

Vale RD, Funatsu T, Pierce DW, Romberg L, Harada Y, Yanagida T (1996) Direct observation of single kinesin molecules moving along microtubules. *Nature* **380:** 451-453

Vale RD, Malik F, Brown D (1992) Directional instability of microtubule transport in the presence of kinesin and dynein, two opposite polarity motor proteins. *The Journal of cell biology* **119:** 1589-1596

Vale RD, Reese TS, Sheetz MP (1985) Identification of a novel force-generating protein, kinesin, involved in microtubule-based motility. *Cell* **42:** 39-50

Verbrugge S, van den Wildenberg SMJL, Peterman EJG (2009) Novel Ways to Determine Kinesin-1's Run Length and Randomness Using Fluorescence Microscopy. *Biophys J* **97:** 2287-2294

Vogel SK, Pavin N, Maghelli N, Julicher F, Tolic-Norrelykke IM (2009) Self-Organization of Dynein Motors Generates Meiotic Nuclear Oscillations. *Plos Biol* **7:** 918-928

Volta A (1792) *Briefe über thierische Elektricität*, Leipzig: Wilhelm Engelmann.

Walker RA, Salmon ED, Endow SA (1990) The Drosophila-Claret Segregation Protein Is a Minus-End Directed Motor Molecule. *Nature* **347:** 780-782

Weddemann A, Ennen I, Regtimer A, Albon C, Wolff A, Eckstädt K, Mill N, Peter MKH, Mattay J, Plattner C, Sewald N, Hütten A (2010) Review and outlook: from single nanoparticles to self-assembled monolayers and granular GMR sensors. *Beilstein Journal of Nanotechnology* **1:** 75-93

Weisenberg RC (1972) Microtubule Formation in-Vitro in Solutions Containing Low Calcium Concentrations. *Science* **177:** 1104-&

Welte MA (2004) Bidirectional transport along microtubules. *Curr Biol* **14:** R525-R537

Welte MA, Gross SP, Postner M, Block SM, Wieschaus EF (1998) Developmental regulation of vesicle transport in Drosophila embryos: Forces and kinetics. *Cell* **92:** 547-557

Yajima J, Alonso MC, Cross RA, Toyoshima YY (2002) Direct long-term observation of kinesin processivity at low load. *Curr Biol* **12:** 301-306

Yildiz A, Tomishige M, Gennerich A, Vale RD (2008) Intramolecular strain coordinates kinesin stepping behavior along microtubules. *Cell* **134:** 1030-1041

Yildiz A, Tomishige M, Vale RD, Selvin PR (2004) Kinesin walks hand-over-hand. *Science* **303:** 676-678

8 Acknowledgement

First of all I would like to thank Dr. Iva Tolic-Norrelykke for offering me such an interesting project and for giving me the opportunity to work at the MPI-CBG in Dresden. I also want to thank her for supervising my thesis work, in particular for the scientific advices and discussions, generous funding (e.g. for conference participations), and keeping up a very positive and supportive atmosphere in the lab. Furthermore I am grateful for the freedom to choose the direction of my project and her comments on the manuscript of this thesis.

I am very grateful to Prof. Dr. Stefan Diez for being a very helpful and encouraging second supervisor. I always felt welcome in his lab (and the weekly group meetings) and I appreciate, that he shared his expertise in *in vitro* experiments without hesitation. I am particularly grateful for being allowed to use his lab's equipment and for the opportunity to teach younger students how to use it. I want to thank him, too, for reading the manuscript of this thesis.

I am also grateful to Prof. Dr. Petra Schwille for participating in my thesis advisory committee. I want to thank her and Prof. Dr. Arne Gennerich for reviewing the thesis work.

I am highly indebted to Veikko Geyer for his great help in using the magnetic tweezing setup he constructed. His enthusiasm and intellectual openness has encouraged me strongly - in particular during the second research year - not to give up but pursue my aims.

I am also highly indebted to Rui Ma and Prof. Dr. Nenad Pavin, who developed the theory for the doublet experiments and explained patiently all the details of their work to me.

I am also very grateful to the whole lab of Dr. Iva Tolic-Norrelykke for the open and supportive atmosphere. I am particularly thankful to Dr. Nicola Maghelli for the discussions over the countless *espressi.* I want to thank Dr. Damien Ramunno-

Johnson for his help with Matlab and drawing my attention to the problems of colorblind scientists.

I also would like to thank all members of the lab of Prof. Dr. Stefan Diez for sharing their knowledge and support with all technical questions. I am particularly grateful to Dr. Bert Nitzsche for providing the protocol for the Ncd gliding assay and help with the purification of Ncd. Furthermore, I want to thank Juliane Beyer for helping with the Ncd related experiments. I am also indebted to Dr. Gero Fink and Dr. Till Korten for general discussions and help with my first *in vitro* experiments. I also want to thank Corina Brauer for help in preparing silanized coverslips and my first protein purification. I am grateful to Felix Ruhnow for providing his tracking software FIESTA and to Viktor Schroeder for generously sharing data for the temperature dependent gliding of kinesin-1. I want to thank Dr. Cecile Leduc for providing the initial doublet protocol.

I want to thank the light microscopy facility of the MPI-CBG, in particular Dr. Britta Schroth-Diez, for general technical support and trouble-shooting with the TIRF setup.

I want to thank Dr. David Drechsel and Dr. Aliona Bogdanova for initial help with handling the yeast strains and the purification of dynein.

I want to thank Prof. Dr. Ron Vale for providing the yeast strains VY 208 and VY 268, which were used for the expression of dynein.

I want to thank the Deutsche Forschungsgemeinschaft for financial support. I want to thank the Studienstiftung des deutschen Volkes for financial support as well as providing the opportunity to participate in interdisciplinary summer schools.

Last but not least I want to thank my friends, белочка and my family for their emotional support during the last three years.

Erklärung entsprechend §5.5 der Promotionsordnung

Hiermit versichere ich, dass ich die vorliegende Arbeit ohne unzulässige Hilfe Dritter und ohne Benutzung anderer als der angegebenen Hilfsmittel angefertigt habe; die aus fremden Quellen direkt oder indirekt übernommenen Gedanken sind als solche kenntlich gemacht. Die Arbeit wurde bisher weder im Inland noch im Ausland in gleicher oder ähnlicher Form einer anderen Prüfungsbehörde vorgelegt.

Die Dissertation wurde im Zeitraum vom 01.09.2008 bis 13.01.2012 verfasst und von Dr. Iva Tolic-Norrelykke, Max Planck Institut für molekulare Zellbiologie und Genetik, Dresden, betreut.

Meine Person betreffend erkläre ich hiermit, dass keine früheren erfolglosen Promotionsverfahren stattgefunden haben.

Ich erkenne die Promotionsordnung der Fakultät für Mathematik und Naturwissenschaften, Technische Universität Dresden, an.

Dresden, 13.01.2012